Geochemistry and petrogenesis of kimberlite intrusions from the eastern lobe the Du Toitspan kimberlite pipe, South Africa.

Dissertation submitted in fulfilment of the requirements for the degree of Master of Science

University of Cape Town

May 2020

Lesego Ramokgaba

Supervisor: Prof A. P le Roex

Co – supervisor: Dr J.V.A Robey

DECLARATION

I know the meaning of plagiarism and declare that all of the work in the dissertation is my own except where otherwise stated in the text.

L. Ramokgaba

May 2020

ACKNOWLEDGMENT

This study would have not been possible had it not been for the unbelievable support that I have been privileged enough to enjoy throughout its duration. First and foremost, to my supervisor Prof Anton le Roex, thank you for your endless patience, support, encouragement, and overall scientific guidance. I could have not asked for a better supervisor. I would also like to thank my co – supervisor, Dr Jock Robey, for assisting greatly especially during the initial stages of the project. I sincerely appreciate you welcoming me into your home and sharing your wealth of knowledge with me. I am also grateful to the scientific and technical staff at UCT for your great assistance with sample preparation and analysis. You guys are incredible.

To my former colleagues–Anne-Marie Nieuwoudt, Iyanai Murimba, Brent Alting and Andrew Rogers, whom allowed me to undertake this project, I am sincerely grateful. I would like to extend my gratitude to my current colleagues, Wiehan Smit and Leah Nyoni for always understanding whenever I needed to take time off work and their willingness to pick up the slack in my absence. To my friends, for always making visits to Cape Town memorable and enjoyable, thank you. Lastly but certainly not least, to my family, thank you for always reminding me in the dark moments of the light awaiting at end of this journey.

ABSTRACT

The Du Toitspan kimberlite pipe located on the outskirts of Kimberley South Africa, is one four Cretaceous aged major kimberlite pipes from the well-known Kimberley cluster, the type locality for archetypal group I kimberlites. Twenty-seven samples representative of various kimberlite intrusions from the eastern lobe of the Du Toitspan kimberlite pipe have been analysed for their whole – rock geochemistry and mineral chemistry (olivine and phlogopite) with the aim of developing semi – quantitative models that constrain their petrogenesis and characterise their respective source region(s). Investigated intrusions include; D13 – phlogopite kimberlite, D14 – monticellite kimberlite, D17 – serpentinized phlogopite kimberlite, and several narrow (<1m) calcite kimberlite dykes ranging in texture from aphanitic to macrocrystic. The aphanitic calcite dykes were further sub-divided into; a phlogopite – rich calcite kimberlite, a perovskite – rich calcite kimberlite, opaque-rich calcite kimberlites and serpentine calcite kimberlites.

Compositions of analysed olivine cores in the macrocrystic kimberlite varieties are similar (Fo_{91-93}; NiO ~0.4 wt. %) but are more variable in the aphanitic kimberlite varieties (Fo_{84-91}; NiO = 0.37 – 0.42 wt. %). Olivine rims in all kimberlite intrusions show restricted forsterite contents (Fo_{87-89}), with variable NiO (0.24 – 0.39 wt. %). Phlogopite compositions show broad overlap, although some phlogopite microcrysts in the D13 – phlogopite kimberlite are slightly poorer in K_2O and richer in F contents compared to those in the D14 – monticellite kimberlite and the calcite kimberlite dykes. Because major elements in all samples of the D17 – serpentinized phlogopite kimberlite samples show unambiguous evidence of crustal contamination, these were omitted from further investigation. Major and trace elements in other kimberlite intrusions in this study are free of significant crustal contamination, and exhibit geochemical variations that are broadly similar except for higher K_2O (and Al_2O_3) and lower Gd/Yb ratios in the D13 – phlogopite kimberlite.

Semi – quantitative partial melting models indicate that the full range of REE abundances in the different kimberlite intrusions can be explained by variable degrees of partial melting (0.4 – 0.9%) of a single peridotite source composition in terms of REE, that is enriched in light REE (La = 2.10 × PM) and depleted in heavy REE (Yb = 0.71 × PM), provided that the relative proportions of residual garnet and clinopyroxene are allowed to vary. The lower Gd/Yb ratios characterising the D13 – phlogopite kimberlite can be explained by ~0.5 –0.6% degrees of partial melting a peridotite source with a higher proportion of residual clinopyroxene relative to garnet. The higher Gd/Yb

ratios characterising the D14 – monticellite kimberlite are consistent with similar degrees of partial melting of a source with a higher proportion of residual garnet relative to clinopyroxene. The macrocrystic calcite kimberlite and the aphanitic phlogopite-rich calcite kimberlite dykes are related to the D14 – monticellite kimberlite by derivation from a similar source, where slight variations in their respective REE abundances are consistent with variation in the degree of partial melting (0.4 – 0.6%). The aphanitic opaque-rich calcite kimberlites and serpentine calcite kimberlites are higher degree partial melts (F=0.9%) requiring a slightly more refractory source, with a slightly greater garnet clino pyroxene ratios than the one giving rise to the D14 – monticellite kimberlite and associated calcite dykes. The latter are also potentially parental to the aphanitic perovskite-rich calcite kimberlite by ~20 – 50% olivine fractionation, although other incompatible elements (e.g., Nb, Zr) cannot be accounted for by olivine fractionation.

K and Al enrichment in the D13 – phlogopite kimberlite is consistent with partial melting of a source with accessory phlogopite. Although the absence K-anomalies on primitive mantle normalised diagrams of samples for the D13 – phlogopite kimberlite suggests that phlogopite was exhausted shortly before or at the moment of melt extraction. Given that the thermal stability of phlogopite does not extend into the sub-lithospheric mantle, phlogopite equilibrating against the D13 – phlogopite kimberlite argues for a source region located within the sub-continental lithospheric mantle. Further, the occurrence of diagnostic incompatible trace element ratios (Ba/Nb, La/Nb, Th/Nb, and Ce/Pb) that have been ascribed a sub-lithospheric mantle origin, support a two stage petrogenetic model where alkali-silicate melts/fluids from an upwelling Mesozoic plume infiltrate through a depleted garnet peridotite protolith and crystallize phlogopite and clinopyroxene possibly in PIC (phlogopite – Ilmenite – Clinopyroxene) bifurcating vein networks. Away from these networks, distal depleted peridotite is progressively cryptically metasomatised from garnet peridotite (GP) to a modally metasomatised garnet phlogopite peridotite (GPP) in more proximal regions. Subsequent heating of this variably metasomatised source by an upwelling mantle plume could have gradually raised the regional geotherm above the peridotite solidus resulting in the petrogenesis of the Du Toitspan kimberlite pipe.

LIST OF FIGURES

LIST OF TABLES

CONTENTS

CHAPTER 1: INTRODUCTION

1.1. DEFINITION AND CLASSIFICATIONS OF KIMBERLITES

Lewis (1887) first coined the term kimberlite to describe 'the matrix to diamonds' shortly following their discovery from the type locality of Kimberley, South Africa. Kimberlites can be broadly defined geochemically as being silica under-saturated, volatile rich magmas, with high concentrations of incompatible elements (Smith et al., 1985; Woolley et al., 1996). The petrological definition of kimberlites presented in Mitchell (1995) endorsed by the International Union of Geological Sciences (IUGS) Sub commission on the systematics of Igneous Rocks (Woolley et al., 1996; Maitre et al., 2005) is quoted below.

"Kimberlites are defined as having a distinctive inequigranular texture resulting from the presence of macrocrysts (and in some instances megacrysts) set in a fine-grained matrix. The megacryst/macrocryst assemblage consists of rounded anhedral crystals of magnesian ilmenite, Cr-poor titanian pyrope, olivine, Cr-poor clinopyroxene, phlogopite, enstatite and Ti-poor chromite. Olivine is the dominant member of the macrocryst assemblage. The matrix minerals include; second generation euhedral primary olivine and/or phlogopite, together with perovskite, spinel (titaniferous magnesian aluminous titanian chromite, members of the magnesian ulvospinel-ulvospinel-magnetite series), diopside (Al and Ti poor), monticellite, apatite, calcite, and primary late stage serpentine (commonly Fe rich). Some kimberlites have late-stage poikilitic eastonitic phlogopites. Nickeliferous sulphides and rutile are common accessory minerals. The replacement of early-formed olivine, phlogopite, monticellite, and apatite by deuteric serpentine and calcite is common. Evolved members may be devoid of, or poor in, macrocrysts, and are termed aphanitic kimberlite. They are composed essentially of calcite, serpentine and magnetite, together with minor phlogopite, apatite, and perovskite."

Wagner (1914) was first to recognise that there were at least two distinct diamond-bearing kimberlite varieties in Southern Africa, which he identified as "basaltic or non-micaceous" and "lamprophyric or micaceous". Smith (1983) later showed that these two kimberlite varieties can be distinguished from each other according to their Pb, Sr and Nd isotope compositions. On this basis, kimberlites were classified into group I and II, broadly corresponding to Wagner's non-micaceous and micaceous kimberlites, respectively. Smith (1983) interpreted these findings to suggest that group I kimberlites were derived from the sub-lithospheric mantle (asthenosphere), and group II kimberlites from the sub-continental lithospheric mantle. Skinner (1989) later

showed that the isotopically distinct group I and II kimberlites also have corresponding differences in their groundmass mineralogy. Group I kimberlites are recognised by their olivine-rich monticellite ± phlogopite ± serpentine ± calcite groundmass mineral assemblage, whereas group II kimberlites are commonly diopside-bearing and very rich in phlogopite (Skinner, 1989). The occurrence of kimberlites with isotopic compositions that are transitional between the two kimberlite variants have also been recognised (e.g., Smith et al., 1985; Becker et al., 2007; Chapalathi Rao and Dongre, 2009). Although this seemingly well-established relationship between group I and II kimberlites has however been contested by Mitchell (1994, 1995), who maintains that the two exhibit mineralogical and compositional variations that are simply too distinct to suggest that they are end-members of the same magma type *senso-lato*. Subsequent discoveries of "orangeite-like" kimberlites in association with lamproites have been reported (e.g., Chalapathi et al., 2005; Pandey et al., 2017; Howarth and Giuliani, 2020) resulting in ambiguity regarding the nature of the relationship (or lack thereof) between group I kimberlites and orangeites (group II kimberlites?). This has even led some authors to propose that latter be classified as olivine lamproites (e.g., Dawson 1987; Pearson et al., 2019; Howarth and Giuliani, 2020) considering their close affinities in geochemistry, mineralogy and petrogenesis (e.g., Mitchell, 1995; Fraser et al., 1985).

1.2. DISTRIBUTION AND OCCURRENCES OF GROUP I KIMBERLITES IN SOUTH AFRICA

There are currently 10 known kimberlite provinces in South Africa (Skinner and Truswell, 2006). Within provinces, groups of intrusions define clusters or fields of ~1-20 individual kimberlite pipes (Mitchell, 1991). Group I Kimberlite provinces in South Africa occur both on- and off- craton, and their intrusions cluster in the following geographical localities (Fig. 1.1a) ; (1) those in the North West province centred around Rustenburg; (2) those in the central Free State Province, around Kroonstad; (3) those in the Northern Cape Province, around Kimberley; (4) and those located on the margins of the Kaapvaal craton, in the Northern Cape centred around Britstown (Skinner and Truswell, 2006). Most of these provinces are dated to be Jurassic-Cretaceous in age (Allsopp and Barrett, 1975), except for four (i.e., the Pruissen, Kuruman, Cullinan, and Alldays) where respective ages of approximately 1950Ma, 1650Ma, 1200Ma and 500Ma have been determined (Skinner and Truswell, 2006). The latter are less common and occur only in the Griqualand East and Victoria West provinces (Skinner and Truswell, 2006).

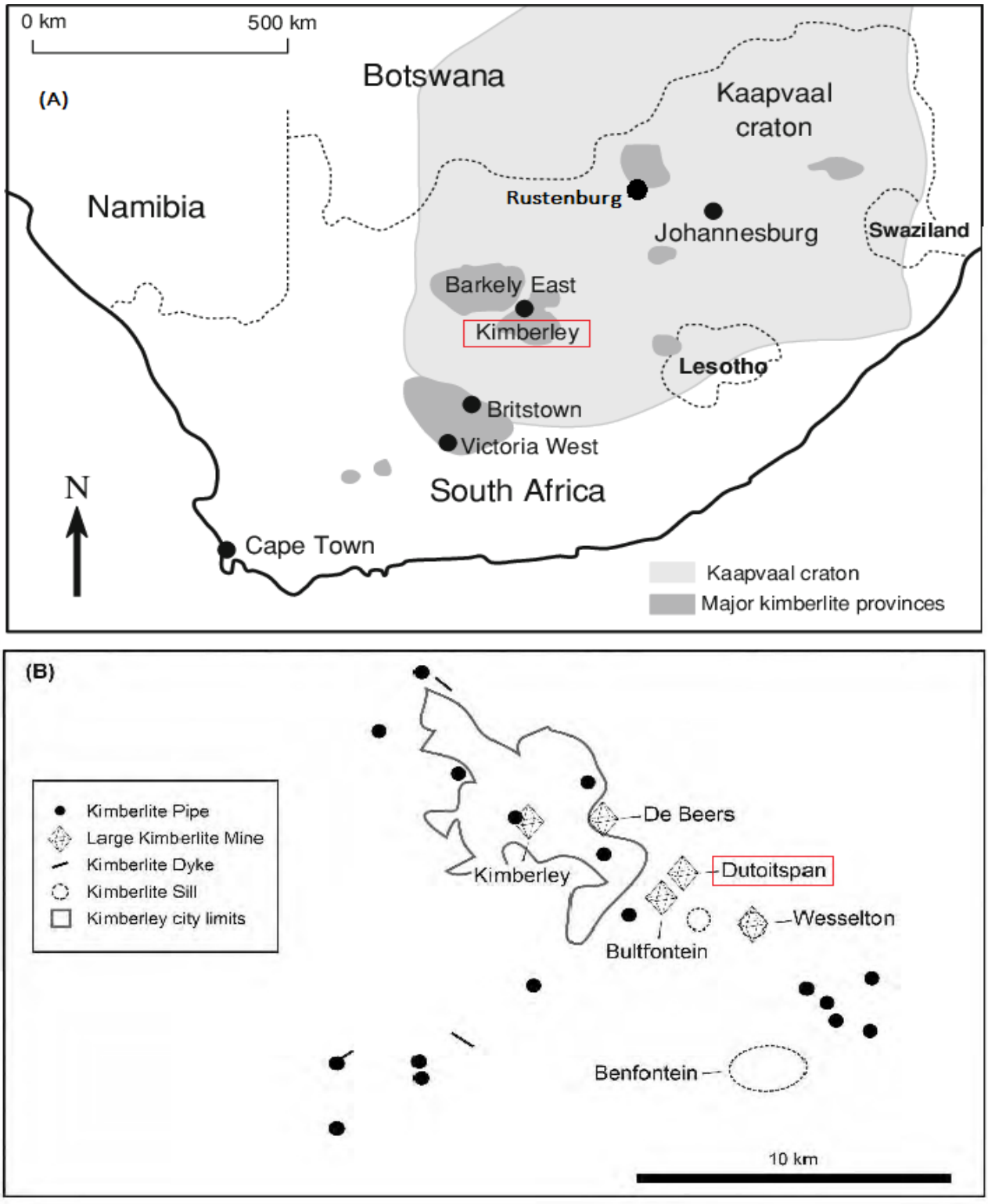

Figure 1.1 : Locality map of the Du Toitspan kimberlite pipe. (a) Map of the location of the town of Kimberley showing the Kaapvaal craton and major South African kimberlite provinces (adapted from Coe et al., 2008). (b) Map showing Kimberley town limits and the relative distribution of the major kimberlite pipes, dykes and sills that form part of the Kimberley cluster (adapted from Field et al., 2008).

1.3. THE SOUTH AFRICAN CLASSICAL KIMBERLITE PIPE MODEL

The South African classical kimberlite pipe model of Hawthorne (1975) depicts a steep-sided (~82°) pipe decreasing in size with depth. The early work of Clement (1982), Clement and Skinner (1979, 1985), Clement et al. (1984), and Clement and Reid (1989) established the sub-division of the South African classical kimberlite model into three distinct morphological zones. These zones consist of a basal root zone, an intermediate diatreme zone, and a top crater zone (Fig. 1.2). The existence of "transitional zones" between the diatreme and root zones infilled with kimberlites exhibiting petrographic features that are intermediate between pyroclastic and hypabyssal kimberlites have been discovered (e.g., Hetman et al., 2004; Skinner and Marsh, 2004; Mitchell and Smith, 2017; Gaudet et al., 2018), and are now incorporated into more modern versions of the model (Skinner, 2008).

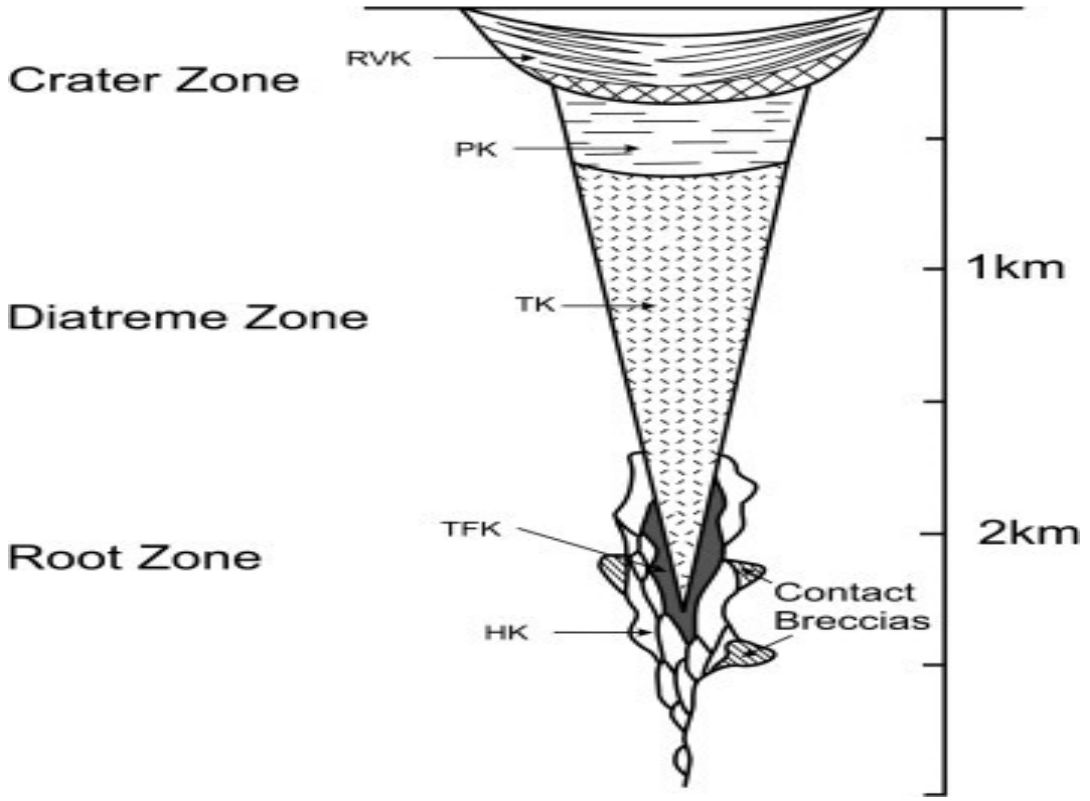

Figure 1.2: The South African kimberlite pipe model showing three morphological zones infilled with hypabyssal kimberlite (HK), Transitional-facies kimberlites (TFK), Massive Volcaniclastic kimberlite (TK), pyroclastic kimberlite (PK) and Re-sedimented volcaniclastic kimberlite (RVK) (Skinner,2008).

Incorporation of the diatreme and root zones into the South African classical kimberlite pipe model were based on observations made in mine exposures in the Kimberley area, South Africa (Field et al., 2008; Kjarsgaard, 2007). The root zone is predominately infilled with hypabyssal kimberlites, whereas the diatreme zone is mostly infilled by massive volcaniclastic kimberlites (formerly tuffistic kimberlites – TK) with relatively minor hypabyssal kimberlite intrusions extending from the root zone (Hawthorne, 1975; Fig 1.2). Incorporation of the crater zone into the model was based on observations made from Tanzania, Botswana, Angola and the Democratic Republic of Congo (DRC), where kimberlite pipes have experienced considerably less erosion compared those in Kimberley (Hawthorne, 1975). When present, the crater zone is infilled with re-sedimented volcaniclastic kimberlites (Hawthorne, 1975; Fig 1.2). A tuff ring was subsequently added to the model based on observations made in Mali (Hawthorne, 1975).

1.4. SCOPE AND AIMS OF PRESENT STUDY

To date, except for the work of Clement (1982), there have been no major studies undertaken on the eastern lobe of the Du Toitspan kimberlite pipe. Previous work has focused on intrusions from the western lobe of the pipe (e.g., Snowden, 1981; Hanekom, 2008; Ogilvie-Harris et al., 2009). The present study presents the first detailed geochemistry of kimberlites from the eastern lobe of the Du Toitspan kimberlite pipe with the aim of developing semi-quantitative models that constrain their petrogenesis and to characterise their source regions. To achieve this the present study is conducted with the following objectives;

- Firstly, to identify the geochemical variability that exists between the various kimberlite intrusions from the eastern lobe of the Du Toitspan kimberlite pipe.

- Secondly, to evaluate the influence of compositional modification experienced during syn- and post-emplacement (low temperature alteration, mantle entrainment, and fractionation) on the geochemistry of the various kimberlite intrusions. Thereafter, semi quantitative models that are consistent with the inherent geochemical variations that exist among them are used to place constraints on their petrogenesis and to characterise the source region(s).

CHAPTER 2: GEOLOGICAL SETTING AND SAMPLING

2.1. REGIONAL GEOLOGY

The Du Toitspan kimberlite pipe is located on the outskirts of Kimberley, South Africa (28° 46' S, 24° 47' E) and is one of four major kimberlite pipes from the well studied Kimberley cluster, the type locality for archetypal group I kimberlites (Fig. 1.1). The Du Toitspan kimberlite pipe was intruded during the Cretaceous through a basal Paleo - Mesoarchean basement complex, that is overlain by a Neoarchean volcano-sedimentary sequence (Ventersdorp Supergroup), and a Phanerozoic sequence of volcanic and sedimentary cover (Karoo Supergroup) (Clement, 1982). Hanson et al. (2009) estimates the paleo-surface in the Kimberley area at the time of emplacement to have been ~850m above the present surface.

2.1.1. Archean basement complex

The Archean basement complex comprises of foliated granitic and amphibolitic gneiss, intruded by granitoids of tonalitic-trondhjemitic-granodioritic compositions and greenstone belt remnants (Poujol and Anhaeusser, 2002; Hunter et al., 2006). The latter are metamorphosed mafic volcanic rocks that show strong geochemical affinities to komatiites (Fritiofsson, 2012). Migmatitic rocks have also been identified in a few mines in the region (Drennan et al., 1990). The Archean basement complex is commonly intruded by several late stage pegmatite and quartz veins (Clement, 1982).

2.1.2. Ventersdorp Supergroup

The Ventersdorp Supergroup is a Proterozoic supra-crustal volcano-sedimentary sequence that unconformably overlies the Archean basement complex. This part of the crust was developed after increased stability of the Kaapvaal craton following the accumulation of an earlier volcano-sedimentary sequence (Hunter et al., 2006). It comprises the basal volcanic Kilieprivers group that is overlain by the volcano sedimentary Platburg group and Bothaville formation, as well as the volcanic Allanridge formation at the top of the succession (Hunter et al., 2006). The Ventersdorp Supergroup is ca. 4km thick on average but is ~350m thick near the Du Toitspan kimberlite pipe and increases to ~1km south of the Wesselton kimberlite pipe (Clement, 1982).

2.1.3. Karoo Supergroup

The Karoo Supergroup unconformably overlies the Ventersdorp Supergroup. The development of the main Karoo basin in the region is considered to be coeval with the amalgamation of continental plates during the development of the Gondwana supercontinent (Hunter et al., 2006). During the late Carboniferous to the Early Permian, the basal unit of the Karoo Supergroup - the Dwyka Group was deposited on Precambrian bedrock, and was subsequently intruded by ~180 Ma dolerite sills, currently outcropping in the Kimberley area (Duncan and Marsh, 2006). The middle to upper groups of the Karoo Supergroup (Ecca, Beaufort, Stromberg, and Drakensberg) are currently eroded from the present stratigraphy, and evidence of their existence is only preserved as crustal xenoliths in kimberlites from the region.

2.2. DU TOITSPAN KIMBERLITE PIPE

During the 1970s an extensive array of sampling tunnels developed between 250 – 870m below surface in the Du Toitspan mine provided unprecedented exposure of the internal geology of Du Toitspan kimberlite pipe (Clement, 1982). By studying samples from these excavations, Clement (1982) was able to comprehensively document the internal geology of the Du Toitspan kimberlite pipe. Clement (1982) identified 18 petrographically distinct kimberlite varieties and classified them as D1 – D18 (Fig. 2.2; 2.3). Relative ages of the various kimberlite intrusions in the Du Toitspan kimberlite pipe were determined from temporal associations with the main established intrusive sequence (D6 – D16) from the western lobe of the pipe (Fig. 2.2). The central part of the Du Toitspan kimberlite pipe which is occupied by D11 - a massive volcaniclastic kimberlite extends towards the eastern and western peripheries (lobes) of the pipe where is it is intruded by multiple hypabyssal kimberlite intrusions.

2.2.1. Western lobe kimberlite intrusions

Kimberlite intrusions that form part of the western lobe can be grouped based on temporal-spatial associations into three intrusive sequences; (1) D6 to D16, (2) D10--D8--D9, and (3) D18--D7. (Fig. 2.2). Ogilvie - Harris et al. (2009) has shown that some of these kimberlite intrusions (e.g., D2 and D18) may have also experienced magmatic-mixing, and that they may also vary in oxygen fugacity (fO_2) with the D16 being the most oxidized and D5 the least oxidized. The western lobe is attached to a south western auxiliary blind kimberlite intrusion (D1) 870m below surface (Fig. 2.2). Details regrading petrographic features and diamond populations can be found in Clement (1982) and Hanekom (2008).

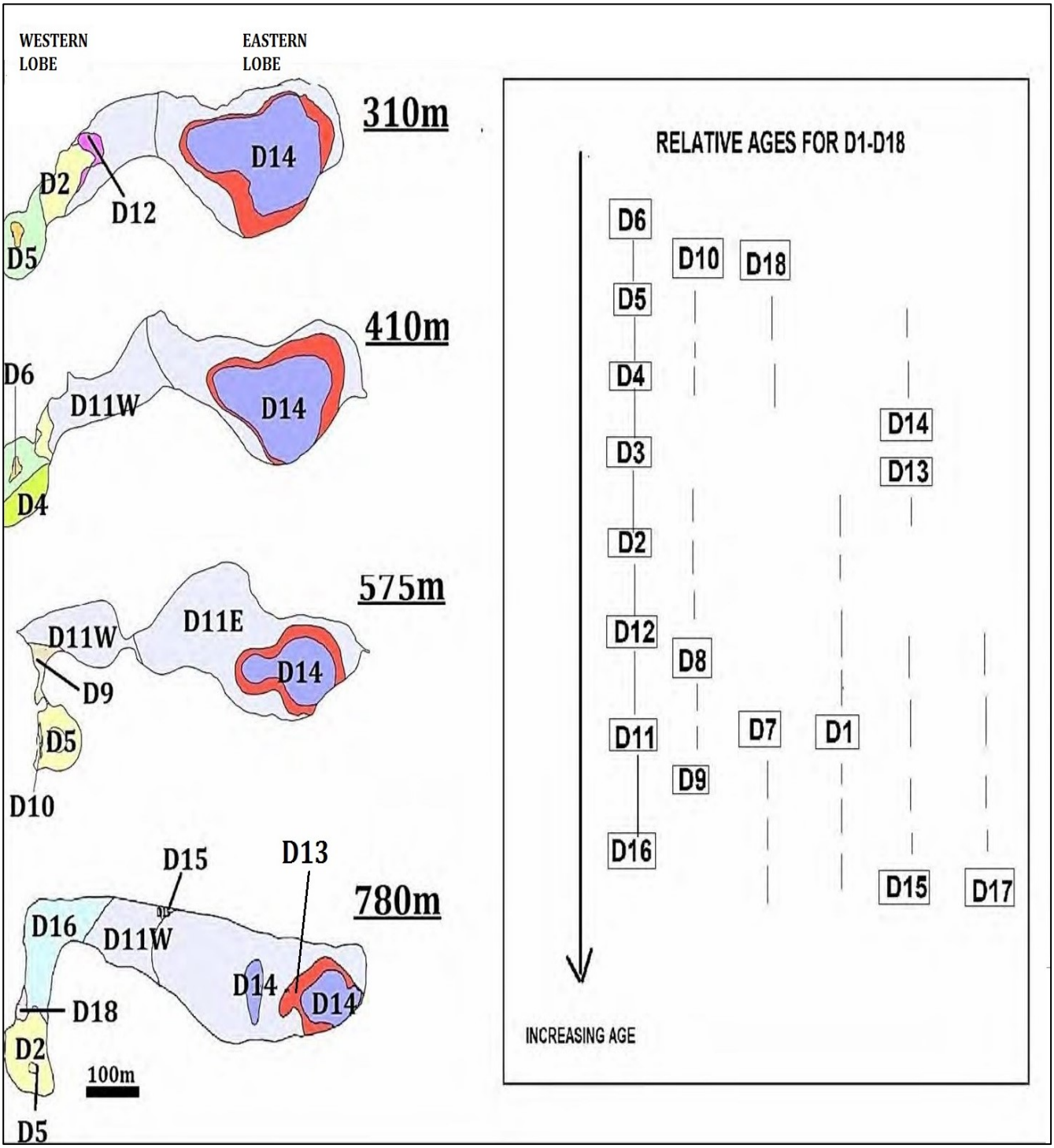

Figure 2.1: Morphology and internal geology of the Du Toitspan kimberlite pipe from 310 -780m (Adapted from Clement, 1982). **(Right)** Relative ages of D1 – D18 based on field relationships. The lines between the various kimberlite intrusions represent relative ages per intrusive sequence based on the relative ages of the main intrusive sequence (D6 – D16).

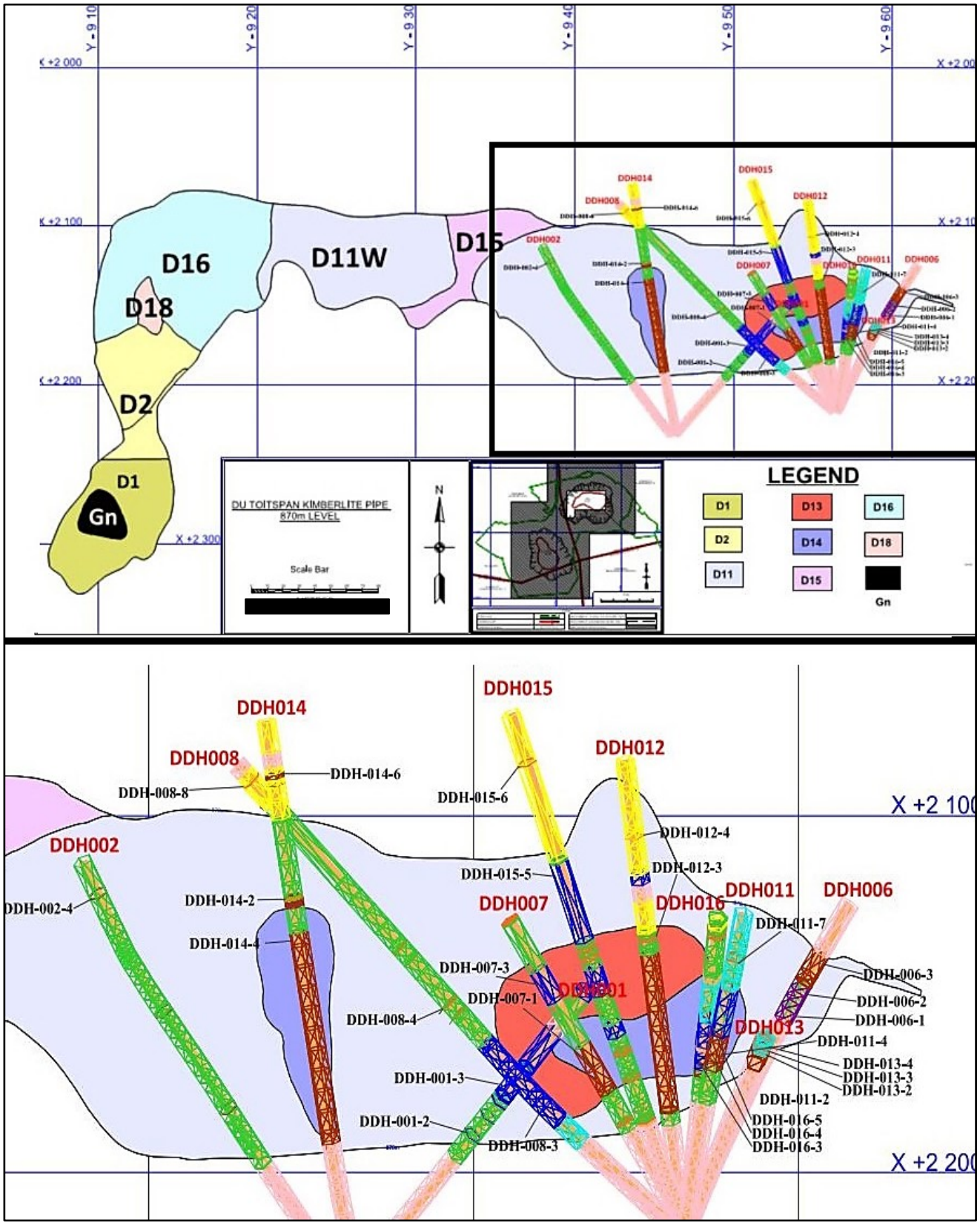

Figure 2.2: Schematic map of the Du Toitspan kimberlite pipe 870 m below surface. **(Top)** Plan view of the Du Toitspan kimberlite pipe at 870m below surface (scale bar = 100m). **(Bottom)** The eastern lobe of the Du Toitspan kimberlite pipe showing at 870m below surface. Borehole drilled downward from 870 m to ~1000m at variable dip angles. Borehole numbers are indicated in red text and sample numbers shown in black. Core-logs of the sampled boreholes are given in Appendix A.

2.2.2 Eastern lobe kimberlite intrusions

The eastern lobe is less complex than the western lobe. It comprises only two known kimberlite intrusive sequences (D13--D14 and D15--D17). The latter are relatively older kimberlite intrusions and are among the oldest in the pipe (Fig. 2.1). D15 is exposed from ~770m extending to 870m below surface (Fig. 2.1; 2.2). Although not shown in Figures 2.2, Clement (1982) also identified D17 as a small intrusion ~870m below surface. D14 is intruded into the D13 intrusive body and splits along two discreet conduits at depth, with the separate conduits coalescing into a single intrusion ~675m below surface (Clement, 1982). Information regarding their diamond populations can be found in Clement (1982).

2.2.3 Dykes

Clement (1982) recognised the occurrence of four types of dykes in the Du Toitspan kimberlite pipe. He referred to them as contemporaneous, internal, cross-cutting, and precursor dykes, respectively. Contemporaneous dykes are described as being large (extending for several hundreds of meters) and are interpreted to represent 'off-shoots or extensions of major intrusions into the country rock. Their emplacement is interpreted to have been coeval with pipe formation (Clement, 1982). The Du Toitspan kimberlite pipe hosts at least one known contemporaneous dyke exposed in the western lobe of the pipe (Hanekom, 2008). Precursor (or antecedant) dykes of Wagner (1914) are usually ~2m in length and intrude within the country rock (Clement, 1982). Cross-cutting dykes are rare and extend from the pipe into the country rock (Clement, 1982). Internal dykes are usually less than 2m wide and are intruded within major intrusive bodies in the pipe (Clement, 1982).

2.3 SAMPLING

A total of twenty-seven samples representative of various kimberlite intrusions were collected from 11 boreholes drilled between 870m to ~1000m on the eastern lobe of the Du Toitspan kimberlite pipe for study (Table 2.1). Figure 2.2 shows the positions of the collected samples from the respective bore holes.

Table 2.1: Samples collected for analysis. Also shown are corresponding depths, texture, and kimberlite phase for the respective samples.

DRILL-HOLE ID	SAMPLE ID	COLLAR DEPTH	TEXTURE	PHASE
DTP880/EX/DDH001	DDH-001-2	61.30	Aphanitic	Internal dykes
	DDH-001-3	97.20	Macrocrystic	D13
DTP880/EX/DDH002	DDH-002-4	105.15	Macrocrystic	Internal dyke
DTP880/EX/DDH006	DDH-006-1	69.40	Macrocrystic	D17
	DDH-006-2	76.00	Macrocrystic	D17
	DDH-006-3	86.90	Macrocrystic	D14
DTP880/EX/DDH007	DDH-007-1	84.00	Macrocrystic	D14
	DDH-007-3	120.00	Macrocrystic	D13
DTP880/EX/DDH008	DDH-008-3	76.60	Macrocrystic	D13
	DDH-008-4	98.00	Aphanitic	Internal dyke
	DDH-008-8	183.80	Aphanitic	Precursor dyke
DTP880/EX/DDH011	DDH-011-2	90.70	Macrocrystic	D14
	DDH-011-4	82.40	Macrocrystic	D17
	DDH-011-7	116.00	Slightly Macrocrystic	Internal dyke
DTP880/EX/DDH012	DDH-012-3	87.80	Aphanitic	Internal dyke
	DDH-012-4	118.20	Macrocrystic	Precursor dyke
DTP880/EX/DDH013	DDH-013-2	100.60	Slightly Macrocrystic	Internal dyke
	DDH-013-3	98.00	Aphanitic	Internal dyke
	DDH-013-4	103.40	Macrocrystic	D17
DTP/880/EX/DDH014	DDH-014-2	92.00	Macrocrystic	Internal dyke
	DDH-014-4	107.00	Macrocrystic	D14
	DDH-014-6	145.00	Aphanitic	Precursor dyke
DTP880/EX/DDH015	DDH-015-5	99.52	Macrocrystic	D14
	DDH-015-6	150.00	Macrocrystic	Precursor dyke
DTP880/EX/DDH016	DDH-016-3	56.85	Macrocrystic	D14
	DDH-016-4	59.12	Macrocrystic	D14
	DDH-016-5	65.35	Macrocrystic	D17

CHAPTER 3: PETROGRAPHY

3.1. INTRODUCTION

This chapter presents petrographic descriptions for kimberlite intrusions from the eastern lobe of the Du Toitspan kimberlite pipe. The aim is to identify and characterise salient textural and mineralogical features that distinguish them in order to classify them accordingly. Detailed descriptions for individual samples are given in Appendix B.1 – B.5. Kimberlite intrusions in this study are classified using the textural-genetic scheme of Clement and Skinner (1985) and using the mineralogical classification scheme of Clement and Skinner (1979) subsequently modified by Scott-Smith et al. (2018). The adopted mineralogical classification scheme uses the most abundant groundmass mineral except for olivine to classify kimberlites. Olivine is excluded because it is ubiquitous, prone to alteration and widely variable in kimberlites. If necessary, adjustments to the name can be made to include the next modally abundant mineral provided that it constitutes >2/3 the modal proportion of the dominant mineral. The next most prominent mineral may also be included provided it constitutes ~1/3 of the modal proportion of the dominant mineral. The latter minerals are usually denoted with the suffix – rich or – bearing. If significantly altered, the style of alteration (e.g., serpentinization) may also be included in the name.

The terms phenocryst and macrocryst are used here as descriptor terms without necessarily implying any genetic connotation. Minerals with grain sizes ranging from 0.1 – 0.5mm are described as phenocrysts, those with grains sizes >0.5mm as macrocrysts and those with grain sizes <0.1 mm as groundmass minerals (Scott-smith et al., 2018). The different kimberlite intrusions are also classified into macrocrystic when containing >15 vol. % macrocrysts, and as sparsely macrocrystic when containing 15 – 1 vol. % and lastly as aphanitic when containing <1% vol. % macrocrysts (Field and Scott-Smith, 1998).

3.2. D13 - PHLOGOPITE KIMBERLITE

[DDH-001-3, DDH-007-3, and DDH-008-3]

The D13 kimberlite intrusion is macrocrystic. It contains abundant up to 27 vol. % anhedral olivine macrocrysts that are up to 5.8mm in length. Olivine macrocrysts are mostly unaltered, although some are serpentinized along fractures and grain margins. Coarser olivine grains (>4mm) commonly exhibit strain features typical of ductile deformation. Deformation textures occur more prominently in the form of re-crystallized neoblasts (up to 0.2mm) (Fig. 3.1a). Olivine phenocrysts are anhedral to sub-euhedral. Coarser olivine phenocrysts (0.2 – 0.5mm) are commonly altered along grain margins with unaltered cores, while finer olivine phenocrysts (<0.2mm) tend to be completely serpentinized (Fig. 3.1c). Minor phlogopite and ilmenite phenocrysts are also present (Fig. 3.1c). The groundmass is uniformly textured and is dominated by phlogopite laths (Fig. 3.1). The groundmass assemblage consists of common equant euhedral to subhedral opaque oxides and perovskites, with minor serpentine, monticellite and calcite. The D13 kimberlite intrusion is classified as a hypabyssal uniformly textured macrocrystic phlogopite kimberlite.

3.3. D14 – MONTICELLITE KIMBERLITE

[DDH-006-3; DDH-007-1; DDH-011-2; DDH-014-4; DDH-015-5; DDH-016-3; and DDH-016-4]

The D14 kimberlite intrusion is macrocrystic. It contains less coarse and abundant olivine macrocrysts compared those in the D13 – phlogopite kimberlite. Apart from sample DDH-014-4 which contains ~35 vol. % olivine macrocrysts, other samples have <25 vol. % olivine macrocrysts. Olivine macrocrysts are typically serpentinized along grain margins with unaltered cores (Fig. 3.2a). Olivine macrocrysts commonly exhibit deformation textures in the form of undulose extinction, deformation lamellae, and neoblasts. Olivine macrocrysts sometimes contain chromite and pyrope inclusions (Fig. 3.2b; c). Phlogopite macrocrysts are rare and when present are typically resorbed and pseudomorphed (Fig. 3.2d). Similar to the D13 – phlogopite kimberlite, coarser olivine phenocrysts (0.2 – 0.5mm) are serpentinized along grain margins with unaltered cores, while the more finer olivine grains (<0.2mm) tend to be completely serpentinized. Phlogopite phenocrysts are rare and are commonly resorbed (Fig. 3.2f). The groundmass is uniformly textured, although some samples (DDH-011-2 and DDH-015-5) exhibit poorly developed segregations of serpentine and calcite (Fig. 3.2e). Monticellite is the dominant groundmass mineral showing replacement by calcite (e.g., DDH-015-5) in samples closer to the contact margin. The groundmass also contains common equant euhedral opaque oxides and perovskite grains. The rest of the groundmass assemblage consists of minor phlogopite laths, calcite, serpentine and accessory apatite. The D14 kimberlite intrusion is

classified as a hypabyssal uniformly textured macrocrystic monticellite kimberlite.

3.4. D17 – SERPENTINIZED PHLOGOPITE KIMBERLITE

[DDH-006-1, DDH-006-2, DDH-011-4, DDH-013-4, and DDH-016-5]

The D17 kimberlite intrusion a macrocrystic. It contains brownish-yellow perversely serpentinized olivines (Fig. 3.3a). Serpentinization has obscured deformation features in most olivine macrocrysts, although recrystallized olivine neoblasts are recognisable in some samples (e.g., DDH-011-4). Phlogopite macrocrysts are more abundant (~10 vol. %) compared to those observed in the D13 - phlogopite and D14 - monticellite kimberlites. Phlogopite macrocrysts are anhedral and serpentinized (Fig. 3.3a). Rare kelyphytized garnet xenocrysts are present in some samples (Fig. 3.3d; e). Samples (DDH-006-1 and DDH-006-2) also host crustal amphibole xenocrysts. Rare magmaclasts are present in some samples (DDH-006-1; Fig 3.3a). Euhedral to subhedral olivine and phlogopite phenocrysts are commonly serpentinized. Phlogopite phenocrysts are also altered and occasionally exhibit chemical zoned rims.

The groundmass varies from poorly (DDH-006-1) to very segregationary (DDH-016-5) in texture. Discrete residual pools containing cryptocrystalline serpentine and tabular calcite are well developed in the segregationary varieties. The groundmass is dominated by abundant altered brown phlogopite (Fig. 3.3f). The rest of the groundmass assemblage consists of equant euhedral to subhedral perovskite, opaque oxides, cryptocrystalline serpentine and accessory diopside microlites assemblage (Fig. 3.3). The presence of magmaclasts and microlitic diopside is in the D17 kimberlite is an indication that the latter experienced some sort of magmatic disruption in a near surface environment and subsequently solidified while transitioning from a hypabyssal into a pyroclastic kimberlite during emplacement (Hetman et al., 2004; Skinner and Marsh, 2004). Thus, the D17 kimberlite intrusion is classified as a transitional segregationary textured macrocrystic kimberlite. Mineralogically it is classified as a serpentinized phlogopite kimberlite.

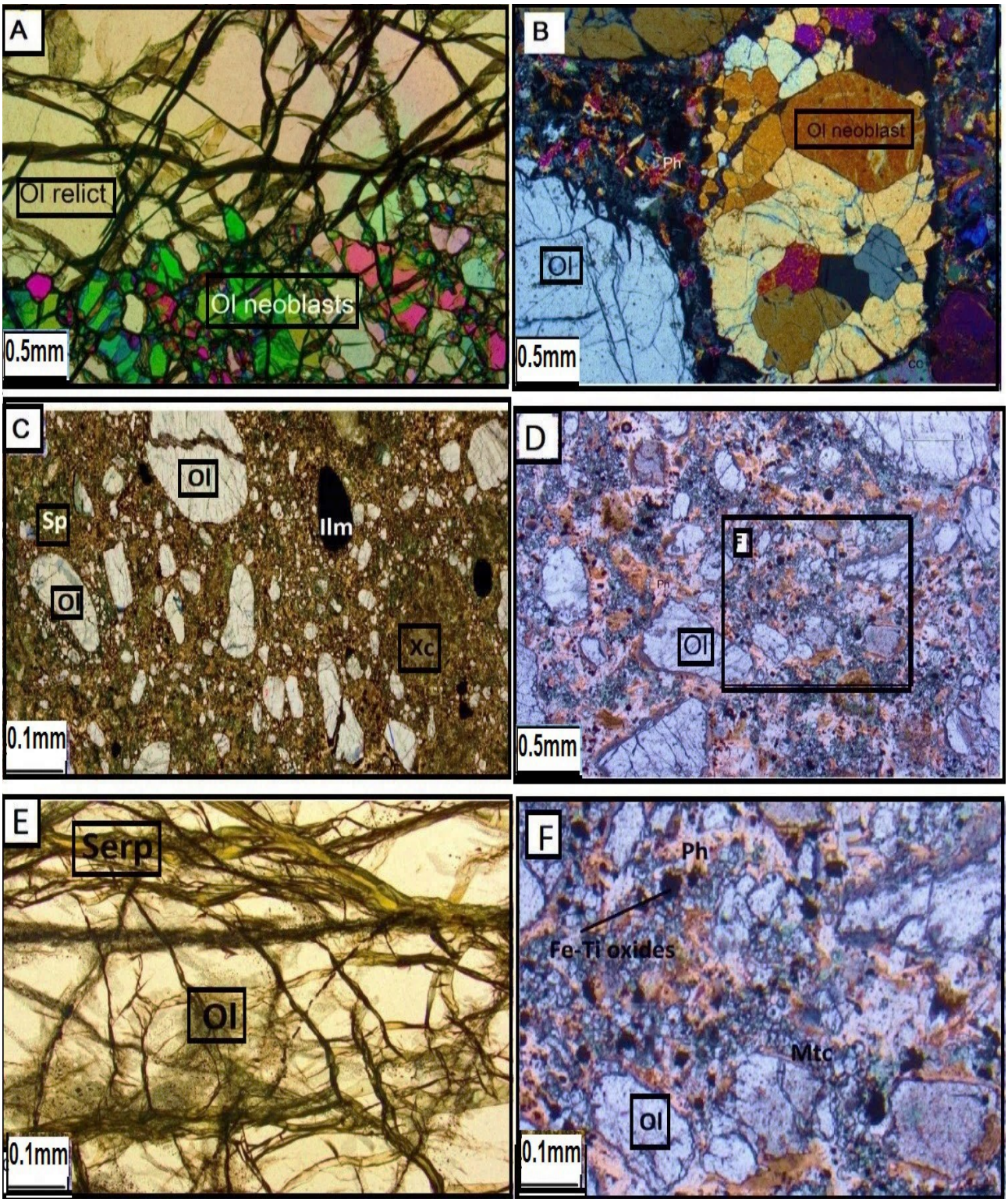

Figure 3.1: Photomicrographs of the D13 - phlogopite kimberlite. Ol = olivine, Sp = Serpentine, Ph = Phlogopite, Ilm = Ilmenite, Mtc = Monticellite. **(A)** A partially recrystallized olivine macrocrysts showing neoblasts and relict of original macrocryst taken under XPL light (DDH-001-3). **(B)** A partially recrystallized olivine macrocryst with neoblasts and preserved relict of original macrocryst (right). Non-recrystallized olivine macrocryst, all set in a phlogopite rich groundmass taken under XPL light (left) (DDH-001-3). **(C)** Ilmenite and olivine macrocrysts set in a phlogopite rich matrix (DDH-006-3). **(D)** Olivine macrocrysts set in a phlogopite -rich matrix with abundant monticellite (DDH-0007-3). **(E)** Fractured olivine macrocryst serpentinized along fractures (DDH-001-3). **(F)** High magnification of unusually coarse monticellite in sample DDH-007-3 of rectangle in "F".

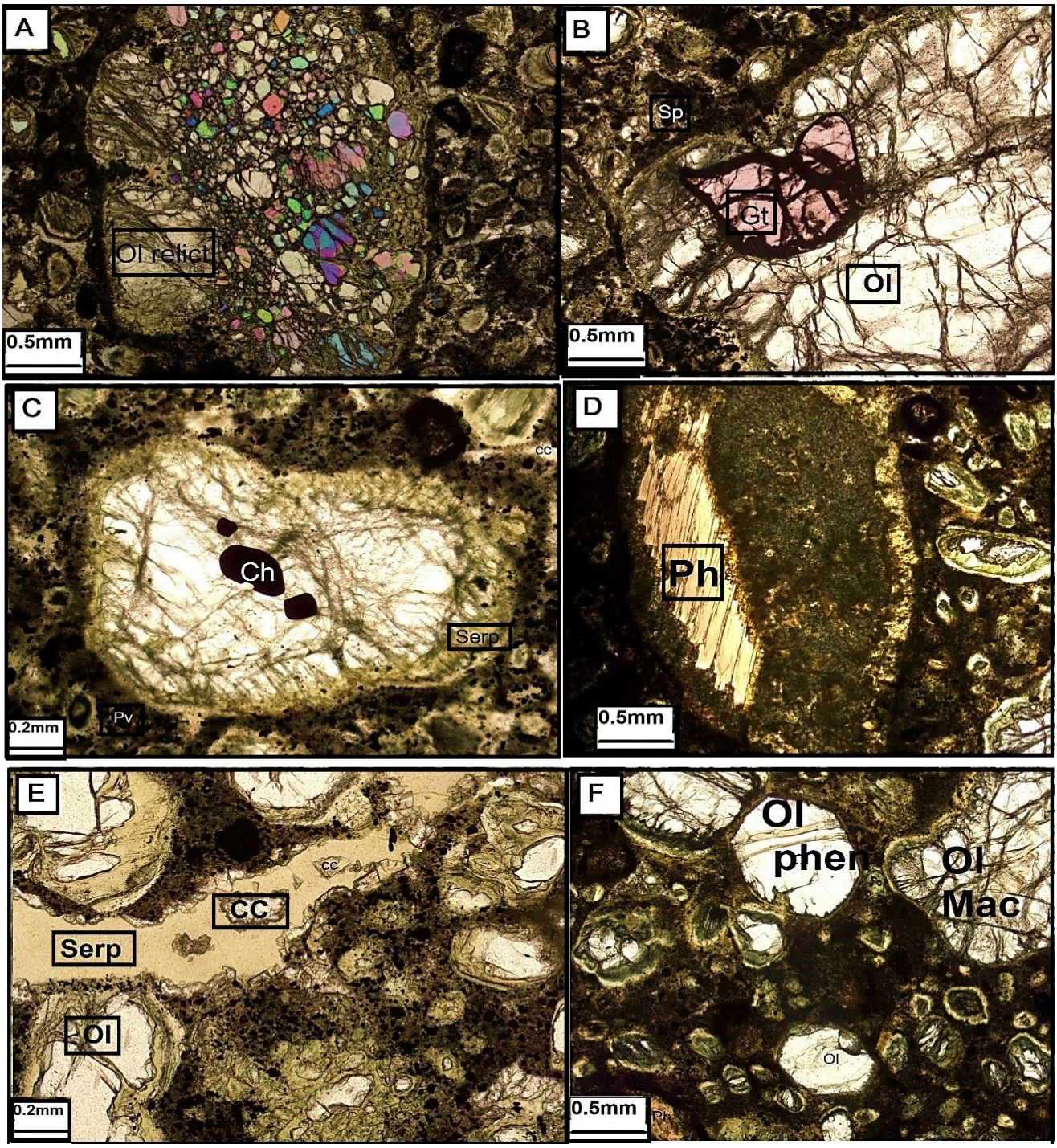

Figure 3.2: Photomicrographs of the D14 - monticellite kimberlite. Ol = olivine, Serp = Serpentine, Ph = Phlogopite, Gt = Garnet, Ch = Chromite, CC = Calcite. **(A)** A partially recrystallized olivine macrocryst showing neoblasts and relict of original macrocryst under XPL light from (DDH-0016-4). **(B)** Olivine macrocryst with garnet (pyrope) inclusion (DDH-007-1). **(C)** Olivine macrocryst with spinel (chromite) inclusions and serpentinized margins (DDH-007-1). **(D)** Chemically zoned partially resorbed phlogopite macrocryst, partially pseudomorphed mostly by Fe-Ti oxides, perovskite and monticellite (DDH-016-4). **(E)** Cryptocrystalline serpentine with calcite tablets (mesostasis) segregated from oxide-silicate groundmass and serpentinized olivine macrocryst margins (DDH-011-2). **(F)** Unaltered to partially altered euhedral-subhedral olivine phenocrysts and partially to completely serpentinized olivine micro-phenocrysts. (Left corner) shows a partially resorbed phlogopite phenocryst (DDH-014-4).

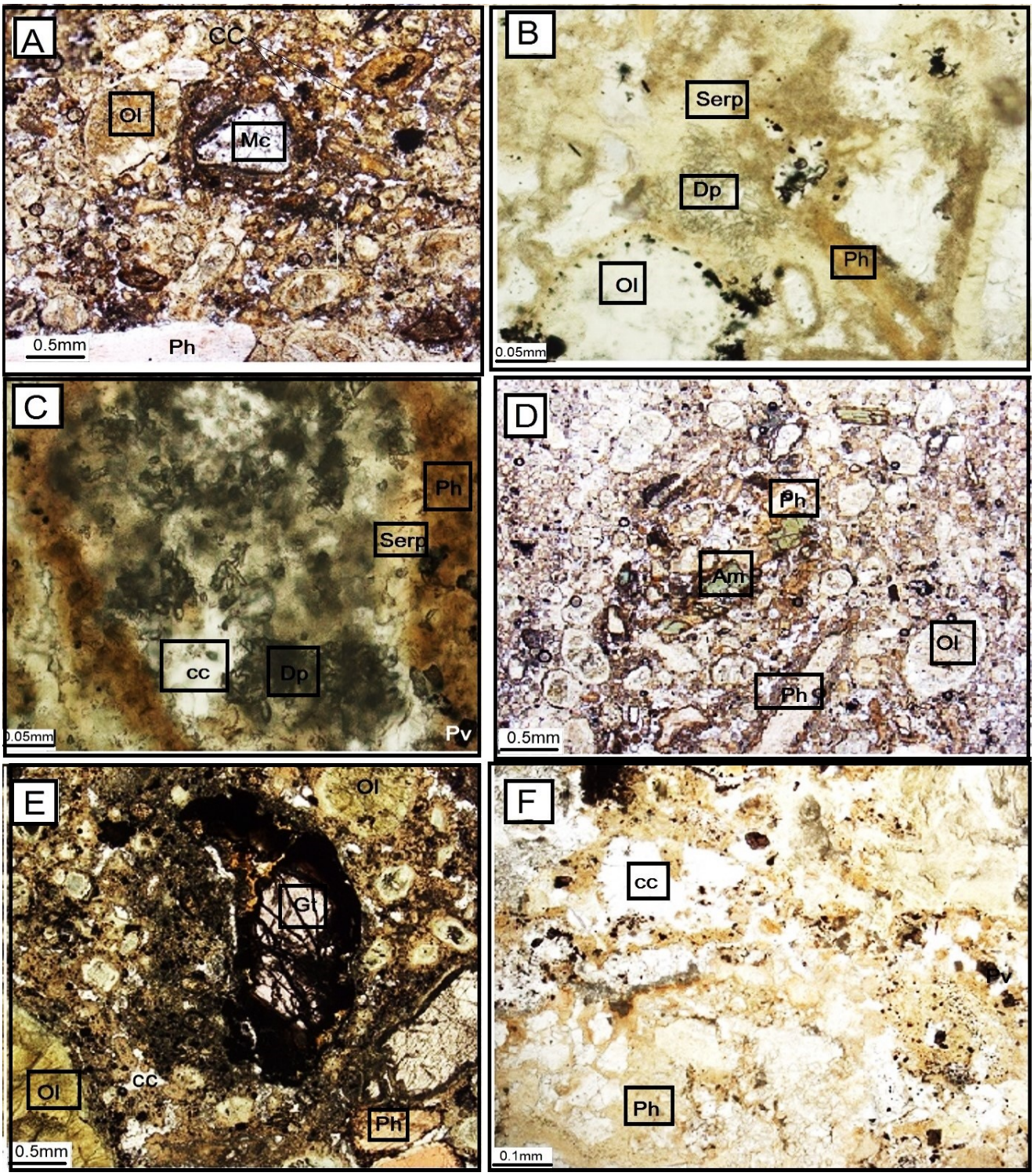

Figure 3.3: Photomicrographs of the D17- serpentinized phlogopite kimberlite. Ol = Olivine, Serp = Serpentine, Ph = Phlogopite, Gt= Garnet, Mc= Magmaclast, CC= calcite, Dp= Diopside, Pv= Perovskite. **(A)** Cored magmaclasts (pyroclasts) with unaltered olivine core and poorly developed crystalline rim, serpentinized olivine and phlogopite macrocrysts (DDH-006-1). **(B)** Microlitic diopside enclosed by deuteric serpentine and olivine macrocrysts (DDH-006-2). **(C)** Microlitic diopside pocket enclosed serpentine all set in a phlogopite rich groundmass (DDH-011-4). **(D)** Green amphibole crustal xenocrysts, serpentinized olivines and phlogopite (DDH-006-1). **(E)** Kelyphytic garnet xenocrysts, serpentinized olivines and chemically zoned phlogopite phenocrysts all set in a poorly segregationary groundmass (DDH-006-2). **(F)** Discrete calcite segregated from the phlogopite rich matrix. Notice how the phlogopite groundmass is altered (brown) (DDH-011-4).

3.5. MACROCRYSTIC CALCITE KIMBERLITE DYKES

Precursor macrocrystic dykes [DDH-012-4 and DDH-015-6]

The precursor macrocrystic kimberlite dykes are intruded into the schist country rock (Appendix A). They contain anhedral olivine macrocrysts that are up to 4mm in length. Olivine macrocrysts show little to no alteration, although some olivine macrocrysts show evidence of late-stage hydrothermal fluids (Fig. 3.4e). Phlogopite macrocrystic are rare and when present are typically resorbed. Also present are minor anhedral Mg-ilmenite macrocrysts that are up to ~1mm. When present the ilmenite macrocrysts are sometimes replaced by <0.1mm perovskite overgrowths along grain boundaries (Fig. 3.4b). Subhedral to euhedral olivine phenocrysts are abundant (Fig. 3.5b). Pseudomorphed phlogopite phenocrysts are common. The groundmass is slightly segregationary. The groundmass consists of abundant calcite with common equant Fe-Ti -oxides and lesser perovskite. Serpentine and accessory monticellite, phlogopite laths and apatite make the rest of the groundmass assemblage and all are set in a matrix set in a matrix comprising of tabular interlocking interstitial calcite grains

Internal macrocrystic dykes [DDH-002-4; DDH-011-7; DDH-013-3; DDH-014-2]

Internal macrocrystic kimberlite dykes are intruded into D11 (DDH-002-4; DDH-014-2) and D17 (DDH-011-7; DDH-013-3) (Appendix A). Samples DDH-002-4 and DDH-014-2 are macrocrystic more macrocrystic than the sparsely macrocrystic varieties (DDH-011-7 and DDH-013-3). All samples have remarkably unaltered olivine macrocrysts (Fig. 3.4a; c), with some olivine macrocrysts hosting pyrope inclusions (Fig. 3.4a). Kelyphytized garnet were observed in all specimens. Phlogopite macrocrysts are rare and when present are usually partially resorbed. Dykes intruded into the D17 – serpentinized phlogopite kimberlite (DDH-013-3 and DDH-011-7) have a higher proportion of phlogopite macrocrysts compared to those intruded into the major intrusive bodies (D13 and D14). Euhedral to subhedral olivine phenocrysts are common and show little to no alteration. Phlogopite phenocrysts are rare with most being resorbed. Texturally the groundmass is uniform and contains abundant equant euhedral Fe-Ti oxides and perovskite. Also present minor monticellite and apatite and accessory phlogopite all set in a calcite.

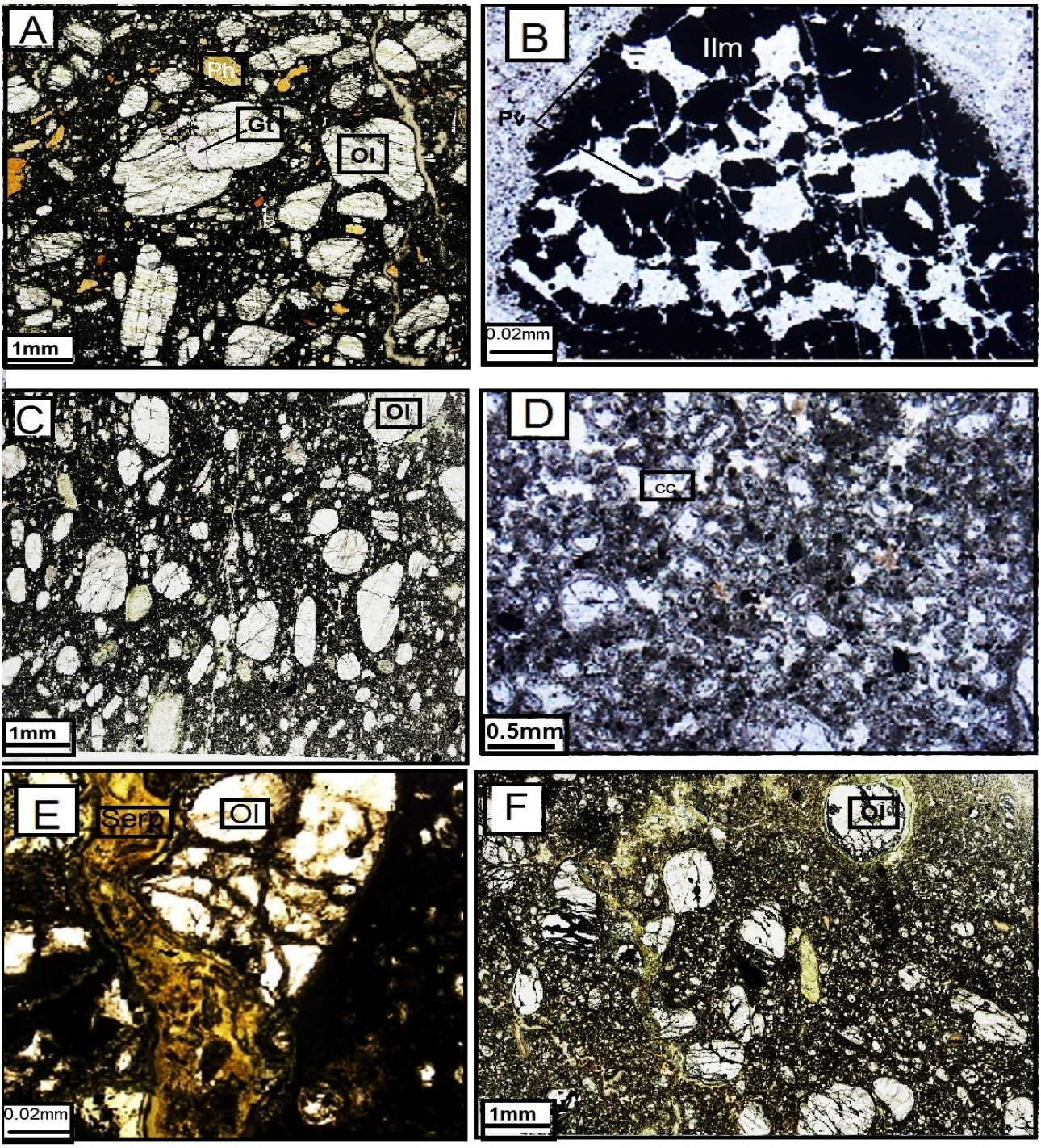

Figure 3.4: Photomicrographs of the macrocrystic calcite kimberlite dykes. Ol = olivine, Serp = Serpentine, Ph = Phlogopite, Pv= Perovskite, Ilm= Ilmenite. (a) Olivine phenocrysts and macrocrysts, (on the centre) one macrocryst contains garnet inclusion. Also seen are phlogopite macrocryst and phenocrysts all set in a very opaque -rich calcite uniformly textured groundmass in DDH-002-4. (b) Partially resorbed Ilmenite macrocryst replaced by overgrowths of perovskite and tabular calcite. (c) Olivine macrocrysts and phenocrysts in a very opaque-rich calcite uniformly textured groundmass in DDH-014-2. (d) Calcite segregations in DDH-014-2 (e) late stage hydrothermal fluid cutting through olivine macrocryst in DDH-0014-2 (f) olivine macrocrysts and phenocrysts with late stage hydrothermal fluids.

3.6. APHANITIC CALCITE KIMBERLITE DYKES

Precursor aphanitic dykes [DDH-014-6; DDH-008-8]

Samples DDH-014-6 and DDH-008-8 are aphanitic kimberlite dykes that are intruded into the schist country rock (Appendix A). The precursor aphanitic kimberlite dykes contain abundant euhedral to subhedral olivine (micro)-phenocrysts that exhibit minor alteration. Phlogopite laths are rare and mostly resorbed. A kelyphytized garnet xenocrysts was observed in one specimen (DDH-014-6) (Fig. 3.5c). The groundmass is poorly segregationary, containing residual pools of abundant cryptocrystalline serpentine and calcite segregated from the silicate-oxide assemblage which consists of abundant euhedral to subhedral Fe-Ti oxides (<0.3mm), with minor perovskite (<0.2mm), accessory acicular apatite and phlogopite laths. The groundmass assemblage is set in a matrix dominated by abundant tabular interlocking calcite grains. The precursor dykes are classified as poorly segregationary aphanitic serpentine calcite kimberlites.

Internal aphanitic dykes [DDH-001-2; DDH-008-4; DDH-0012-3; and DDH-013-3]

Samples (DDH-001-2, DDH-08-4 and DDH-012-3) represent dykes intruded into D11, whereas sample DDH-013- 3 represent a single intrusion into the D17 – serpentinized phlogopite kimberlite (Appendix A). Mineralogically the internal aphanitic dykes are similar to the precursor dykes and only vary by the relative abundances of their groundmass assemblage. DDH-013-3 contains a relatively higher abundance of phlogopite, whereas DDH-008-4 is relatively more perovskite-rich, and samples DDH-001-2 and DDH-012-3 are richer in opaque-oxides (Fig. 3.5). Texturally all samples have a uniformly textured groundmass. Similarly to the precursor aphanitic calcite kimberlites, the internal kimberlite dykes are all characterized by a calcite rich matrix. Mineralogically the respective aphanitic kimberlite dykes are classified as follows:

Opaque- rich calcite kimberlites [DDH-001-2 and DDH-012-3].

Serpentine calcite kimberlite [DDH- 008-8 and DDH-014-6]

Phlogopite-rich calcite kimberlite [DDH-013-3].

Perovskite-rich calcite kimberlite [DDH-008-4].

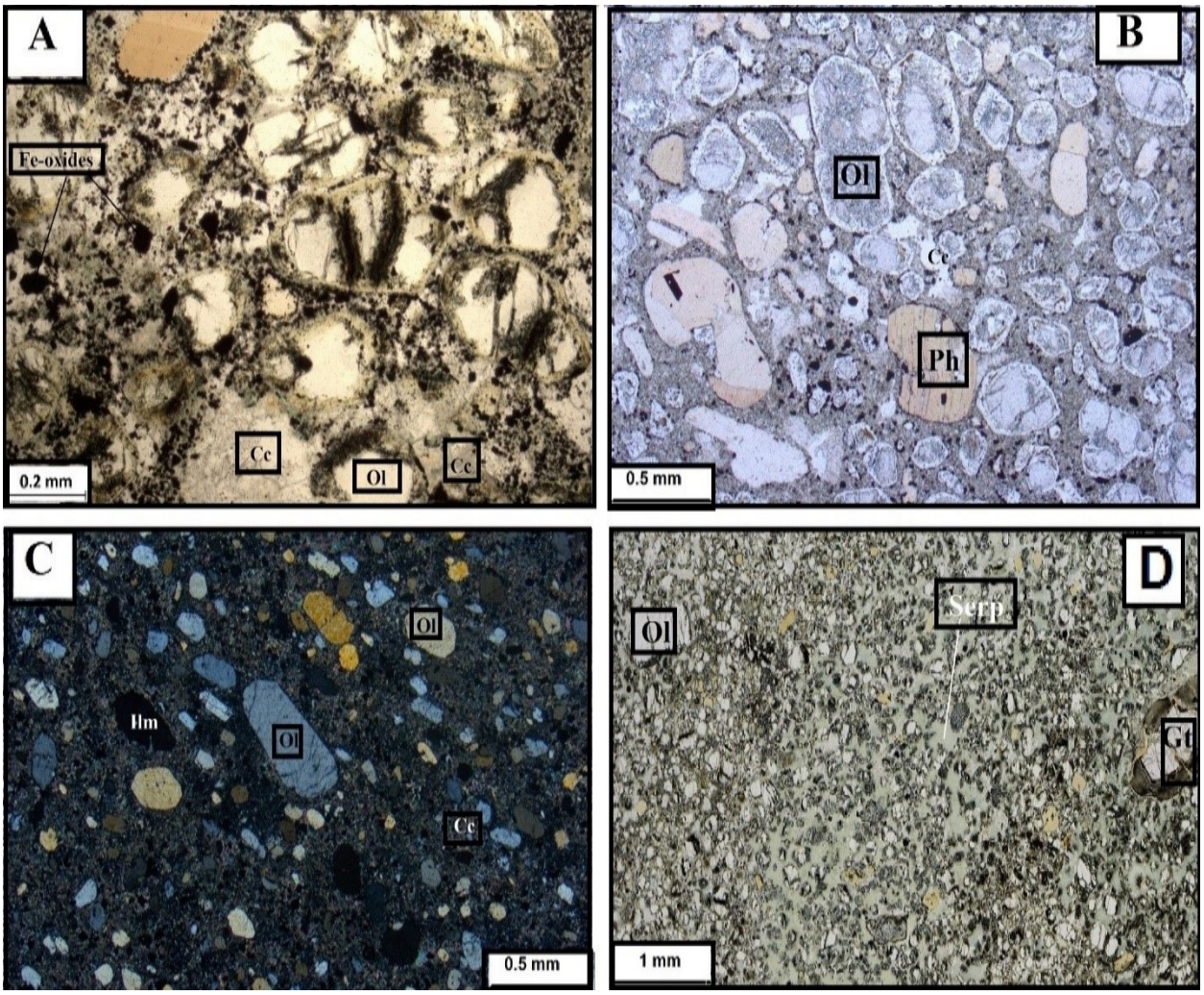

Figure 3.5: Photomicrographs of different aphanitic calcite kimberlite dykes. Ol = olivine, Serp = Serpentine, Ph = Phlogopite, Ilm= Ilmenite. (A) Olivine (micro) - phenocrysts, phlogopite phenocrysts (orange) with an Fe-Ti oxide rich matrix of calcite (DDH-001-2). (B) Phlogopite and olivine (micro) - phenocrysts set in calcite matrix with abundant Fe-Ti oxides (DDH-013-3). (C) Unaltered olivine (micro) - phenocrysts and abundant Fe-oxides all set in calcite rich groundmass (DDH-008-4). (D) Olivine and phlogopite (micro) - phenocrysts all set in a serpentine calcite -rich matrix (DDH-008-8).

Table 3.1: Summary of salient petrographic features in kimberlite intrusions from the eastern lobe of the Du Toitspan kimberlite pipe. Modal proportion for the macrocrysts were determined using 1000-point counts. Oliv = olivine, phl=phlogopite, carb=carbonate, mont =monticellite, grt = garnet, pv =perovskite, serp = serpentine, op-ox = opaque oxides, cpx = clinopyroxene, ap =apatite.

PHASE	Sample ID	Macrocrysts (> 0.5 - 10mm)			(Micro)-phenocrysts	Groundmass and accessory phase	Textural-genetic classification	Mineralogical classification
		Ol (%)	Phl (%)	Other			Skinner and Clement (1985)	Clement and Skinner (1979)
D13	DDH-001-3	23	5	Ilm	oliv, phl	phl, mont, op-ox, pv, carb, serp	Uniform, Macrocrystic	Phlogopite kimberlite
	DDH-007-3	27	3	Ilm	oliv, phl	phl, mont, op-ox, pv, carb, serp	Uniform, Macrocrystic	Phlogopite kimberlite
	DDH-008-3	25	6	Ilm	oliv, phl	phl, mont, op-ox, pv, carb, serp	Uniform, Macrocrystic	Phlogopite kimberlite
D14	DDH-006-3	10	3		oliv, phl	mont, carb, op-ox, pv, phl	Uniform, sparsely macrocrystic	Monticellite kimberlite
	DDH-007-1	20	3		oliv, phl	mont, carb, op-ox, pv, phl, ap	Uniform, Macrocrystic	Monticellite kimberlite
	DDH-011-2	20	3		oliv, phl	mont, carb, op-ox, pv, phl	Uniform, Macrocrystic	Monticellite kimberlite
	DDH-014-4	35	5		oliv, phl	mont, carb, phl, op-ox, pv, serp, ap	Uniform, Macrocrystic	Monticellite kimberlite
	DDH-015-5	12	5		oliv, phl	mont, carb, phl, op-ox, pv, serp,	Uniform, sparsely macrocrystic	Monticellite kimberlite
	DDH-016-3	16	5		oliv, phl	mont, carb, phl, op-ox, pv, serp, ap	Uniform, Macrocrystic	Monticellite kimberlite
	DDH-016-4	25	10		oliv, phl	mont, carb, op-ox, pv, phl	Uniform, Macrocrystic	Monticellite kimberlite
D17	DDH-006-1	28			oliv	phl, serp, carb, op-ox, pv, cpx	Uniform, Macrocrystic	Serpentinized phlogopite kimberlite
	DDH-006-2	30			oliv	phl, carb, op-ox, pv, serp, cpx	Uniform, Macrocrystic	Serpentinized phlogopite kimberlite
	DDH-011-4	25	6		oliv, phl	phl, serp, carb, op-ox, pv, cpx	Segregationary, Macrocrystic	Serpentinized phlogopite kimberlite
	DDH-013-4	24	5		oliv, phl	phl, serp, carb op-ox, pv, cpx	Segregationary, Macrocrystic	Serpentinized phlogopite kimberlite
	DDH-016-5	26	7		oliv, phl	phl, serp, carb, op-ox, pv, cpx	Segregationary, Macrocrystic	Serpentinized phlogopite kimberlite
DYKE	DDH-002-4	39	5	Grt	oliv, phl	carb, op-ox, pv, serp, mont, phl, ap	Uniform, Macrocrystic	Opaque-rich calcite kimberlite
	DDH-011-7	10	8	Grt	oliv, phl	carb, op-ox, pv, serp, mont, phl, ap	Uniform, Sparsely Macrocrystic	Opaque-rich calcite kimberlite
	DDH-013-2	15	8	Grt	oliv, phl	carb, op-ox, pv, serp, mont, phl, ap	Uniform, Sparsely Macrocrystic	Opaque-rich calcite kimberlite
	DDH-012-4	28			oliv, phl	carb, op-ox, pv, serp, mont, phl, ap	Slightly segregationary, Macrocrystic	Opaque-rich calcite kimberlite
	DDH-014-2	30			oliv, phl	carb, op-ox, pv, serp, mont, phl, ap	Uniform, Macrocrystic	Opaque-rich calcite kimberlite
	DDH-015-6	26	3	Grt	oliv, phl	carb, op-ox, pv, serp, mont, phl, ap	Slightly segregationary, Macrocrystic	Opaque-rich calcite kimberlite

Table 3.1 : Continued

Dyke	DDH-001-2	1	-	-	oliv, Ilm	carb, op-ox, pv, serp, phl, ap	Uniform, Aphanitic	Opaque-rich calcite kimberlite
	DDH-008-4	-	-	-	oliv, pv	carb, pv, op-ox, pv, serp, ap	Uniform, Aphanitic	Perovskite-rich calcite kimberlite
	DDH-008-8	-	-	-	oliv	carb, serp, op-ox, pv, phl, mont, ap	Uniform, Aphanitic	Serpentine calcite kimberlite
	DDH-012-3	-	-	-	oliv, Ilm	carb, op-ox, pv, serp, phl, ap	Uniform, Aphanitic	Opaque-rich calcite kimberlite
	DDH-013-3	-	-	-	oliv, phl	carb, phl, op-ox, pv, serp, ap	Uniform, Aphanitic	Phlogopite-rich calcite kimberlite
	DDH-014-6	-	-	-	oliv	carb, serp, op-ox, pv, mont, phl, ap	Uniform, Aphanitic	Serpentine calcite kimberlite

CHAPTER 4: MINERAL CHEMISTRY

4.1. INTRODUCTION

Olivine and phlogopite are the dominant (micro) - phenocrysts and macrocrysts in this suite of rocks (chapter 3; Table 3.1). Therefore these minerals were selected for analysis because there have been several studies demonstrating that valuable insights about kimberlite petrogenesis can be obtained from the chemical analysis of olivine (e.g., Giuliani, 2018 and references therein), while others have demonstrated that insight about metasomatism in kimberlite source regions which has direct implications on kimberlite petrogenesis can be determined from chemical analysis of their constituent phlogopite (e.g., Grégoire, et al., 2002; Griffin et al., 2003; Giuliani et al., 2016; Kargin et al., 2019). Electron probe microanalysis (EPMA) analysis procedure, and specifications of apparatus used for analysis are given in Appendix C.1. The objective of the analysis was to determine if any compositional variability exists among olivines and phlogopites in the various kimberlite intrusions, and whether or not this variability can provide insights pertaining to their petrogenesis. Samples of the D17 – serpentinized phlogopite kimberlite were excluded from analysis due to their perverse alteration. The data of analysed grains are reported in Tables 4.1 – 4.3.

4.2. OLIVINE

Olivine cores in the D13 – phlogopite kimberlite have forsterite contents ranging from Fo_{91-93} (Fig. 4.1; Table 4.1). Their macrocrystic cores are on average slightly more magnesian (~ Fo_{93}) than the phenocrystic cores (~ Fo_{91}) (Table 4.1). Olivine phenocrystic cores in the D13 – phlogopite kimberlite are on average slightly higher in CaO (~ 0.05 wt. %) compared to the macrocrystic cores (CaO = 0.017 wt. %). NiO concentrations in both the phenocrystic and macrocrystic cores are similar and range from 0.3 – 0.5 wt. %. On average olivine phenocrystic and macrocrystic cores in the D14 – monticellite kimberlites have ~Fo_{92}; NiO (0.17 – 0.46 wt. %) and CaO (0.02 - 0.07 wt. %) (Table 4.1). Phenocrystic cores in the macrocrystic calcite dykes show a wider compositional range (Fo_{87-93}) compared to the other macrocrystic varieties. Macrocrysts in the macrocrystic calcite kimberlites show a similar range in forsterite content (Fo_{87-93}). The macrocrystic calcite kimberlite dykes on average NiO (~ 0.4 wt. %) and CaO (~0.02 wt. %) concentrations are similar in both phenocrystic and macrocrystic olivines. In the aphanitic calcite kimberlite varieties, several analysed olivine cores in the phlogopite-rich calcite

kimberlite (DDH-013-3) and the serpentine calcite dyke (DDH-014-6) are Fe-rich (Fo_{84-87}) (Fig. 4.1). Although MgO-rich cores (Fo_{90-92}) are more abundant in this suite of kimberlites. Olivines with Fe-rich cores are characterized by lower NiO (< 0.3 wt. %) (Fig. 4.1), whereas those with MgO-rich cores generally have NiO > 0.4 wt. %. CaO concentrations in the aphanitic calcite kimberlites show a similar range (0.02 – 0.06 wt. %) with the macrocrystic varieties. Olivine rims for all kimberlite intrusions in this study have near constant forsterite contents (Fo88-89) (Table 4.1; 4.2), with variable NiO (0.1 – 0.45 wt. %) and CaO <0.1 wt. % (Fig. 4.1; Table 4.1 and 4.2). Although olivine rims in macrocrystic calcite kimberlite dykes with noticeably higher CaO (up to 0.41 wt. %) are present (Fig. 4.1b). In general, olivine compositions in the aphanitic calcite kimberlite dykes are much more variable than those in the macrocrystic varieties. When present Fe-rich olivine cores have NiO, Fo and CaO concentration that fall within the field of South African megacrysts, whereas MgO-rich olivine cores have NiO, Fo and CaO compositions that fall within the field of sheared and granular peridotites from the Kaapvaal craton (Giuliani et al., 2018).

Table 4.1: Average major element compositions in olivines from selected samples representative of the D13 - phlogopite kimberlite and the D14 - monticellite kimberlites reported as wt. %. n= number of analysis.

Phase	**D13 -phlogopite kimberlite**					**D14 - monticellite kimberlite**				
Grain size/type	Phenocryst		Macrocryst		Relict	Phenocryst		Macrocryst		Neoblasts
	Cores	Rims	Cores	Rims	Cores	Cores	Rims	Cores	Rims	Cores
	n = 4	*n = 4*	*n = 18*	*n = 5*	*n = 5*	*n = 8*	*n = 8*	*n = 13*	*n = 11*	*n = 5*
SiO_2	41	40.62	41.2	40.4	41.4	41.3	40.6	41.59	40.9	40.6
TiO_2	0.01	0.03	0.02	0.02	0.05	0.01	0.04	0.03	0.02	0.035
Al_2O_3	0.01	0.01	0.01	0.01	0.07	0.01	0.02	0.02	0.02	0.005
Cr_2O_3	0.04	0.06	0.03	0.04	0.07	0.04	0.07	0.02	0.05	0.02
FeO	8.44	12.12	7.33	11.65	9.83	7.03	11.24	7.47	11.08	11.25
MnO	0.09	0.12	0.08	0.13	0.12	0.07	0.13	0.09	0.11	0.145
MgO	49.8	47.1	51.1	47.6	48.8	51.2	47.86	50.64	48.1	48.7
CaO	0.03	0.08	0.02	0.05	0.075	0.02	0.06	0.02	0.06	0.03
NiO	0.43	0.21	0.4	0.23	0.385	0.45	0.3	0.4	0.3	0.335
Total	99.93	100.4	99.96	100.1	100.8	100.1	100.3	100.3	100.6	100.1
calculated for four oxygens										
Si	1.016	1.012	1.029	0.999	1.055	0.999	0.999	1.004	1.001	1.000
Ti	0.000	0.001	0.000	0.000	0.001	0.000	0.001	0.001	0.000	0.001
Al	0.000	0.000	0.000	0.000	0.002	0.000	0.001	0.000	0.001	0.000
Cr	0.001	0.001	0.001	0.001	0.001	0.001	0.001	0.000	0.001	0.000
Fe	0.167	0.244	0.147	0.241	0.178	0.142	0.231	0.151	0.227	0.233
Mg	1.755	1.695	1.817	1.755	1.573	1.847	1.755	1.822	1.755	1.754
Mn	0.002	0.002	0.002	0.003	0.002	0.001	0.003	0.002	0.002	0.003
Ca	0.001	0.002	0.001	0.001	0.002	0.001	0.002	0.001	0.002	0.001

Table 4.1 : Continued

Ni	0.008	0.004	0.008	0.005	0.007	0.009	0.006	0.008	0.006	0.007
Sum	2.95	2.96	3.00	3.00	2.82	3.00	3.00	2.99	2.99	3.00
Fo%	91.3	87.4	93.4	90.2	89.8	92.9	88.4	92.4	88.6	88.3

Table 4.2: Average major element compositions in olivines from selected samples representative of the various macrocrystic and aphanitic calcite kimberlite dykes reported as wt. %. n= number of analysis.

Phase	**Macrocrystic dykes**				**Aphanitic dykes**	
Grain size /type	**Phenocrysts**		**Macrocrysts**		**Phenocrysts**	
	Cores	**Rims**	**Cores**	**Rims**	**Cores**	**Rims**
	n = 5	*n = 5*	*n = 7*	*n = 7*	*n = 15*	*n = 14*
SiO_2	41.2	40.5	41.5	40.7	41	40.7
TiO_2	0.02	0.03	0.01	0.05	0.04	0.04
Al_2O_3	0.01	0.01	0.01	0.02	0.02	0.02
Cr_2O_3	0.04	0.07	0.03	0.05	0.04	0.04
FeO	8.94	11.3	7.32	11.3	10.3	11.7
MnO	0.1	0.15	0.1	0.13	0.1	0.13
MgO	49.1	47.7	50.4	47	47.8	47
CaO	0.02	0.07	0.02	0.09	0.05	0.06
NiO	0.41	0.24	0.42	0.32	0.37	0.28
Total	99.78	100.07	99.82	99.57	99.75	99.96
calculated for four oxygens						
Si	1.01	1	1.01	1.01	1.01	1.01
Ti	0.000	0.001	0.000	0.001	0.001	0.001
Al	0.000	0.000	0.000	0.001	0.001	0.001
Cr	0.001	0.001	0.001	0.001	0.001	0.001
Fe	0.184	0.233	0.15	0.233	0.213	0.242
Mn	0.002	0.003	0.002	0.003	0.002	0.003
Mg	1.80	1.75	1.84	1.73	1.75	1.73
Ca	0.001	0.002	0.000	0.003	0.001	0.002
Ni	0.008	0.005	0.008	0.006	0.007	0.006
Sum	3.01	3	3.02	2.98	2.99	2.99
Fo %	90.7	88.3	92.5	88.2	89.2	87.7

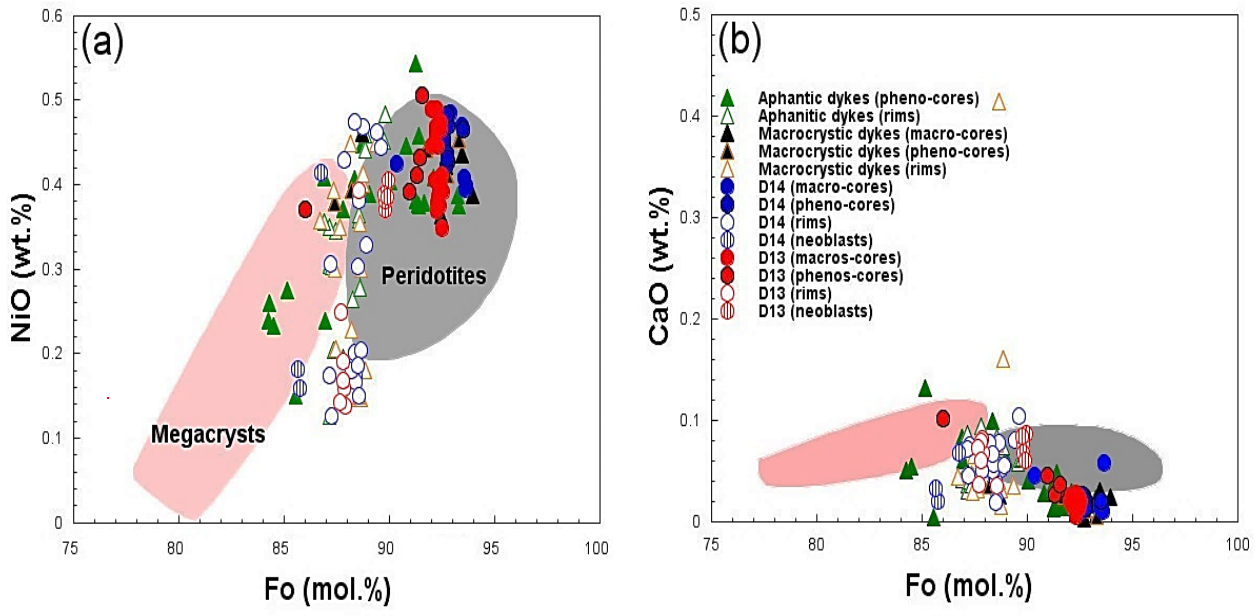

Figure 4.1: Bivariate plot of Fo. (mol. %) vs NiO and CaO in olivines from selected samples representative kimberlite intrusions from the eastern lobe of the Du Toitspan kimberlite pipe. Fields for South African megacrysts and peridotites from the compilation of Giuliani (2018).

4.3. PHLOGOPITE

The major kimberlite intrusions (D13 – Phlogopite kimberlite and D14 – Monticellite kimberlite) generally have Cr- poor (< 0.3 wt. %) phlogopite phenocrysts and groundmass cores (Table 4.3; Fig. 4.2). Cores in the phlogopite macrocrysts are relatively more Cr-rich (> 0.3 wt. %) (Table 4.3). The D13 – Phlogopite kimberlite is characterized by F-rich (F > 0.5 wt. %) phlogopite phenocrysts and groundmass cores (Fig. 4.2). Phlogopites in the D13 – phlogopite kimberlite are noticeably lower in K_2O (average phlogopite phenocrysts ~ 9.38 wt. %; average phlogopite groundmass ~ 8.95 wt. %) in comparison with the other intrusive phases (Fig. 4.2e; Table 4.3). Although their macrocrystic cores tend to be slightly higher in K_2O (>10 wt. %) (Fig. 4.2e). Phlogopite in the D14 – monticellite kimberlite describes a wider range in F concentrations, with one phenocryst core and a subset of macrocryst rims from sample DDH -016-4 having high fluorite contents (>0.5 wt.%) (Fig. 4.2; Table 4.3). Both the D13 – phlogopite kimberlite and D14 - monticellite kimberlites have low TiO_2 (< 2 wt. %) with slightly more variable Al_2O_3 contents that range from 9.3 -12.7 wt. % in the D13- phlogopite kimberlite and from 10.6 -18 wt. % in the D14 – monticellite kimberlite (Fig. 4.2b). The major kimberlite intrusive phases show a similar range in Mg# (85 – 93 wt. %) (Fig. 4.2c). The D13 – phlogopite show slightly lower K_2O in most groundmass and phenocrystic phlogopite cores with slightly lower K_2O and higher F concentrations are comparable to highly metasomatized mafic xenoliths (e.g., glimmerites,

MARIDs and PICs) (Fig.4.2). There is a subset of F-rich macrocrystic rims in the D14 – monticellite kimberlite fall outside the field of highly metasomatized mafic xenoliths (Fig.4.2). Cr_2O_3 concentrations in the macrocrystic and aphanitic calcite dykes average ~1.1 wt. % and ~1.9 wt. % respectively (Fig. 4.2a). Both the macrocrystic and aphanitic dykes have F-poor (<0.5 wt. %) phlogopites (Fig.4.2). Phlogopite and in both the macrocrystic and aphanitic dykes have similar K_2O (~ 9.6 – 11.9 wt. %) and Mg# (~85 – 94 wt. %). The macrocrystic calcite kimberlite dykes are characterized by a broader range in TiO_2 (0.5 – 4.6 wt. %), and a limited range in Al_2O_3 (10.6 – 14.8 wt. %) compared to the aphanitic calcite kimberlite dykes. The aphanitic calcite kimberlite dykes have TiO_2 ranging from 0.3 – 3.6 wt. % and relatively more variable Al_2O_3 (9.6 – 18.6 wt.%). Some Al-poor phlogopite cores tend to also be Fe-rich (i.e., follow the ferriphlogopite trend instead of the Al-eastonite trend), although Al-Fe and Al-Ti typically shows intra- and inter – intrusion overlap.

In general, phlogopite microcrysts (phenocrysts and groundmass) in the D13– phlogopite kimberlite are slightly poorer in K_2O and richer in F compared to most analysed phlogopite grains from the other kimberlite intrusions. These generally fall within the range of highly metasomatized mafic xenoliths and some within the overlap field between peridotites and highly metasomatized mafic xenoliths (Fig. 4.2e). Both the macrocrystic and aphanitic dykes have phlogopite compositions that fall within the overlapping field of peridotites and highly metasomatised xenoliths.

Table 4.3: Average major elements in phlogopite from selected samples representative of different kimberlite intrusions from the eastern lobe of the Du Toitspan kimberlite pipe
n = number of analyses.

Phase	D13 - Phlogopite kimberlite				D14 - Monticellite kimberlite				Aphanitic calcite kimberlite dykes			Macrocrystic calcite kimberlite dykes		
Grain size	Groundmass	Phenocrysts	Macrocrysts		Groundmass	Phenocryst	Macrocrysts		Groundmass	Phenocrysts		Phenocrysts	Macrocryst	
one	Cores	Cores	Cores	Rims	Cores	Cores	Cores	Rims	Cores	Cores	Rims	Cores	Cores	Rims
	n = 5	*n =3*	*n = 2*	*n = 2*	*n = 3*	*n = 3*	*n = 7*	*n = 5*	*n = 2*	*n = 5*	*n = 7*	*n = 12*	*n= 3*	*n = 7*
SiO_2	41.70	41.60	42.20	42.30	39.10	41.90	41.80	40.30	36.00	40.60	39.80	41.30	41.50	39.90
TiO_2	0.82	1.50	0.71	0.82	0.87	0.25	1.07	2.82	1.04	2.59	2.04	1.74	1.50	2.87
Al_2O_3	9.21	9.88	12.20	10.90	17.10	10.40	11.70	13.00	18.20	14.10	14.80	12.60	12.80	13.90
Cr_2O_3	0.04	0.14	0.63	0.24	0.01	0.11	0.36	0.61	0.00	0.90	0.38	0.36	0.40	1.16
FeO	8.22	6.82	5.13	6.88	3.68	6.95	5.84	5.54	4.51	4.20	4.17	4.54	4.92	4.61
MnO	0.06	0.06	0.01	0.04	0.04	0.04	0.02	0.05	0.08	0.01	0.06	0.03	0.02	0.01
MgO	26.70	26.40	25.30	24.90	26.50	25.60	25.10	23.70	23.80	23.90	24.20	24.50	24.00	22.80
CaO	0.09	0.07	0.01	0.01	0.07	0.01	0.01	0.02	0.21	0.01	0.01	0.01	0.01	0.22
Na_2O	0.12	0.21	0.24	0.17	0.05	0.11	0.19	0.21	0.08	0.34	0.26	0.24	0.18	0.23
K_2O	8.95	9.38	10.10	9.47	9.26	10.70	10.10	10.10	10.00	10.20	10.40	10.50	10.70	10.60
F	0.89	1.15	0.32	0.69	0.37	0.62	0.46	1.00	0.44	0.30	0.36	0.43	0.37	0.34
Total	96.41	96.68	96.59	96.16	96.93	96.32	96.53	96.92	94.23	97.14	96.3	96.05	96.24	96.43
H_2O*	3.47	3.34	3.72	3.53	3.65	3.55	3.64	3.34	3.40	3.69	3.62	3.62	3.65	3.62
(OH=F)	0.37	0.48	0.13	0.29	0.16	0.26	0.19	0.42	0.19	0.13	0.15	0.18	0.16	0.14
Total calc.	99.50	99.54	100.2	99.40	100.4	99.61	99.97	99.84	97.45	100.71	99.77	99.49	99.73	99.91
Calculated For 11 oxygens														
Si	3.22	3.21	3.27	3.29	3.07	3.27	3.25	3.17	2.99	3.17	3.15	3.24	3.26	3.16
Ti	0.05	0.09	0.04	0.05	0.05	0.01	0.06	0.17	0.06	0.15	0.12	0.10	0.09	0.17
Al	0.42	0.45	0.56	0.50	0.79	0.48	0.54	0.60	0.89	0.65	0.69	0.58	0.59	0.65
Cr	0.00	0.00	0.02	0.01	0.00	0.00	0.01	0.02	0.00	0.03	0.01	0.01	0.01	0.04

Table 4.3: Continued

Fe	0.53	0.44	0.33	0.45	0.24	0.45	0.38	0.36	0.31	0.27	0.28	0.30	0.32	0.31
Mn	0.00	0.00	0.00	0.00	0.00	0.00	0.00	0.00	0.01	0.00	0.00	0.00	0.00	0.00
Mg	3.07	3.04	2.92	2.88	3.10	2.98	2.91	2.78	2.95	2.79	2.85	2.86	2.81	2.70
Ca	0.01	0.01	0.00	0.00	0.01	0.00	0.00	0.00	0.02	0.00	0.00	0.00	0.00	0.02
Na	0.01	0.02	0.02	0.01	0.00	0.01	0.01	0.02	0.01	0.03	0.02	0.02	0.01	0.02
K	0.44	0.46	0.50	0.47	0.46	0.53	0.50	0.51	0.53	0.51	0.52	0.52	0.54	0.54
cation sum	7.75	7.71	7.66	7.66	7.72	7.74	7.67	7.62	7.47	7.29	7.34	7.32	7.31	7.28
Mg#	85.3	87.3	89.8	86.6	92.8	86.8	88.5	88.4	90.4	91.0	91.2	90.6	89.7	89.8

H_2O* calculated by stoichiometry

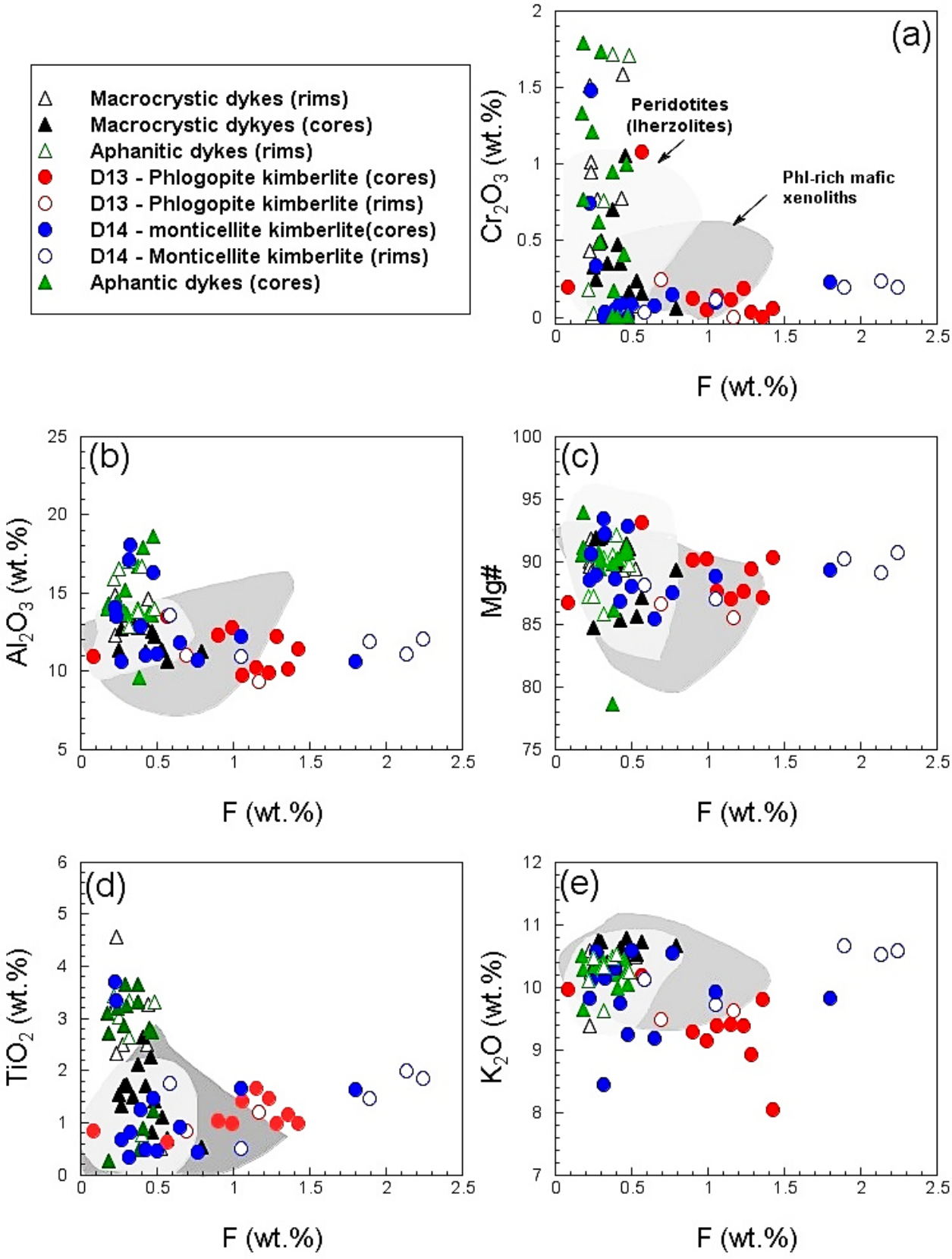

Figure 4.2: Bivariate plot of Fluorine vs selected oxides in phlogopites from selected samples representative of kimberlite intrusions from the eastern lobe of the Du Toitspan kimberlite pipe. Fields of phlogopite-rich mafic xenoliths and peridotite from the compilation of Giuliani et al. (2016).

CHAPTER 5: MAJOR ELEMENT GEOCHEMISTRY

5.1. INTRODUCTION

Samples representative of kimberlite intrusion from the eastern lobe of the Du Toitspan kimberlite pipe were analysed for major elements using X-ray fluorescence (XRF). Analysed elements include; Si, Ti, Al, Fe, Mn, Mg, Ca, Na, K and P. CO_2 concentrations were determined separately using the Karbonat - bombe method of Birch (1981). Sample preparation, procedure and standards used for analysis are given in Appendix C.2 – C.4. All major element data are given in Tables 5.1 – 5.3. The data are plotted in Figures 5.1 – 5.2 without normalisation to a volatile-free basis. Because of their explosive emplacement style, kimberlites magmas usually incorporate and assimilate crustal xenoliths (e.g., Clement, 1982, Sparks et al., 2006; Skinner, 2008). Because crustal contamination is perhaps the most prevalent compositional modification process affecting kimberlites and its effects are recognisable in major elements, as a first order assessment for compositional modification, the effects of crustal contamination for the different kimberlite intrusions are evaluated. Although considerable attempts were made to select only unaltered kimberlite fragments for analysis following the removal of all visible xenogenic material with the aid of high magnification binocular microscope, it is still possible that some (micro-) xenoliths could have been overlooked and inadvertently crushed during sample preparation. Also, given the abundance of shale and siltstone xenoliths in some of the collected samples for analysis, considering their low melting points (< 700 °C) (e.g., Kilinc, 1989) the possibility of partial (or complete) assimilation of crustal xenoliths by the host kimberlite could have acted as an additional source of contamination. The different kimberlite intrusions are evaluated for crustal contamination using the contamination index (C.I.) of Clement (1982). The C.I. is calculated on a weight % basis using the expression below:

$$C.I. = (SiO_2 + Al_2O_3 + Na_2O) / (2K_2O + MgO).$$

The C.I. is widely applied in quantifying the degree of crustal contamination and extent of weathering experienced by kimberlite intrusions. Since crustal rocks are characterized by higher Na_2O, Al_2O_3 and SiO_2 contents and lower K_2O and MgO contents compared to kimberlites, enrichment in Na_2O, Al_2O_3 and SiO_2 relative to K_2O and MgO is considered to be indicative of crustal contamination (Clement, 1982). Clement (1982) considered kimberlites with C.I > 1.5 to be crustally contaminated and those with C.I <1.5 to be contamination free. However, subsequent

studies recommend a 'bottom cut-off' of 1 as being more reliable in discriminating between contaminated and contamination-free kimberlite samples (e.g., Mitchell, 1986; Nowicki et al., 2008; Kjarsgaard et al., 2009).

Table 5.1: Bulk rock major element compositions of samples representative of the D13 - phlogopite kimberlite and the D14 - monticellite kimberlite from the eastern lobe of the Du Toitspan kimberlite pipe.

Phase	D13 - phlogopite kimberlites			D14 - monticellite kimberlites						
Texture	Macrocrystic			Macrocrystic						
Sample ID	DDH-001-3	DDH-007-3	DDH-008-3	DDH-006-3	DDH-007-1	DDH-011-2	DDH-014-4	DDH-015-5	DDH-016-3	DDH-016-4
SiO_2	31.9	34.1	33.8	33.0	30.3	28.7	32.4	31.1	32.0	28.7
TiO_2	1.50	1.62	1.58	1.33	2.17	1.49	1.73	1.44	1.37	2.32
Al_2O_3	5.07	3.34	3.68	2.21	2.34	2.11	2.62	1.84	2.34	2.40
FeO_T	8.38	9.33	9.30	8.35	9.76	8.72	9.64	8.91	8.64	9.83
MnO	0.14	0.16	0.16	0.14	0.16	0.15	0.17	0.15	0.14	0.17
MgO	29.6	33.5	32.2	29.0	28.6	31.7	31.7	30.2	34.6	30.2
CaO	7.28	7.58	6.76	9.15	9.58	10.39	9.02	9.00	6.99	9.56
Na_2O	0.21	0.46	0.53	0.13	0.13	0.05	0.17	0.34	0.24	b. d
K_2O	3.56	2.48	2.86	2.05	2.12	1.64	1.88	1.69	2.00	1.45
P_2O_5	1.04	0.97	0.81	1.29	1.16	2.06	0.930	2.17	1.31	1.24
SO_3	0.03	0.04	0.02	0.04	0.06	0.05	0.09	0.05	0.06	0.13
Cr_2O_3	0.17	0.19	0.18	0.23	0.22	0.18	0.23	0.23	0.23	0.19
NiO	0.12	0.14	0.14	0.14	0.13	0.13	0.14	0.14	0.14	0.12
H_2O-	0.53	0.43	0.23	0.53	0.55	0.35	0.18	0.55	0.32	0.51
LOI	9.62	4.80	6.78	11.3	12.1	11.9	8.50	11.6	9.13	12.7
Total	99.1	99.1	99.0	98.8	99.3	99.6	99.4	99.4	99.5	99.5
*H_2O^+	4.62	3.2	3.38	3.43	5.68	4.76	3.73	6.26	5.00	7.77
*CO_2	5.01	1.60	3.40	7.87	6.39	7.13	4.77	5.37	4.14	4.93
*C.I.	1.01	0.98	1.00	1.07	1.00	0.88	0.99	0.99	0.90	0.95
*FeO	6.65	7.4	7.38	6.62	7.74	6.91	7.64	7.06	6.85	7.8
*Fe_2O_3	1.00	1.11	1.11	0.99	1.16	1.04	1.15	1.06	1.03	1.17
*Mg#	88.8	89.0	88.6	88.6	86.8	89.1	88.1	88.4	90.0	87.3

* calculated

Mg# = [atomic Mg/ (Mg+ Fe^{2+}], assuming $Fe_2O_3/FeO = 0.15$

C.I. = ($SiO_2 + Al_2O_3 + Na_2O$)/ ($MgO + 2K_2O$).

CO_2 determined from karbonate Bombe analysis method of Birch (1981).

LOI: loss on Ignition (900°C).

$H_2O^+ = LOI - CO_2$

Table 5.2: Bulk rock major element compositions of samples representative of the D17 – serpentinized phlogopite kimberlite from the eastern lobe of the Du Toitspan kimberlite pipe.

Phase	Serpentinized Phlogopite kimberlite D17				
Texture	Macrocrystic	Macrocrystic	Macrocrystic	Macrocrystic	Macrocrystic
Sample ID	DDH-006-1	DDH-006-2	DDH-011-4	DDH-013-4	DDH-016-5
SiO_2	34.7	34.3	36.1	34.4	34.1
TiO_2	1.64	1.53	1.66	1.95	1.62
Al_2O_3	3.85	4.07	4.29	3.95	3.29
FeO_T	8.17	7.97	8.45	8.26	8.21
MnO	0.14	0.15	0.14	0.13	0.14
MgO	22.1	21.6	23.1	24.6	25.8
CaO	8.54	9.23	7.48	6.74	7.78
Na_2O	0.95	0.90	0.87	1.17	0.31
K_2O	2.20	2.43	2.86	2.71	3.21
P_2O_5	0.96	0.95	1.15	1.15	0.97
SO_3	0.82	0.78	0.03	0.04	0.04
Cr_2O_3	0.16	0.16	0.17	0.22	0.18
NiO	0.11	0.10	0.11	0.10	0.12
H_2O-	2.92	3.03	2.62	3.26	0.76
LOI	11.29	11.77	10.01	10.39	12.36
Total	98.53	98.97	99.07	99.06	98.92
*C.I.	1.49	1.49	1.43	1.32	1.17
*Mg#	85.9	85.9	86.0	87.0	87.6
*Fe_2O_3	0.97	0.95	1.00	0.98	0.98
*FeO	6.48	6.32	6.70	6.55	6.51
H_2O^+	n.d	n.d	n.d	n.d	n.d
CO_2	n.d	n. d	n.d	n.d	n.d

* calculated

Mg# = [atomic Mg/ (Mg+ Fe^{2+}], assuming $Fe_2O_3/FeO = 0.15$

C.I. = $(SiO_2 + Al_2O_3 + Na_2O)/ (MgO + 2K_2O)$.

CO_2 determined from karbonate Bombe analysis method of Birch (1981).

Loss on Ignition (900°C).

H_2O^+ = LOI - CO_2

n.d = not determined

Table 5.3: Bulk rock major element compositions of samples representative of various macrocrystic and aphanitic calcite kimberlite dykes from the eastern lobe of the Du Toitspan kimberlite pipe.

Phase	Dykes						Dykes					
Texture	Macrocrystic calcite kimberlites						Aphanitic calcite kimberlites					
Sample ID	DDH-002-4	DDH-011-7	DDH-012-4	DDH-013-2	DDH-014-2	DDH-015-6	DDH-001-2	DDH-008-4	DDH-008-8	DDH-012-3	DDH-013-3	DDH-014-6
SiO_2	32.9	30.0	28.3	32.0	30.5	25.7	26.6	25.3	26.1	29.5	28.5	26.0
TiO_2	1.46	2.24	2.3	1.89	1.73	2.41	1.01	3.30	2.03	0.82	1.78	2.40
Al_2O_3	1.97	2.10	1.72	2.14	2.20	1.83	0.970	2.99	1.27	0.810	2.34	1.81
FeO_T	9.05	9.26	10.8	9.16	9.43	10.3	9.84	9.90	9.86	8.86	10.0	10.6
MnO	0.16	0.16	0.18	0.15	0.16	0.18	0.17	0.23	0.17	0.15	0.18	0.18
MgO	36.0	32.1	31.3	28.8	36.2	33.0	35.5	27.6	33.2	34.0	28.2	30.0
CaO	5.77	8.37	9.30	8.65	8.78	9.85	10.3	16.6	9.51	8.71	11.35	11.7
Na_2O	0.06	0.10	0.08	0.04	0.07	0.03	b.d	0.46	0.03	0.22	0.03	0.01
K_2O	1.01	1.86	1.15	2.14	0.96	0.94	0.17	1.05	0.83	0.24	1.41	1.00
P_2O_5	0.90	1.19	0.97	1.14	1.35	0.98	2.05	1.33	0.69	1.76	2.00	2.40
SO_3	0.07	0.12	1.06	0.10	0.16	0.68	0.14	0.08	0.86	0.31	0.17	0.82
Cr_2O_3	0.25	0.22	0.23	0.21	0.24	0.19	0.10	0.41	0.16	0.09	0.22	0.18
NiO	0.16	0.13	0.13	0.14	0.13	0.11	0.14	0.07	0.10	0.13	0.12	0.11
H_2O-	0.19	0.34	0.13	0.43	0.26	0.27	0.10	0.21	0.15	0.50	0.21	0.17
LOI	8.80	11.6	11.8	12.4	7.57	13.0	12.7	10.1	14.8	13.9	12.5	12.0
Total	98.8	99.8	99.4	99.3	99.8	99.5	99.8	99.6	99.7	100	99.0	99.3
*H_2O+	5.40	6.50	3.05	5.01	3.59	5.27	5.11	3.31	6.88	7.45	5.21	4.64
*CO_2	3.40	5.12	8.70	7.39	3.98	7.74	7.63	6.82	7.90	6.42	7.30	7.30
*C.I.	0.92	0.90	0.89	1.03	0.86	0.79	0.77	0.97	0.79	0.89	0.99	0.87
*FeO	7.17	7.34	8.59	7.26	7.47	8.15	7.8	7.85	7.81	7.03	7.95	8.4
*Fe_2O_3	1.08	1.1	1.29	1.09	1.12	1.22	1.17	1.18	1.17	1.05	1.19	1.26
*Mg#	90.0	88.6	86.7	87.6	89.6	87.8	89.0	86.3	88.3	89.6	86.3	86.4

* calculated

Mg# = [atomic Mg/ (Mg+ Fe^{2+}], assuming $Fe_2O_3/FeO = 0.15$

C.I. = ($SiO_2 + Al_2O_3 + Na_2O$)/ ($MgO + 2K_2O$).

CO_2 determined from karbonate Bombe analysis method of Birch (1981).

Loss on Ignition (900°C).

$H_2O^+ = LOI - CO_2$

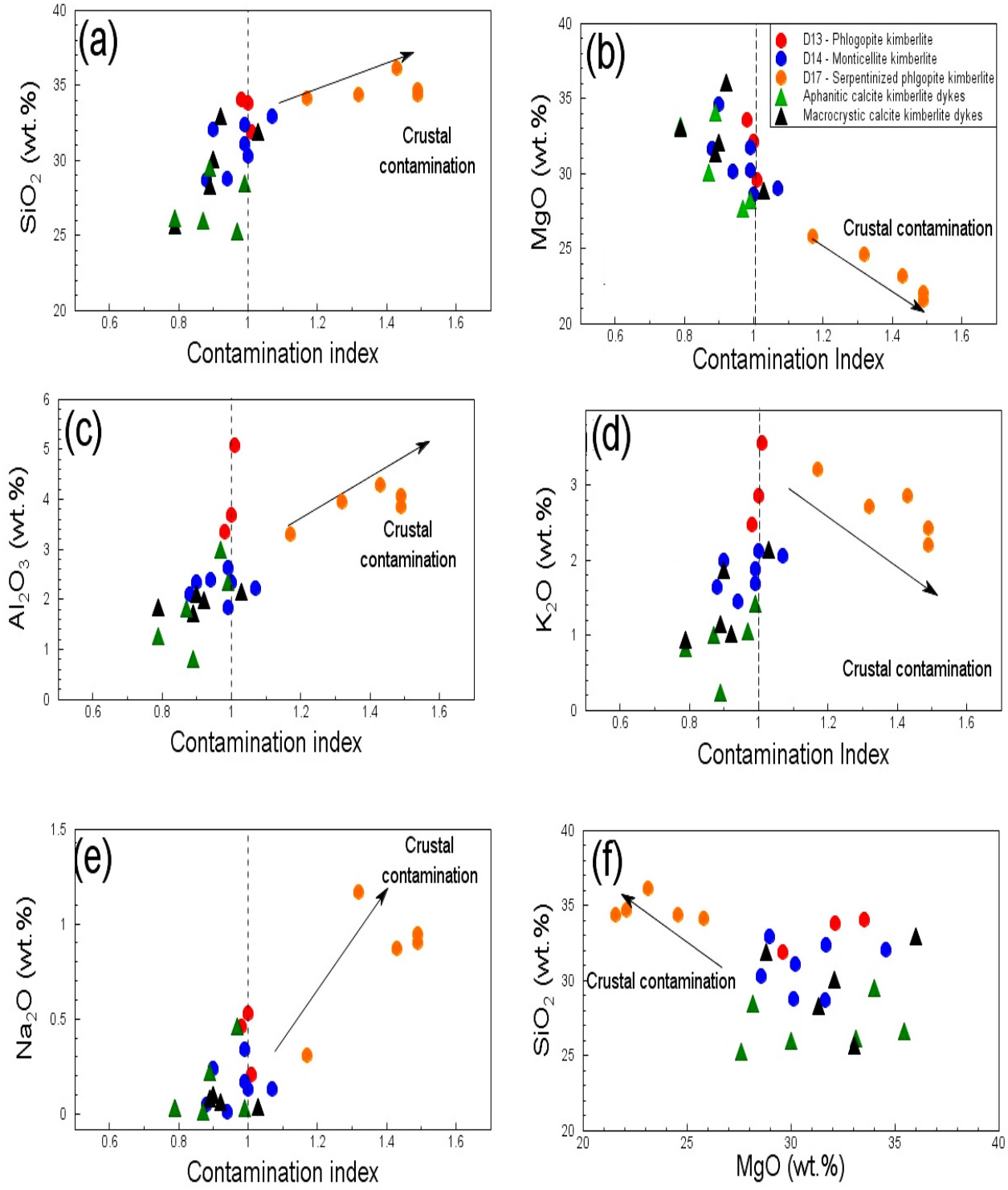

Figure 5.1: Bivariate plots showing the effects of crustal contamination in samples representative of different kimberlite intrusions from the eastern lobe of the Du Toitspan kimberlite pipe. (a – c) C.I. vs (SiO_2, Al_2O_3, Na_2O, MgO and K_2O). (f) SiO_2 vs MgO. Arrows show correlation trends consistent with crustal contamination. Dashed vertical lines (a – e) discriminate between crustally contaminated and contamination free samples.

The D17 – serpentinized phlogopite kimberlite samples have higher contamination indices (C.I. = 1.17 – 1.49) compared to other kimberlite intrusions in this study (Fig 5.1). The high C.I. in the D17 – serpentinized are negatively correlated with K_2O and MgO, and correlate positively with Na_2O, SiO_2 and Al_2O_3 (Fig. 5.1a – e). Further evidence in support of crustal contamination in the D17 – serpentinized phlogopite kimberlite is seen from their strong negative SiO_2-MgO (le Roex et al., 2003). Consequently, samples for the D17 – serpentinized phlogopite kimberlite are omitted from further discussion. Samples for other intrusions have C.I < 1 (Fig. 5.1; Table 5.1-5.3), except for three (DDH-006-3, DDH-013-2, and DDH-001-3) with C.I. ranging from 1 – 1.07 (Table 5.2). The negligibly raised C.I. in the aforementioned samples is ascribed to either negligible crustal contamination or is perhaps indicative of the chemical leaching of Mg^{2+} and K^{+} cations during the serpentinization of olivine and phlogopite (Mitchell, 1986). These samples are treated with caution and will be assessed further in section 7.2.

5.2. D13- PHLOGOPITE KIMBERLITES

D13 – phlogopite kimberlite samples have SiO_2 (31.86 – 34.06 wt. %) and MgO (29.60 – 33.53 wt. %) (Table 5.1; Fig. 5.2a). FeOT (total) concentrations are near identical in all samples (FeO_T = 8.30 – 9.33 wt. %) (Fig. 5.2b). Corresponding Mg numbers [atomic 100 × Mg^{2+}/ (Mg^{2+} + Fe^{2+}); Fe_2O_3/FeO =0.15] shows a limited range (88.6 – 90.0) (Table 5.1). CaO concentrations in all three samples are similar (6.76 – 7.58 wt. %.). P_2O_5 (0.97 - 1.04 wt. %) and TiO_2 (1.50 – 1.62 wt. %) also show similar range for all samples. CO_2 content are significantly variable (1.60 - 5.01 wt. %) (Table 5.1). Al_2O_3 (3.34 - 5.07 wt. %) and K_2O (2.34 – 3.56 wt. %) in all samples are high and are positively correlated when plotted together (Fig. 5.2e). Al_2O_3 and K_2O also show strong negative correlation with MgO (Fig. 5.2e). The K_2O concentrations in the D13 – phlogopite kimberlite samples are considerably higher than previously reported for kimberlites from the Kimberley cluster (le Roex et al., 2003). The K_2O contents in the D13 – phlogopite kimberlite are instead comparable with group II kimberlites (Becker and le Roex, 2006). High Al_2O_3 (5.07 wt. %) in sample DDH-001-3 falls outside the field of group I and II kimberlites; while the other two samples have Al_2O_3 contents that are comparable with group I kimberlites from the Kimberley cluster (le Roex et al., 2003). In general, apart from for high K_2O contents, the D13 – phlogopite kimberlites have major elements compositions that fall within the overlapping field between group I and II kimberlites.

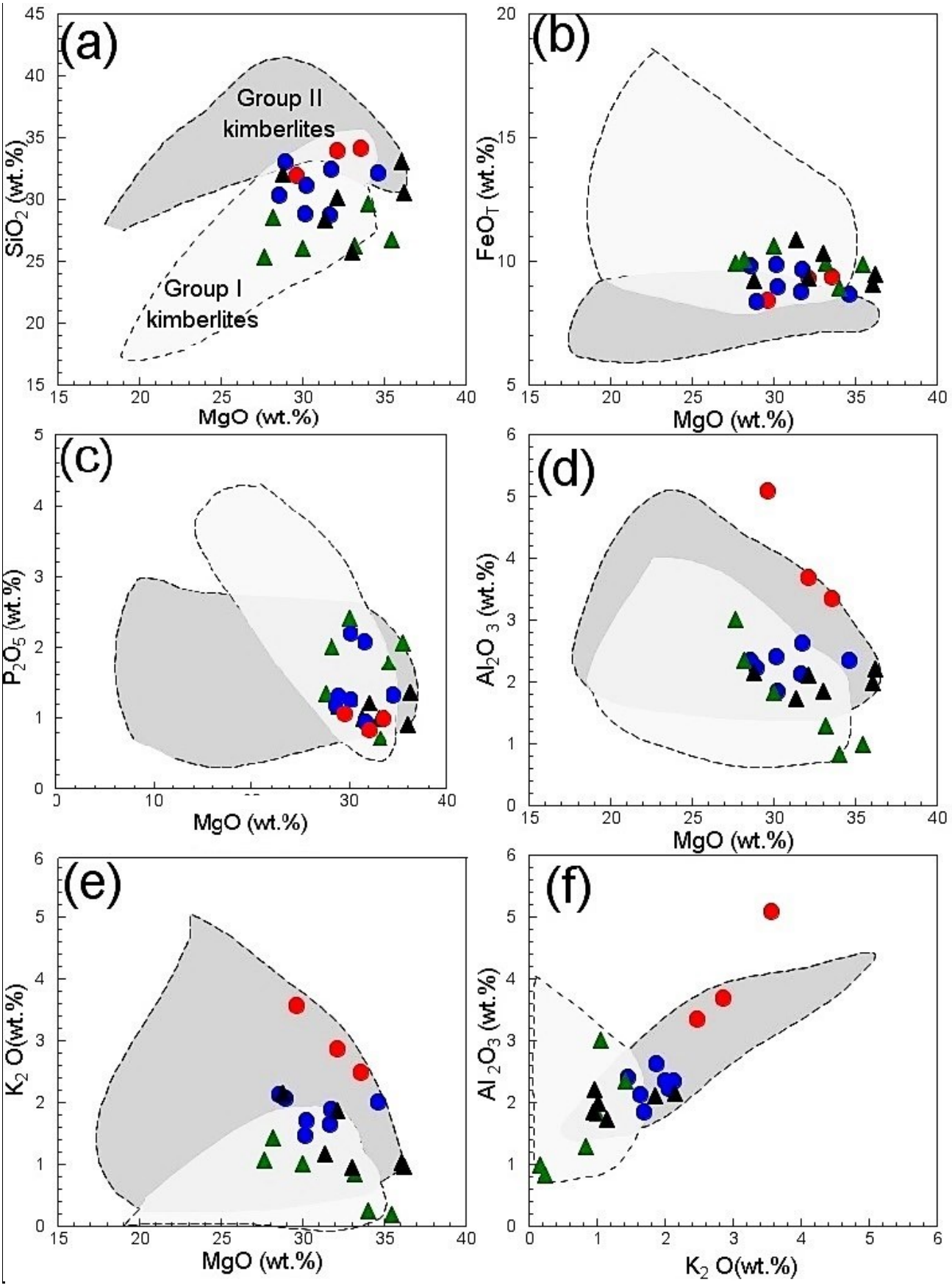
(a)
Group II kimberlites
Group I kimberlites
SiO2 (wt.%)
MgO (wt.%)
(b)
FeOT (wt.%)
MgO (wt.%)
(c)
P2O5 (wt.%)
MgO (wt.%)
(d)
Al2O3 (wt.%)
MgO (wt.%)
(e)
K2O(wt.%)
MgO (wt.%)
(f)
Al2O3 (wt.%)
K2O(wt.%)

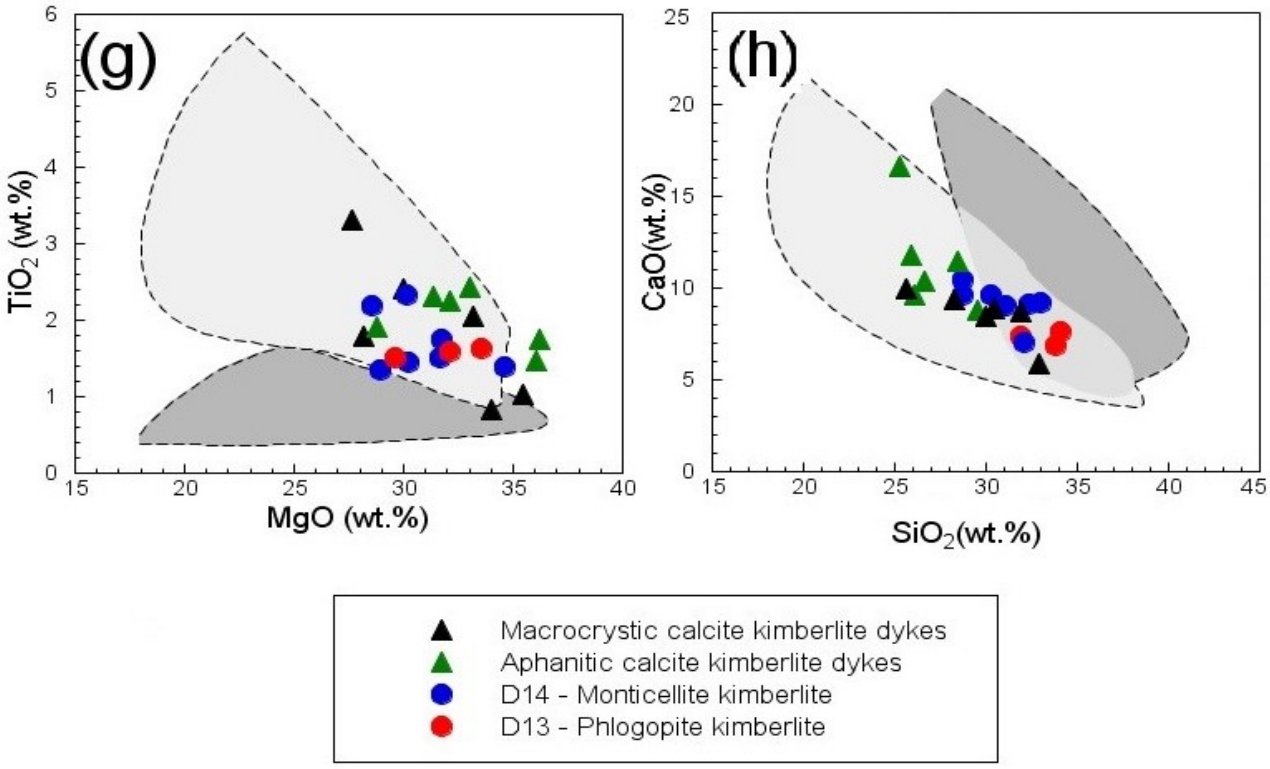

Figure 5.2 : Bivariate plots of MgO vs selected major elements in samples representative of kimberlite intrusions from the eastern lobe of the Du Toitspan kimberlite pipe. The field of group I kimberlites is from le Roex et al (2003). The field of group II kimberlites is from Becker and le Roex (2006).

5.3. D14 - MONTICELLITE KIMBERLITE

D14 – monticellite kimberlite samples have SiO2 (28.7 - 32.8 wt. %) and MgO (28.6 - 36.2 wt. %) (Fig. 5.2a). FeO_T (8.35 – 9.83 wt. %) and Mg numbers (0.86-0.90) similar to those in the D13 – phlogopite kimberlites (Fig. 5.2b; Table 5.1). CaO contents (7.0 – 10.4 wt. %) are higher than those in the D13 – phlogopite kimberlite. The D14 – monticellite kimberlites have lower Al_2O_3 (1.84 – 2.62 wt. %) and K_2O (1.88 – 2.12 wt. %) contents compared to the D13 – phlogopite kimberlite. TiO_2 (1.33 - 2.32 wt. %) and P_2O_5 (0.93 – 2.17 wt. %) show limited ranges, respectively (Table 5.1). Apart from samples with >2 wt.% K_2O (DDH-006-3, DDH-007-1 and DDH-015-5), major elements in the D14 – monticellite kimberlite have concentrations that fall within the overlapping field between group I and II kimberlites (Fig. 5.2).

5.4. MACROCRYSTIC CALCITE KIMBERLITE DYKES

The macrocrystic calcite kimberlites dykes have SiO_2 (28.82 – 36.03 wt. %) and MgO (28.82 – 36.03 wt. %) ranges that are comparable to those in the D14 monticellite kimberlite (Table 8; Fig. 5.2a). FeO_T (8.35 – 9.83) and Mg numbers (0.86 - 0.90) ranges are also similar to those in those in the D14 – monticellite kimberlite (Table 5.3). CaO contents show a slightly broader range (5.77-9.85 wt. %) compared to the D14 – monticellite kimberlite (Table 5.3). Al_2O_3 and K_2O are generally <2 wt. %, with Al_2O_3 >2.1 wt. % in the sparsely macrocrystic kimberlite samples (DDH-011-7 and DDH-013-2). P_2O_5 (0.90 – 2.05 wt. %) is slightly variable (Fig. 5.2c). The macrocrystic calcite kimberlite dykes have a narrow range in TiO_2 (1.73 – 2.41 wt. %) which is similar with the D14 – Monticellite kimberlite. Generally, the macrocrystic calcite kimberlite dykes show very little intra- intrusion variability and have major element concentrations that are almost indistinguishable from those in the D14 – monticellite kimberlites.

5.5. APHANITIC CALCITE KIMBERLITE DYKES

The aphanitic calcite kimberlite dykes have lower SiO2 (25.26 - 28.47 wt. %) compared to the macrocrystic varieties. Their MgO (27.63 - 35.46 wt. %) range is similar to that of the macrocrystic varieties (Fig. 5.2; Table 5.3). The wide range in MgO contents in the aphanitic calcite kimberlite dykes is extended by the highly magnesian (MgO >34 wt. %) in the opaque-rich calcite kimberlite dykes. The aphanitic calcite kimberlite dykes have a similar range to the macrocrystic varieties but are slightly skewed towards higher values (Table 5.3). Their Mg numbers range from 86.4 -90.0, with the highest values in the opaque-rich calcite kimberlite dykes (Mg# ~90). The opaque- rich calcite kimberlites are slightly lower in Al_2O_3 (<1.1 wt. %) and TiO2 (<1 wt. %) compared to the other aphanitic calcite dykes with higher Al_2O_3 (1.27 – 2.99 wt. %) and TiO_2 (1.78 – 3.30 wt. %) concentrations. The opaque-rich calcite kimberlite dykes also have <1 wt. % K2O, whereas the other dykes tend to have slightly higher >1 wt. % K_2O concentrations (Table 5.3). The perovskite –rich calcite kimberlite (DDH-008-4) is characterized by noticeably higher CaO (16.56 wt. %) and TiO_2 (3.30 wt. %) and concentrations compared to the other dykes in this study.

CHAPTER 6: TRACE ELEMENT GEOCHEMISTRY

6.1. INTRODUCTION

Trace elements occur in very low concentrations in rocks, usually constituting less than 0.1 wt. %, i.e. less than 1000 part per million (ppm) (Rollinson, 1993). Trace elements typically substitute for major elements in rock forming minerals, although in rare instances they may constitute stoichiometric components in some rock forming minerals (e.g., Zircon) (Rollinson, 1993). Trace elements with ionic radii or charge that is similar to major elements occupying the main crystallographic sites in minerals are known as compatible elements, whereas those with different ionic radii or charges are known as incompatible elements (Rollinson, 1993). Depending on the reason for the incompatibility (i.e., ionic radii or charge) incompatible elements are sub-divided into high field strength elements (HFSE) and large ion lithophile elements (LILE) (Rollinson, 1993). This chapter presents trace element data of samples representative of different kimberlite intrusions from the eastern lobe of the Du Toitspan kimberlite pipe. The representative samples were analysed for trace elements using the inductively coupled plasma mass spectrometry (ICP-MS) and X-ray fluorescence (XRF) analytical techniques. The full range of all analysed trace elements includes; Li, Sc, V, Cr, Co, Ni, Cu, Zn, Ga, Rb, Sr, Y, Zr, Nb, Ba, REE (La, Ce, Pr, Nd, Sm, Eu, Tb, Gd, Dy, Ho, Er, Tm, Yb, Lu), Hf, Ta, Pb, Th and U. Sample preparation, analysis procedure, and standards used for analysis are given in Appendix C.3. The trace element data of the different kimberlite intrusions is presented in Tables 6.1 and 6.2

Trace element analysis was conducted on the various kimberlite intrusions to characterise them in order to develop semi-quantiative models that are consistent with the observed variability with the aim of placing constraints on their petrogenesis. The theoretical basis for the quantitative treatment of trace elements relies on the distribution law:

$$\mathbf{D} = \frac{\mathbf{C_i^{mineral}}}{\mathbf{C_i^{melt}}}$$

Where D is the partition coefficient, C_i is the concentration of a trace element in either the mineral or the melt phase. Perhaps the greatest draw-back in the application of quantitative modelling towards the study of kimberlite petrogenesis is the absence of a complete collection of suitable mineral-melt partition coefficients (D). Thus, quantitative modelling performed on kimberlites has

often had to apply partition coefficients determined from other silica – under saturated systems (e.g., basanites, nephelinites, carbonatites etc.).

Table 6.1: Bulk rock trace element compositions for representative samples of the D13 - phlogopite kimberlite and D14 - Monticellite kimberlite from the eastern lobe of the Du Toitspan kimberlite pipe.

Phase	D13 - phlogopite kimberlite			D14 - monticellite kimberlite						
Texture	macrocrystic			macrocrystic						
Sample ID	DDH-001-3	DDH-007-3	DDH-008-3	DDH-006-3	DDH-007-1	DDH-011-2	DDH-014-4	DDH-015-5	DDH-016-3	DDH-016-4
Li	10.7	6.23	6.62	7.89	6.19	4.68	5.90	4.02	4.44	10.7
Cu	47.3	69.4	59.0	53.4	84.4	67.9	56.0	77.6	55.2	85.7
Ni	970	1141	1104	1095	1018	1086	1105	1123	1197	942
Zn	68.1	69.5	75.1	65.2	77.8	65.2	69.7	68.5	69.4	84.0
Nb	102	104	106	125	123	148	129	137	133	137
Zr	190	187	267	221	247	237	234	251	236	284
Y	15.7	15.8	15.8	12.0	15.2	14.7	14.8	11.1	11.4	15.4
Sr	811	585	688	1108	916	1644	719	1656	1142	887
Rb	130	120	105	111	103	103	80	131	105	103
U	2.52	2.61	2.54	2.66	2.19	3.71	2.91	3.42	3.21	3.17
Th	9.15	9.23	9.43	11.7	9.70	14.7	12.6	14.0	14.0	14.1
Pb	4.84	9.64	3.88	4.77	3.39	11.1	8.07	14.0	8.77	8.21
Co*	88.6	99.1	98.6	97.5	104	99.4	99.9	105	105	98.8
Cr*	1407	1500	1441	1752	1560	1535	1709	1779	1865	1499
V*	88.23	120.3	85.23	89.32	141	121	79.9	110	83.6	124
Sc*	20.5	19.6	20.8	20.1	23.0	22.1	23.3	21.3	18.5	24.1
Ba	707	836	632	797	827	981	594	1888	1037	1500
Hf	4.31	4.36	5.76	4.55	5.49	5.03	5.27	5.36	5.12	6.38
Ta	5.78	6.19	6.03	7.02	8.08	8.51	7.05	7.78	7.73	8.52
Ga	32.1	34.4	30.4	33.4	35.7	38.6	22.6	56.5	34.4	48.1
La	86.4	90.2	89.9	115	99.5	146	110	120	112	106
Ce	174	182	183	231	205	294	225	243	223	215
Pr	19.4	20.6	20.4	25.0	23.1	32.3	25.6	27.0	24.9	24.2
Nd	72.5	78.4	77.3	90.9	86.9	119	95.0	98.4	94.2	95.1
Sm	10.1	11.0	10.8	11.4	11.9	15.3	14.2	13.6	13.6	14.7
Eu	2.77	2.84	2.81	3.15	3.44	3.84	3.34	3.16	3.10	3.50
Gd	7.28	7.62	7.43	7.78	8.76	9.70	8.65	7.66	7.86	9.20
Tb	0.849	0.885	0.865	0.834	0.989	1.04	0.983	0.783	0.793	1.00
Dy	3.85	3.81	3.70	3.37	4.19	4.00	4.18	3.33	3.33	4.29
Ho	0.585	0.592	0.577	0.465	0.596	0.567	0.594	0.440	0.452	0.630
Er	1.32	1.34	1.31	0.964	1.25	1.17	1.29	0.898	0.981	1.34
Tm	0.157	0.152	0.148	0.103	0.134	0.118	0.131	0.095	0.103	0.147
Yb	0.927	0.898	0.875	0.573	0.753	0.656	0.743	0.525	0.564	0.808
Lu	0.127	0.124	0.118	0.074	0.097	0.084	0.103	0.060	0.075	0.101

Trace elements analysed by ICP-MS, except for * analysed by XRF.

Table 6.2: Bulk rock trace element compositions for the aphanitic and macrocrystic dykes from the eastern lobe of the Du Toitspan kimberlite pipe.

	calcite kimberlite dykes						calcite kimberlite dykes					
Texture	**macrocrystic**						**aphanitic**					
Sample ID	**DDH-002-4**	**DDH-011-7**	**DDH-012-4**	**DDH-013-2**	**DDH-014-2**	**DDH-015-6**	**DDH-001-2**	**DDH-008-4**	**DDH-008-8**	**DDH-012-3**	**DDH-013-3**	**DDH-014-6**
Li	1.55	2.78	7.28	9.27	7.10	7.36	2.87	17.33	5.04	4.53	6.98	3.62
Cu	56.9	78.8	58.8	73.5	53.0	56.9	50.2	116.6	46.5	46.1	53.3	101
Ni	1329	1024	1023	1067	1116	977	1129	573	784	1099	953	896
Zn	62.9	77.1	81.6	71.8	70.6	86.1	64.6	100	79.3	67.3	85.8	73.0
Nb	114	129	154	107	131	160	129	237	153	106	177	172
Zr	197	241	266	219	235	295	233	464	231	185	302	293
Y	13.3	13.1	15.4	12.7	13.7	17.1	17.6	36.4	15.6	11.9	17.2	16.1
Sr	618	711	782	801	996	896	1346	1038	1007	957	1203	1446
Rb	51.3	74.0	44.4	102.8	86.7	58.4	9.3	43.5	58.9	9.4	67.8	72.9
U	2.31	2.23	3.09	2.12	3.21	3.52	2.87	5.59	3.07	3.07	4.89	3.90
Th	9.84	8.98	15.5	8.82	12.0	16.1	13.1	24.0	13.1	10.9	20.0	14.0
Pb	0.775	4.28	6.88	4.28	11.7	7.35	8.16	7.05	7.19	11.4	9.65	11.39
Co*	108	100	111	99.9	102	106	112	77.1	104	108	98.0	104
Cr*	1808	1745	1384	1538	1918	1389	776	3235	1222	717	1735	1312
V*	67.5	112	106	121	140	108	67.4	80.6	89.4	53.2	91.8	144
Sc*	18.6	21.3	26.2	20.4	24.9	23.7	28	38.3	21.9	24.1	26.6	26.3
Ba	415	542	743	784	1856	760	711	688	937	193	866	124
Hf	4.28	5.54	6.24	4.88	5.24	6.86	4.57	10.3	5.12	3.81	6.55	6.49
Ta	6.56	8.54	10.3	6.81	7.35	10.5	4.99	14.7	8.85	4.07	9.24	9.42
Ga	19.2	25.1	27.3	33.4	56.1	27.9	26.5	32.6	35.7	84.1	29.4	39.5
La	99.7	90.9	119	90.5	112	118	150	236	127	91.4	186	127
Ce	201	192	253	189	232	244	315	476	268	204	419	255
Pr	22.3	21.8	28.9	21.3	26.3	27.9	35.4	53.1	30.0	23.4	44.7	28.8
Nd	83.0	83.3	109	80.9	98.2	111	132	199	114	87.7	164	108
Sm	11.3	11.4	16.2	10.9	14.4	17.4	17.4	27.3	15.6	12.7	23.1	16.4
Eu	3.08	2.94	3.95	2.78	3.47	4.19	4.66	7.05	3.93	3.11	5.35	3.94
Gd	7.69	7.64	9.88	7.23	8.86	10.7	11.7	17.9	10.0	7.97	13.2	10.3
Tb	0.857	0.848	1.08	0.810	0.963	1.17	1.26	2.02	1.10	0.837	1.37	1.10
Dy	3.64	3.48	4.65	3.30	4.12	5.06	5.07	8.34	4.40	3.53	5.45	4.82
Ho	0.514	0.505	0.642	0.480	0.584	0.720	0.697	1.22	0.622	0.499	0.757	0.674
Er	1.03	1.08	1.32	1.05	1.24	1.51	1.37	2.58	1.27	1.09	1.48	1.45
Tm	0.111	0.114	0.134	0.112	0.126	0.154	0.146	0.269	0.129	0.117	0.155	0.146
Yb	0.617	0.645	0.757	0.642	0.705	0.882	0.812	1.49	0.690	0.622	0.814	0.814
Lu	0.078	0.081	0.097	0.084	0.091	0.100	0.110	0.193	0.087	0.09	0.108	0.098

Trace elements analysed by ICP-MS, except for * analysed by XRF.

6.2. COMPATIBLE ELEMENTS

Ni concentrations in the macrocrystic kimberlite varieties are largely controlled by the abundance of their constituent macrocrysts. The most macrocryst – rich sample (DDH-002-4) has the highest Ni (1472 ppm) (Fig.6.1a; Table 6.1). Apart from sample DDH-002-4, Ni concentrations in the macrocrystic calcite kimberlites (Ni = 943 ppm – 1130 ppm) are indistinguishable from those in the D14 – monticellite kimberlite (933 – 1216 ppm). The D13 – phlogopite kimberlites have Ni concentrations ranging from (1079 – 1206 ppm) (Fig. 6.1a). In the aphanitic calcite kimberlite varieties, the opaque-rich calcite kimberlites are characterized by the highest Ni abundances (DDH-001-2 – Ni = 1241 ppm; DDH-012-3 – Ni = 1160 ppm). The other aphanitic calcite kimberlites have lower Ni (<1000 ppm), with the perovskite-rich calcite kimberlite (DDH-008-4) having the lowest (Ni = 598 ppm) (Fig.6.1a; Table 6.2). The D14 - monticellite kimberlites and macrocrystic calcite kimberlites have similar Cr concentrations ranging from (1384 – 1918 ppm) (Fig.6.1b; Table 6.1). The D13 - phlogopite have a slightly narrower Cr concentrations (1407 - 1500 ppm) (Fig.6.1b; Table 6.1). Cr concentrations in the aphanitic calcite kimberlites are variable (717 – 3235 ppm), with the opaque-rich calcite kimberlites and the perovskite-rich calcite kimberlite having the lowest (Cr <800 ppm) and highest (Cr = 3235 ppm), respectively (Table 6.2). Sc (19 – 25 ppm) and Co (89 – 112 ppm) concentrations are less variable show the least variability among the macrocrystic varieties and the aphanitic calcite kimberlites (Sc = 22 – 38 ppm; Co = 77 – 112 ppm) (Table 6.2). Generally, except for higher and lower Ni and Cr abundances in samples DDH-002-4 and DDH-008-4, respectively. All kimberlite intrusions in this study generally fall within the field of group I kimberlites (Fig. 6.1).

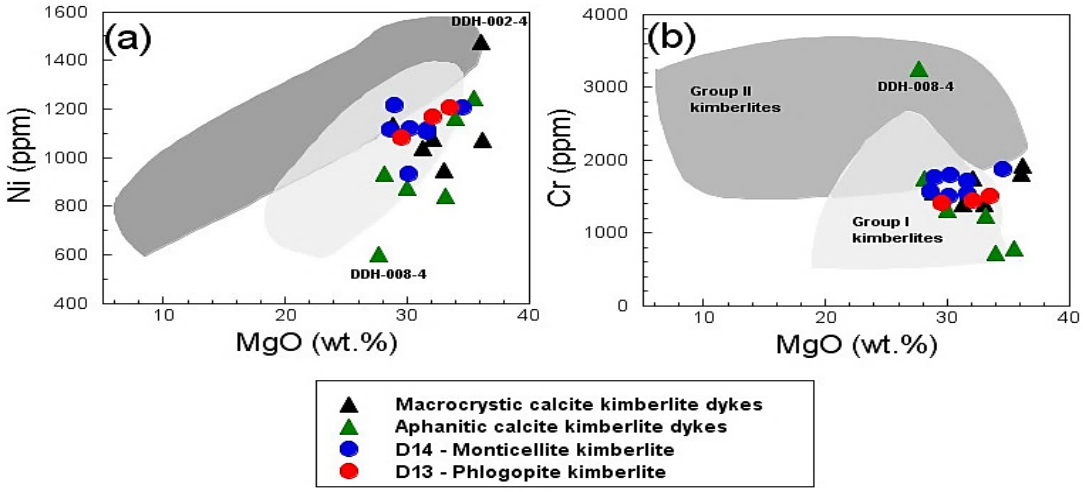

Figure 6.1: Bivariate plots of MgO vs selected compatible elements in samples representative of different kimberlite intrusions from the eastern lobe of the Du Toitspan kimberlite pipe. The group I kimberlites field is from le Roex et al (2003). The group II kimberlites field is from Becker and le Roex (2006).

6.3. INCOMPATIBLE ELEMENTS

Large ion lithophile (LILE) in the D13 – phlogopite kimberlite shows a narrow range (Rb= 105 – 130 ppm; Ba =635 - 707 ppm; Sr = 585 – 811 ppm) (Table 6.1; Fig. 6.2). The D14 -monticellite kimberlite show a broader range in LILE (Rb = 80.2 – 131 ppm; Sr = 718 – 1656 ppm; Ba = 594 – 1888 ppm) (Table 6.1; Fig. 6.2), with samples DDH - 014-4 and DDH-015-5 being richer and poorer lowest in LILE abundances, respectively (Table 6.1). LILE in the macrocrystic calcite kimberlites have lower Rb (44.4 -103 ppm) and similar Sr (618 - 996 ppm) compared to the other macrocrystic kimberlite varieties (Fig. 6.2a; b). Ba concentrations in the macrocrystic calcite kimberlites are generally <800 ppm, although sample DDH-015-5 shows exceptionally higher Ba (~1888 ppm). LILE in the aphanitic calcite kimberlites show a broad range (Sr = 957 - 1446 ppm; Ba = 193 - 124 ppm; Rb 9.33 - 729 ppm), with samples DDH-012-3 and DDH-008-4 having the lowest and highest LILE concentrations, respectively (Table 6.1). Generally, when plotted against each other on bivariate plots, LILE concentrations in the different kimberlite intrusions describe scattered coherent distributions (Fig. 6.2e). Although they generally fall within the overlapping field between group I and II kimberlites (Fig. 6.2). More specifically, some D13 - phlogopite kimberlite samples (DDH-001-3 and DDH-007-3) and D14 – monticellite kimberlite samples (DDH-006-3, DDH-015-5 and DDH-016-4) have Rb abundances that are more comparable to group II kimberlites. Also, some D14 – monticellite kimberlite samples (DDH-015-5 and DDH-016-4), and one macrocrystic calcite kimberlite dyke sample (DDH-014-2) all have Ba concentrations that fall within the field of group II kimberlites.

High Field Strength elements (HFSE) in the D13 – phlogopite kimberlite show a narrow (Nb = 101 – 106 ppm; Ta =5.8 - 6.2 ppm; Th = 9.2 - 9.4 ppm) with slightly variable Zr (187 – 267 ppm) (Table 6.1; Fig 6.3). The D14 - monticellite kimberlites show a broader range in HFSE (Nb =123 – 148ppm; Zr = 221 – 283 ppm; Th = 9.70 – 14.73 ppm). The macrocrystic calcite kimberlites dykes show a similar range in HFSE (Nb = 107 – 162 ppm; Zr = 197 – 295 ppm; Th = 8.82 – 16.1 ppm) as the D14 – monticellite kimberlites. HFSE in the aphanitic calcite kimberlite are more variable (Zr = 185 – 464ppm; Th = 9.70 – 14.7 ppm; Nb = 105 – 237 ppm) compared to the macrocrystic kimberlite varieties. The perovskite-rich calcite has the highest enrichment in HFSE (Nb = 237 ppm; Zr = 464 ppm; Th = 24 ppm) compared with the other aphanitic calcite kimberlites (Nb = 106 – 177 ppm; Zr = 185 – 302 ppm; Th = 10.9 – 20.0 ppm) (Table 6.2; Fig. 6.3). HFSE when plotted against each other on bivariate plots describe excellent positive correlations (Fig. 6.3). HFSE in the different kimberlite intrusions fall within the overlapping field between group I and II kimberlites.

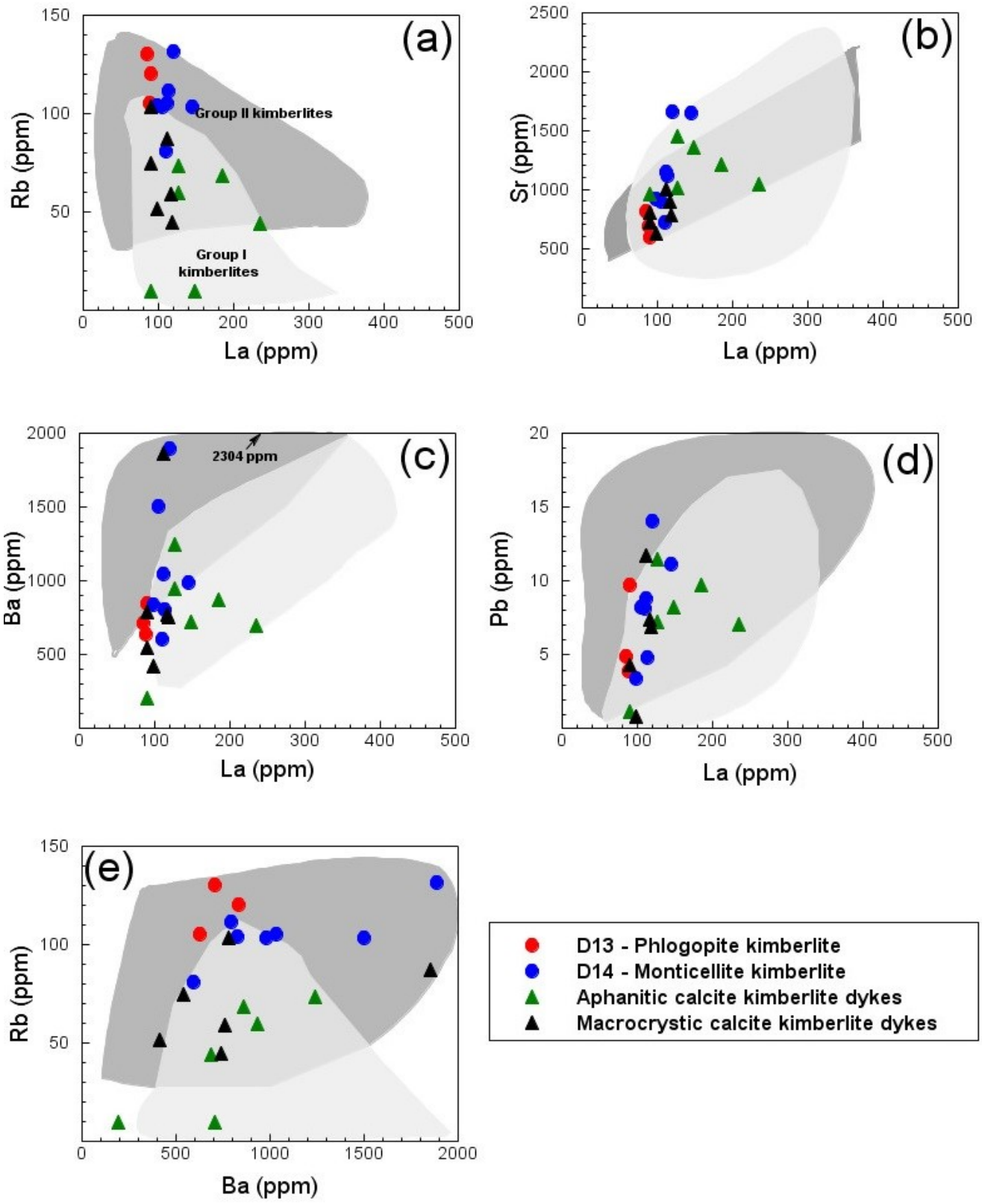

Figure 6.2: Bivariate plots of selected large ion lithophile elements (LILE) in samples representative of kimberlite intrusions from the eastern lobe the Du Toitspan kimberlite pipe. Group I kimberlite field is from le Roex et al (2003). Group II kimberlite field is Becker and le Roex (2006).

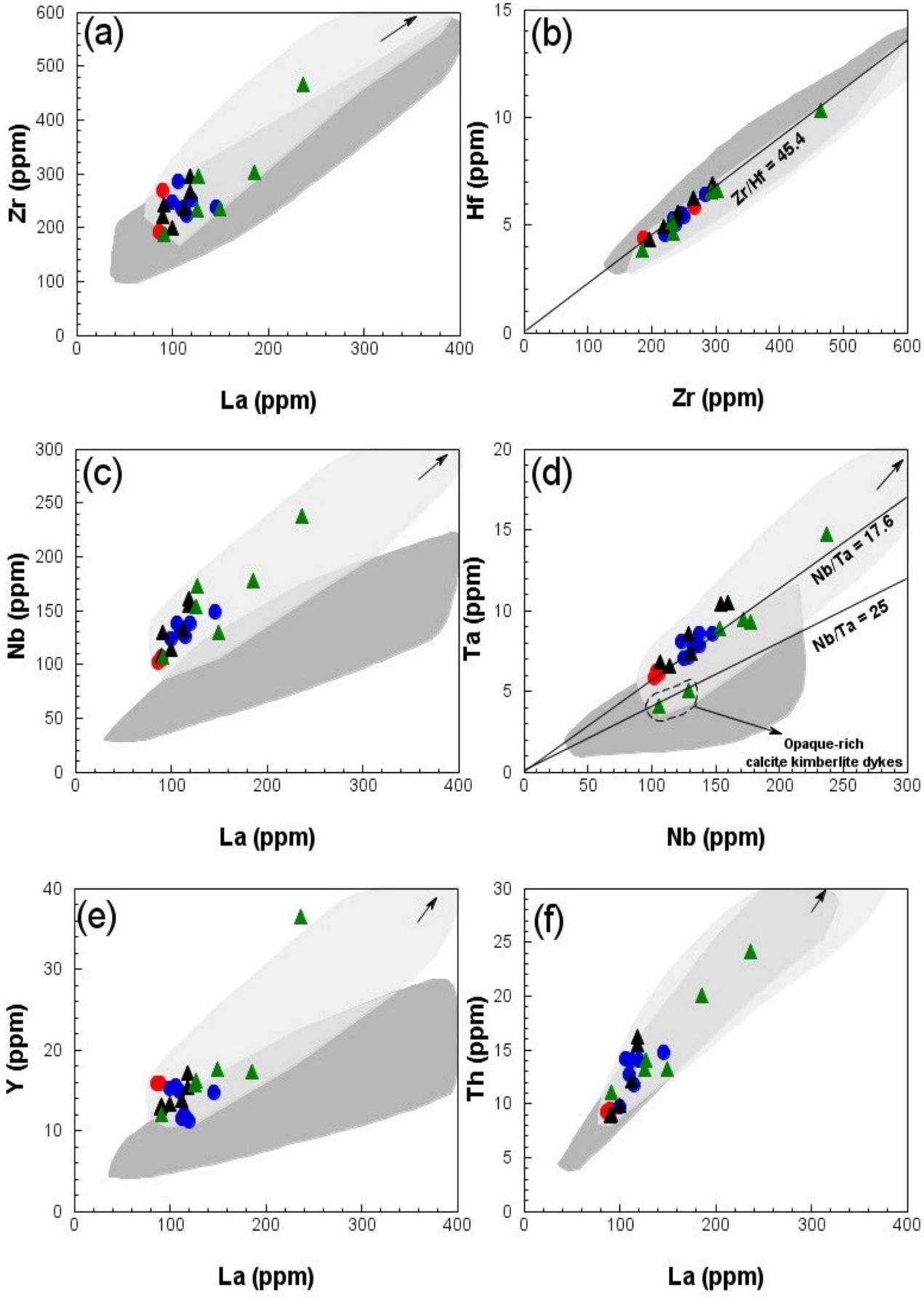
(a)
Zr (ppm)
La (ppm)
(b)
Hf (ppm)
Zr (ppm)
Zr/Hf = 45.4
(c)
Nb (ppm)
La (ppm)
(d)
Ta (ppm)
Nb (ppm)
Nb/Ta = 17.6
Nb/Ta = 25
Opaque-rich
calcite kimberlite dykes
(e)
Y (ppm)
La (ppm)
(f)
Th (ppm)
La (ppm)

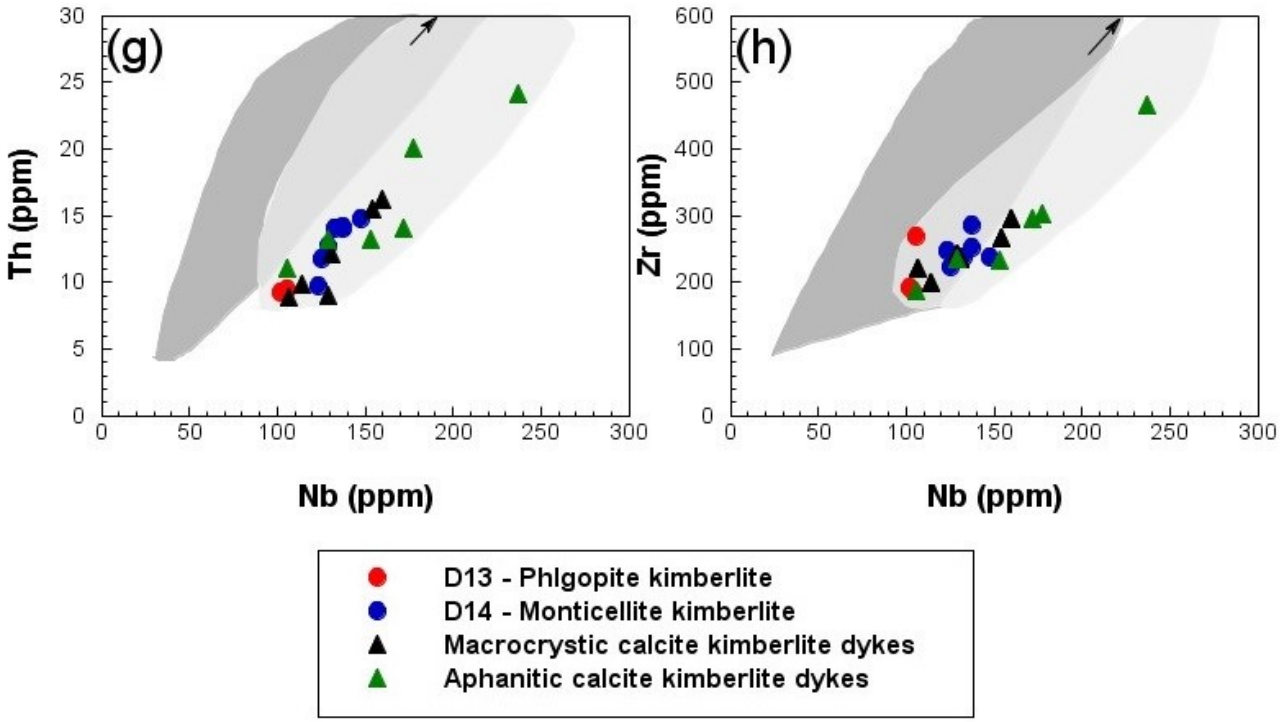

Figure 6.3: Bivariate plots of selected high field strength elements (HFSE) in samples representative kimberlite intrusions from the eastern lobe the Du Toitspan kimberlite pipe. Group I kimberlite field is from le Roex et al (2003). Group II kimberlite field is from Becker and le Roex (2006).

6.4. INCOMPATIBLE ELEMENT RATIOS

Incompatible element ratios in the D13 – phlogopite kimberlite samples show little variation (La/Nb =0.9 ± 0.01; Th/U =3.6 ± 0.09; Nb/Ta = 17.3 ± 0.42; Zr/Hf = 44.4 ± 1.76) (Fig. 6.4; Table 6.3). Although there is some slight variation in their Zr/Sm ratios (~17.0 – 24.7). When normalised to chondrite values (Sun and McDonough, 1989), the D13 – phlogopite kimberlite samples are characterized sub-parallel patterns (La/Sm_N = 5.31 – 5.53; La/Yb_N = 66.9 – 73.7) with a flattening slope towards the heavier REE (Gd/Yb_N = 6.49 – 7.02) (Fig. 6.5). When normalised to the primitive mantle, incompatible elements in the D13 – phlogopite kimberlite show Hf, Sr and Ti negative anomalies (Fig. 6.7). The magnitudes of these anomalies can be quantified by interpolating their values from normalised diagrams if one assumes a smooth variation between two adjacent elements (le Roex, et al., 2003). For example, $Hf^* = [Sm \times Zr]^{1/2}$, where Sm and Zr are both normalised. The magnitudes of calculated anomalies are expressed with the notation (X/X *), where X is the measured concentration of the element and X* is the interpolated value for the same element (le Roex et al., 2003). The magnitudes of negative anomalies in the D13 – phlogopite kimberlite samples show very similar magnitudes (Ti/Ti* = 0.50 ± 0.01; Hf/Hf* = 0.73 ± 0.03; and Sr/Sr* = 0.52 ± 0.07) and are characterised by the absence of K-anomalies (Fig. 6.7a).

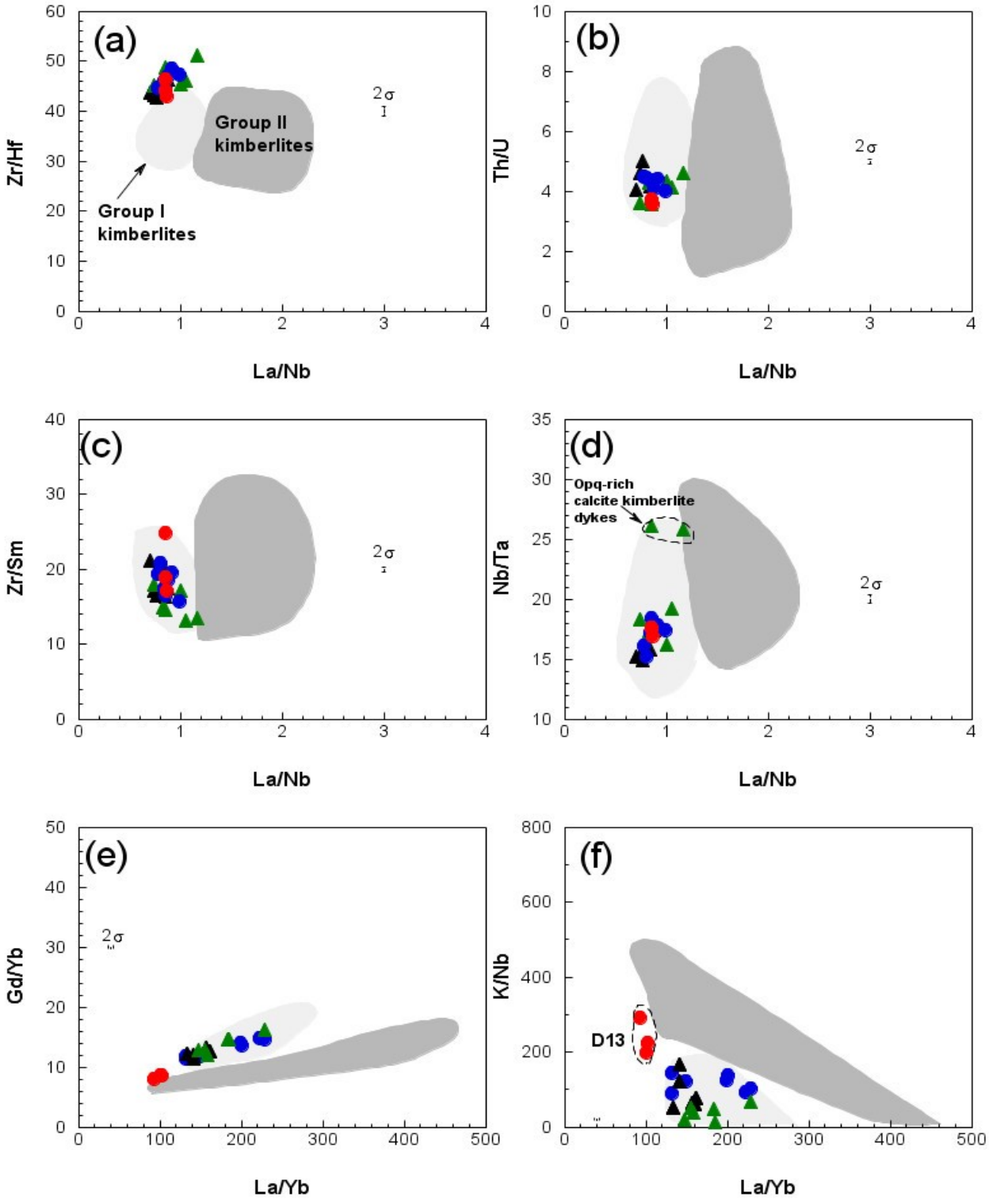

Figure 6.4: Bivariate plots showing selected incompatible trace element ratios in samples representative kimberlite intrusions from the eastern lobe the Du Toitspan kimberlite pipe. Group I kimberlites field is from le Roex et al (2003). Group II kimberlites is from Becker and Le Roex (2006). 2σ error bars have also been shown where applicable.

Because incompatible trace element ratios in the D14 – monticellite kimberlites and macrocrystic calcite kimberlites show broad overlap they are described here together. Incompatible trace element ratios in the D14 – monticellite kimberlites and macrocrystic calcite kimberlites are almost indistinguishable and range from (La/ Nb = 0.80 ± 0.07; Th/U = 4.3 ± 0.4, Nb/Ta = 16.0 ±1.3; Zr/Hf = 44.1 ± 1.3; Ba/Nb = 3.65 – 14.12). Trace element ratios with mobile elements (e.g., Ba/Nb, Ce/Pb) show the most variability. Chondrite normalised values for the D14 - monticellite kimberlites and macrocrystic calcite kimberlites show strong enrichment in LREE (D14 – monticellite kimberlites: La/Sm_N = 4.66 – 6.51; macrocrystic calcite kimberlites: La/Sm_N = 4.39 – 5.68). Both the macrocrystic calcite kimberlites (La/Yb_N = 96.1 – 115; Gd/Yb_N = 9.32 – 10.8), and the D14 – monticellite kimberlites (La/Yb_N = 143 – 164; Gd/Yb_N = 11.5 – 12.2) are characterized by sub-parallel, steep-straight patterns. Super imposed on the steep-straight patterns of the D14 - monticellite kimberlites and the dykes are negative K, Hf, Sr and Ti anomalies (Fig. 6.7 - 8). Negative anomalies in the macrocrystic calcite kimberlite range from (K/K* = 0.29 ± 0.14 Ti/Ti* = 0.54 ± 0.09; Hf/Hf* = 0.67 ± 0.04; and Sr/Sr* = 0.48 ± 0.06) and from (K/K* = 0.37 ± 0.08 Ti/Ti* = 0.46 ± 0.09; Hf/Hf* = 0.69 ± 0.04; and Sr/Sr* = 0.66 ± 0.15) in the D14 – monticellite kimberlites.

The aphanitic calcite kimberlites have variable incompatible trace element ratios (La/ Nb = 0.80 ± 0.07; Th/U = 4.3 ± 0.4, Nb/Ta = 16.0 ±1.3; Zr/Hf = 44.1 ± 1.3; Ba/Nb = 3.65 – 14.12).The perovskite-rich dyke (DDH-008-4) and the phlogopite-rich (DDH-013-2) to a lesser extent show the most enrichment in REE abundances compared to the other aphanitic and macrocrystic kimberlite varieties (Fig. 6.6b; Table 6.2). The opaque rich calcite kimberlite are characterized by the least REE compared to the other aphanitic calcite kimberlite dykes. Although except for the phlogopite- rich calcite kimberlite (La/Sm_N = 164), REE patterns (La/Yb_N = 105 – 131) among the other aphanitic kimberlite varieties are sub-parallel and are characterised by a steeper slope compared to the macrocrystic kimberlite varieties. When normalised to primitive mantle normalised diagrams, the aphanitic calcite kimberlites are also characterised by Sr, Hf, Ti , K negative anomalies with widely variable magnitudes (K/K* = 0.04 – 0.20; Ti/Ti* = 0.20 - 0.55; Hf/Hf* = 0.52 – 0.68; and Sr/Sr* = 0.56 – 0.75), with the opaque – rich calcite kimberlites showing greater magnitudes in Ti and K- negative anomalies compared to the other aphanitic kimberlites varieties with more subdued anomalies (Fig. 6.8b). The opaque-rich calcite kimberlite also show Rb-Ba anomalies, although it is clear if these are an inherent feature or consequence of element mobility.

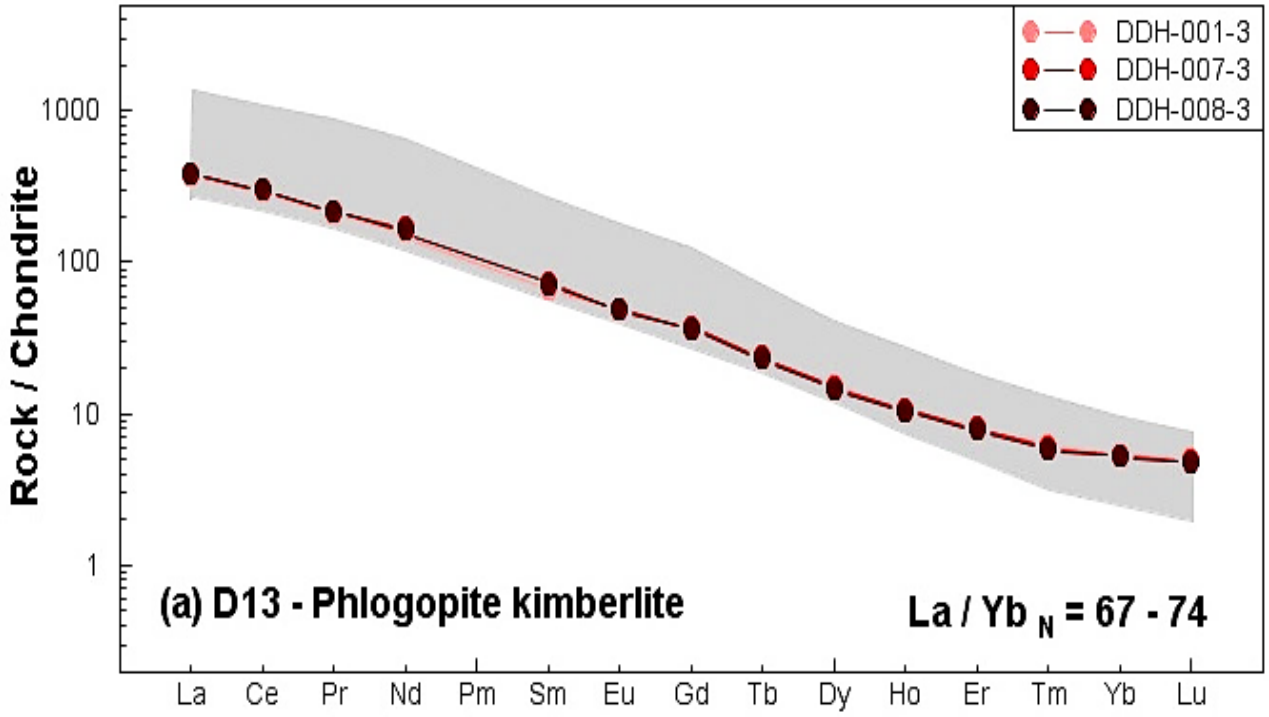

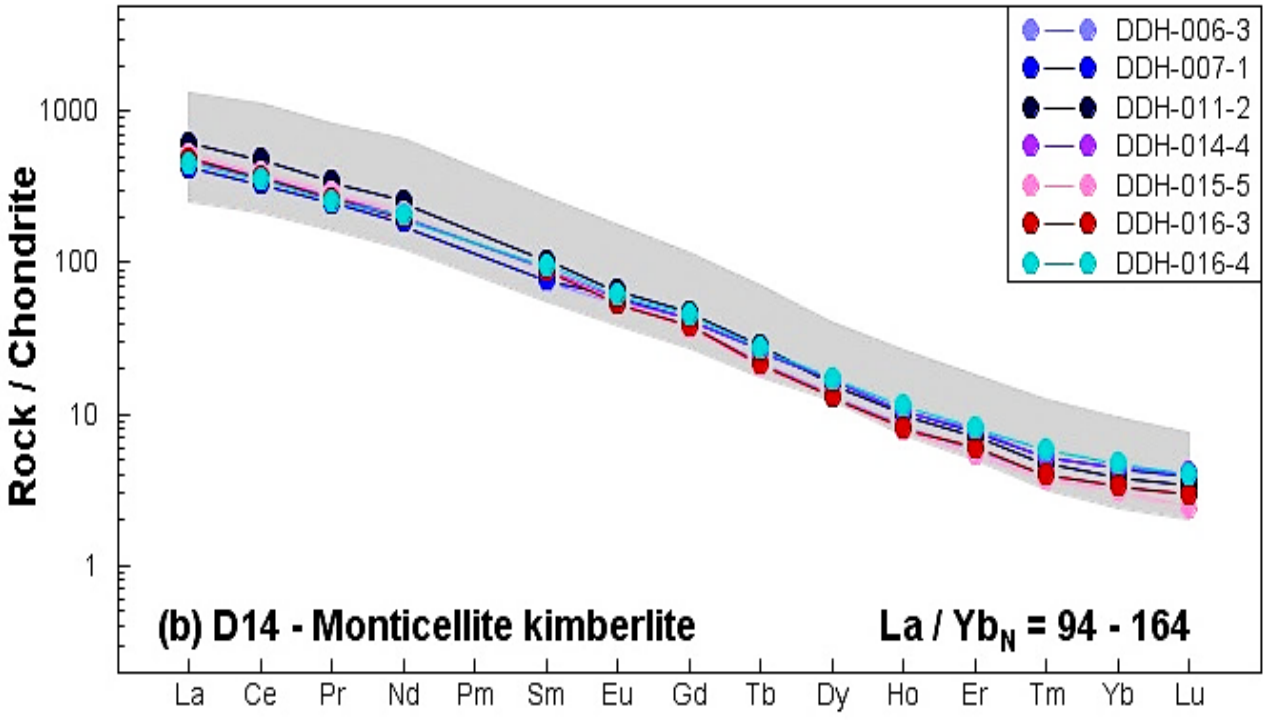

Figure 6.5: Chondrite normalised diagrams of REE patterns in the major kimberlite intrusions. Normalising values from Sun and McDonough (1989). Field of group I kimberlites from le Roex et al. (2003).

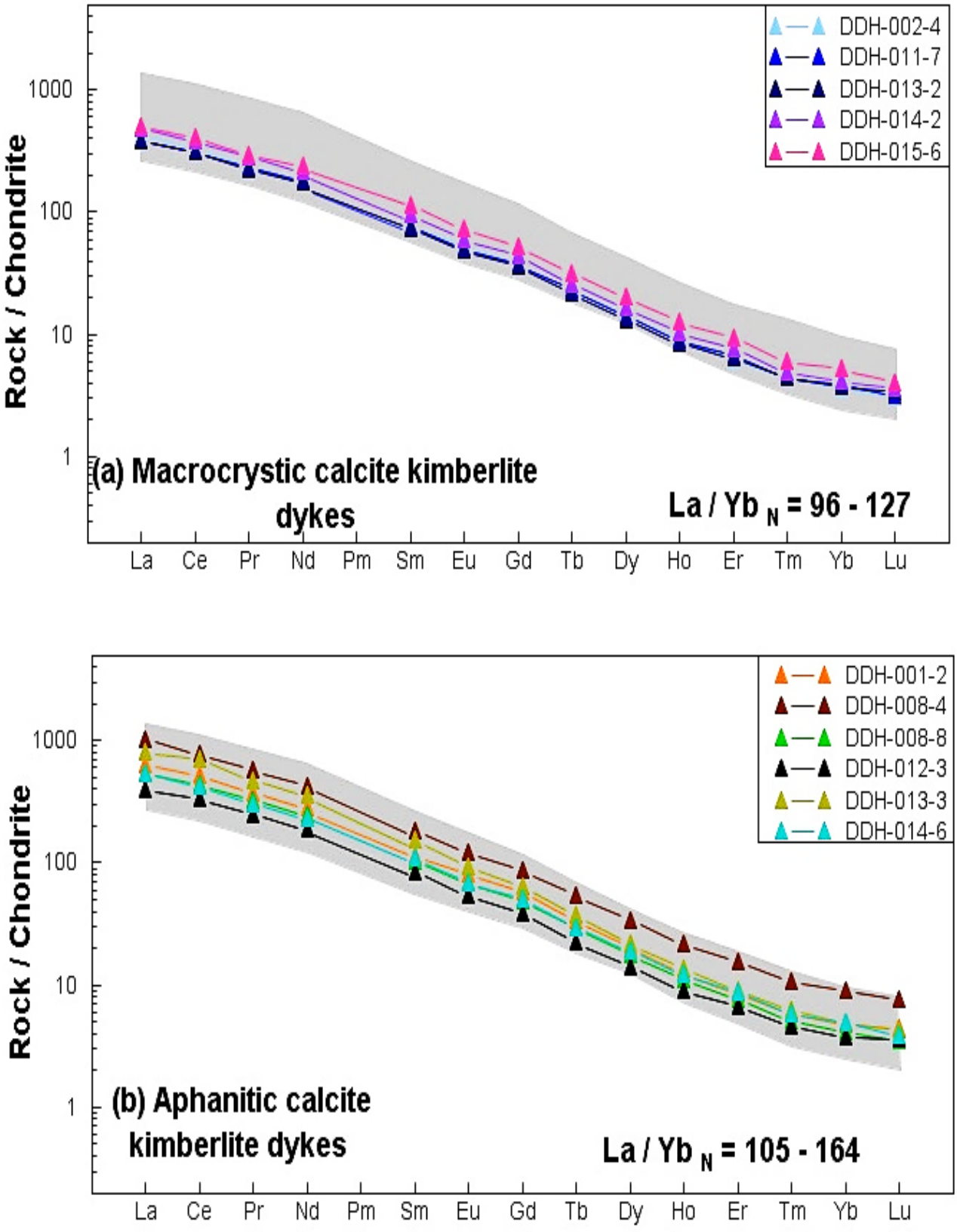

Figure 6.6: Chondrite normalised diagrams of REE patterns in the dykes. Normalising values from Sun and McDonough (1989). Field of group I kimberlites from le Roex et al. (2003).

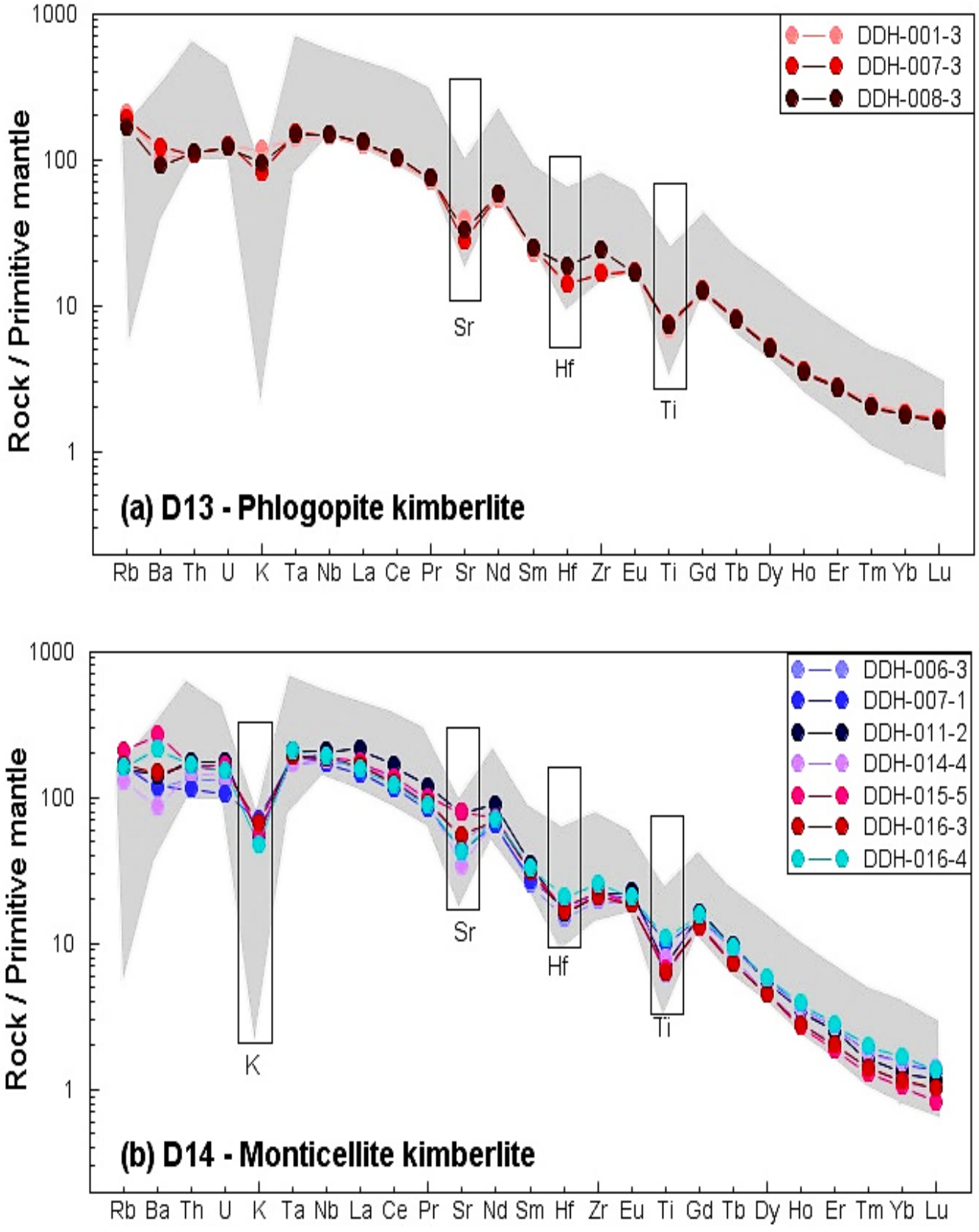

Figure 6.7: Primitive mantle normalised diagrams of incompatible element patterns in the major kimberlite intrusions phases. Normalising values from Sun and McDonough (1989). Group I kimberlite filed from le Roex et al (2003).

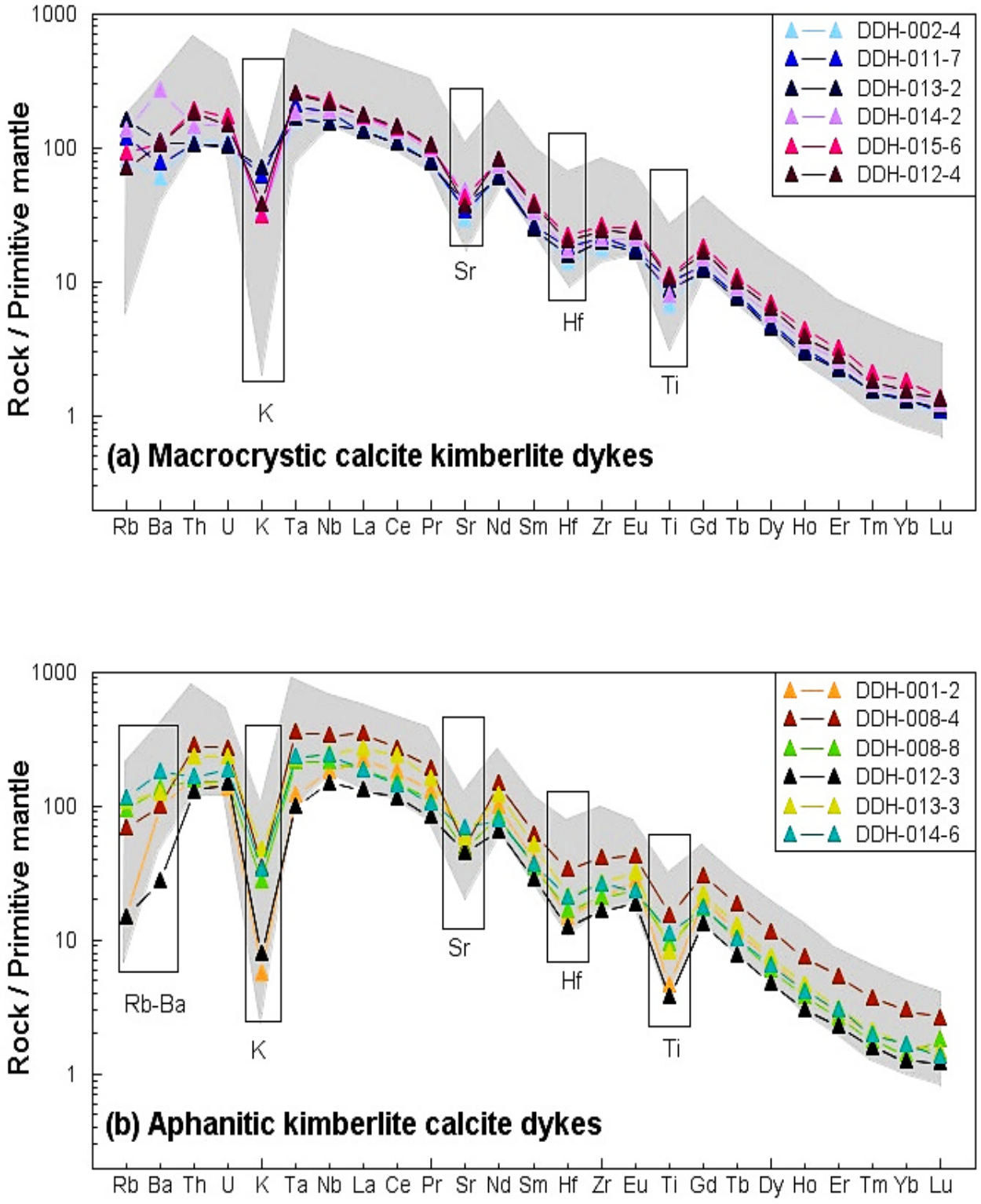

Figure 6.8: Primitive mantle normalised diagrams of incompatible element patterns in the dykes. Normalising values from Sun and McDonough (1989). Group I kimberlite field from le Roex et al. (2003).

CHAPTER 7: PETROGENESIS

7.1. INTRODUCTION

Kimberlite magmas are enriched in incompatible elements (Mitchell, 1986; Smith et al., 1985; Woolley et al., 1996; Becker and le Roex, 2006; Fraser et al., 1985). Their enrichment in incompatible elements has been widely ascribed to low degrees of partial melting of an enriched source relative to the primitive mantle (Mitchell, 1986). This is consistent with experimental studies conducted on CaO-MgO-Al_2O_3-SiO_2-CO_2 ($CMAS$-CO_2) component systems demonstrating that kimberlitic magmas can be produced by low degrees of partial melting of a carbonated peridotite at pressures <10 GPa (Wyllie,1978; Eggler and Wendlandt, 1979; Canil and Scarfe,1990; Dalton and Presnall, 1998; Ulmer Sweeney, 2002; Gudfinnsson and Presnall, 2005). Accordingly, several kimberlite petrogenetic models have proposed that kimberlites are low degree partial melts derived from an enriched source argued to be located within the sub-continental lithospheric mantle (SCLM) (e.g., le Roex et al., 2003; Becker and le Roex, 2006; Arndt et al., 2010; Howarth and Taylor; 2016; Howarth and Büttner, 2019; Chalapathi, 2017). Although while these models vary with respect to the nature of the metasomatising agents directly preceding kimberlite petrogenesis, they are in general agreement that the metasomatising fluids/melts originate from a sub-lithospheric source. Alternatively, some authors advocate for the 'hybridization model' which considers kimberlites to be carbonate-rich 'proto-kimberlite magmas' derived from the asthenosphere, becoming modified towards more silicic compositions from the assimilation of the lithospheric mantle *en-route* to surface (e.g., Patterson et al., 2009; Russel et al., 2013; Shatskiy et al., 2017; Golovin et al., 2018; Abersteiner et al., 2019; Kamenetsky et al., 2008; 2014). In the study of kimberlite petrogenesis two rather different geochemical approaches have been adopted. One involves detailed chemical analysis of their constituent olivines and its hosted mineral and melt inclusions (see reviews by Giuliani, 2018; Bussweiler, 2019). Another approach, which is adopted in this study, involves the analysis of their bulk-rock geochemistry.

Earlier geochemical studies conducted on kimberlites were largely qualitative and descriptive (e.g. Wedepohl and Muramatsu, 1979; Clement, 1982; Muramatsu, 1983; Shee, 1985). It is only in more recent studies where trace elements in kimberlite have been treated quantitatively in attempts to model their petrogenesis (e.g., Fraser and Hawkesworth, 1992; Tainton and McKenzie, 1994; Beard et al., 1998; le Roex et al., 2003; Chalapathi et al., 2004; Harris et al., 2005; Becker and le Roex, 2006; Coe et al., 2008; Chalapathi and Dongre, 2016; Chalapathi, 2017; Dongre and Tappe, 2019). In the present study, semi-quantitative models predicting the distribution of trace elements in the various kimberlite intrusions in this study are used to

characterise their source region (s) and to place constraints on their petrogenesis. Kimberlite intrusions investigated include; the D13 – phlogopite kimberlite, the D14 – monticellite kimberlite, and associated macrocrystic and aphanitic calcite kimberlite dykes that range in texture from macrocrystic to aphanitic in texture.

Although before the petrogenesis of the various kimberlite intrusions can be evaluated, it is important to first consider the influence of syn- and post-emplacement compositional modification processes such as low temperature alteration, fractionation and mantle entrainment (and assimilation) on the compositions of the various kimberlite intrusions in this study.

7.2. ROLE OF LOW TEMPERATURE ALTERATION

Serpentinization is by far the most dominant low temperature alteration process affecting kimberlites (Stripp, et al., 2006; Afanasyev et al., 2014). Serpentine occurs as either deuteric or cryptocrystalline serpentine. As deuteric serpentine, it forms as pseudomorphs of relict olivine macrocrysts and phenocrysts or along their grain boundaries (Mitchell, 1986). As cryptocrystalline serpentine, it crystallizes with carbonate (calcite ± dolomite) in 'residual pools' in low temperature environments often replacing earlier formed groundmass minerals (Mitchell, 1986). Since samples in this study have certainly experienced varying degrees of alteration as evidenced by the presence of secondary serpentine (Chapter 3), the possibility that their incompatible elements could have been perturbed during this process needs to be evaluated. Smooth trends in a co-genetic suite of rocks plotted on bivariate diagrams is usually a good indicator of some petrogenetic process at work (Cox et al., 1979). Because incompatible elements are especially sensitive to partial melting, the distribution of incompatible from the different samples is expected to be controlled by this process which is readily visible by a positive slope on bivariate plots. Thus, the effects of low temperature alteration can recognised by contrasting behaviours of their fluid – mobile elements (alkaline earth, alkali metals and actinoids) and immobile elements, where deviation from a positive slope serves as an indication of compositional modification by either low temperature or post emplacement alteration (le Roex et al., 2003).

In evaluating the effects of alteration, it is clear that immobile elements in all samples show strong positive correlation (Fig. 6.3; Fig. 7.1a). In contrast when mobile elements are plotted against an immobile element, or another mobile element, they generally describe incoherent scattered distributions (Fig. 7.1b - d). This is especially apparent in samples with prominent segregationary textures (e.g., DDH-014-2 and DDH-015-5; Fig.7.1b; c). In general, there is strong evidence to suggest that mobile elements in this suite of rocks samples have been disturbed by

low temperature and post-emplacement alteration, while in contrast their immobile elements have remained resilient and largely unaffected by these processes.

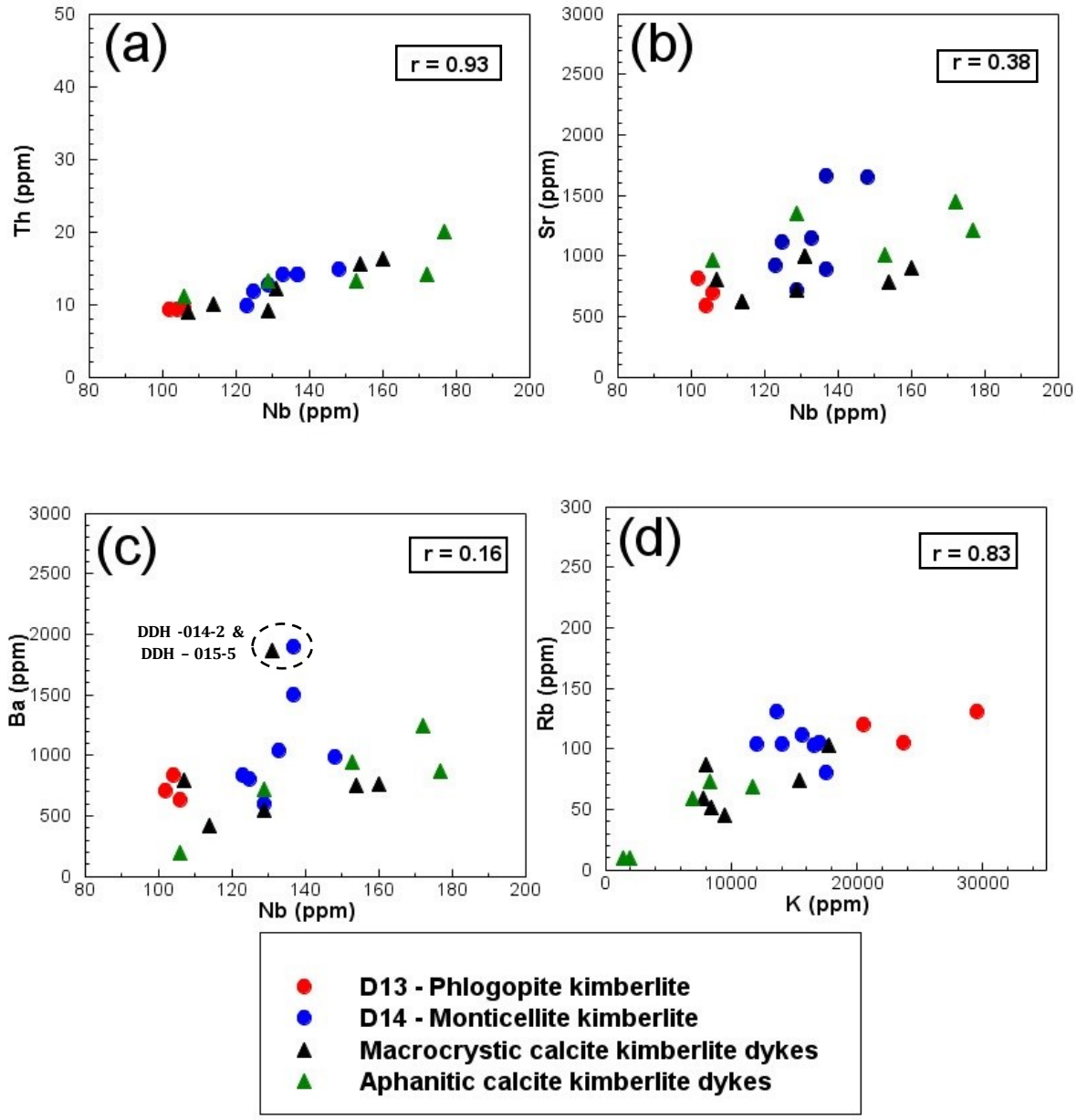

Figure 7.1: Bivariate plots showing selected mobile vs immobile elements illustrating effects low temperature alteration in samples representative of kimberlite intrusions from the eastern lobe of the Du Toitspan kimberlite pipe. Correlation coefficients (r) also shown.

7.3. ROLE OF FRACTIONATION

Primary kimberlite magmas typically experience differentiation by crystal fractionation *en-route* to surface (Mitchell, 1986). Although primary compositions for kimberlite magmas are

not well constrained, with proposed compositions ranging from silicate (e.g., Price et al., 2000; le Roex, et al., 2003; Becker and le Roex, 2006; Kopylova, et al., 2007, 2013; Kjarsgaard et al., 2009), to transitional silicate-carbonate (Nielsen and Sand, 2008; Brooker et al., 2011; Howarth and Taylor, 2016; Howarth and Büttner, 2019) and carbonate (Francis and Patterson, 2009; Russel et al., 2013; Kamenetsky et al., 2008, 2014; Pilbeam et al., 2013; Brett et al., 2015;Stone and Luth, 2016; Shatskiy et al., 2017; Golovin et al., 2018; Abersteiner et al., 2019). This disparity complicates attempts to understand compositional modification by crystal fractionation in co-genetic kimberlite intrusions because there is no common reference point. Nevertheless, in this section an attempt is made to determine whether kimberlite intrusions in this suite can be related by crystal fractionation.

Evaluation of the macrocrystic kimberlite varieties for crystal fractionation is however not possible given that the latter are better considered as partial cumulates rather than liquids (e.g., Mitchell, 1986; le Roex et al., 2003), and on account of their macrocrystic textures are anyway unlikely to have experienced significant differentiation by crystal fractionation (Mitchell, 1986). Because aphanitic kimberlites represent the closest analogues to 'true kimberlite liquids' (e.g., Price et al., 2000; le Roex et al., 2003; Becker and le Roex, 2006) this section will only focus on the aphanitic kimberlite varieties in this study. The aphanitic calcite kimberlites have been sub-divided into; (2) opaque-rich calcite kimberlites, (2) serpentine calcite kimberlites, (1) phlogopite-rich kimberlite, and (1) perovskite-rich calcite kimberlite. Since olivine is the dominant (micro)-phenocryst in the aphanitic calcite kimberlites (Table 2.1); any magmatic differentiation experienced is expected to have been controlled largely by olivine fractionation. A major consequence of olivine fractionation is to deplete the host kimberlite magma in the mineral forming major elements such as MgO, SiO_2, FeO and their compatible elements, while also enriching the host kimberlite magma in other major elements such as CaO, TiO_2, P_2O_5 and incompatible elements (Zr, Nb, Th, LREE). Trace element ratios between incompatible elements pairs with similar chemical properties (i.e., ionic charge and radius) are not fractionated from each other during partial melting or significantly so during crystal fractionation (Cox et al., 1979; Wilson, 1989). This makes incompatible trace element ratios a very useful tool in relating various kimberlite intrusions to a common source, before attempting to relate them to a common parental magma. Because the aphanitic opaque-rich calcite kimberlites have more refractory compositions (Ni >1000 ppm; Mg numbers ~0.89) and the least enrichment in incompatible elements compared to other the aphanitic calcite kimberlites, these geochemical characteristics suggest that they experienced the least differentiation by olivine fractionation and hence represent the most primitive compositions among this suite of aphanitic dykes. However, as mentioned above, the aphanitic opaque-rich calcite kimberlites can only be parental to the other aphanitic calcite kimberlites in this study provided that their incompatible

elements ratios are similar. Accordingly, while all other incompatible element ratios in the aphanitic calcite kimberlites are almost indistinguishable, the aphanitic opaque – rich calcite kimberlite is characterised by higher (>25) Nb/Ta ratios compared to those in the aphanitic calcite kimberlites (Nb/Ta ratios <18; Fig 6.4). Because this difference is statistically significant (i.e. falls outside 2-sigma analytical error ; Fig. 6.4). Although the existence of aphanitic dykes from the Du Toitspan kimberlite pipe with similar refractory compositions coupled with distinctly higher Nb/Ta ratios appears to be common (e.g., sample K6/10; le Roex et al., 2003) the opaque-rich calcite kimberlite cannot be parental to the other aphanitic kimberlite varieties in this study.

Following exclusion of the aphanitic opaque-rich calcite kimberlite from consideration, it becomes less apparent which other aphanitic calcite kimberlite variety could represent a potential parental magma. This is because while the precursor dykes (i.e., the aphanitic serpentine calcite kimberlite dykes) are more magnesian (MgO = 30 – 33 wt. %) and least enrichment in incompatible elements compared to the other aphanitic calcite kimberlites in this study, their lower Ni (841-871 ppm) concentrations compared to the aphanitic phlogopite-rich calcite kimberlite (Ni = 937 ppm); suggests that these dykes cannot be related by olivine fractionation. Further, the aphanitic phlogopite – rich calcite kimberlite and the aphanitic perovskite – rich calcite kimberlite despite differences in their compatible and incompatible elements show similarities in their MgO contents also suggests these dykes cannot be related by olivine fractionation either. The aphanitic serpentine calcite kimberlite and the aphanitic perovskite – rich calcite kimberlite are the only aphanitic dykes that could be related to each other by olivine fractionation. Given that some olivines show chemical zonation and others do not, both equilibrium crystallization and fractional crystallization mechanisms are considered.

During equilibrium crystallization, crystals precipitating from the magma remain in equilibrium with the residual melt until they are expelled from the system (Cox et al., 1979). During fractional crystallization only the surface of the crystallizing mineral re-equilibrates with the residual melt, before being isolated from the magmatic system (Cox et al., 1979). Equilibrium olivine crystallization curves are calculated from eqns. 1 and 2 in Figure 7.2 below assume an olivine-melt partitioning of K_D=0.36 (Hertzberg and O'Hara, 2002). Partition coefficients for incompatible elements are from the compilation of Späth et al. (2001). Ni partition coefficients are calculated from the D_{Ni}=124/MgO+0.9 equation of Hart and Davies (1978). The results of the modelling are illustrated in Figures 7.2. The mathematical expressions used to model equilibrium crystallization and fractional crystallization (Shaw, 1970; Rayleigh, 1902) are illustrated below.

$$\frac{C_l}{C_O} = \frac{1}{(D+F-FD)} \quad (1)$$

$$\frac{C_l}{C_O} = F^{(D-1)} \quad (2)$$

C_o = Concentration of a trace element in the original liquid.

C_l = Concentration of trace element in the melt.

F = Degree of melt fraction remaining.

D = Initial bulk distribution coefficient.

Table 7.1: Incompatible elements used Partition coefficients used in quantitative modelling. Compilation from Späth et al. (2001)

Phase	Rb	Ba	Th	K	Ta	Nb	La	Ce	Pb	Pr	Sr	P	Nd
Oliv	0.001	0.001	0.001	0.001	0.001	0.001	0.001	0.001	0.001	0.001	0.001	0.001	0.001
Opx	0.001	0.001	0.001	0.001	0.001	0.001	0.001	0.001	0.001	0.001	0.001	0.001	0.001
Cpx	0.001	0.001	0.001	0.01	0.01	0.01	0.05	0.08	0.08	0.1	0.12	0.1	0.14
Gt	0.001	0.001	0.001	0.001	0.001	0.001	0.01	0.021	0.021	0.054	0.001	0.05	0.087

Phase	Zr	Sm	Eu	Ti	Gd	Tb	Dy	Ho	Er	Tm	Yb	Lu
Oliv	0.001	0.001	0.001	0.001	0.001	0.001	0.001	0.001	0.001	0.001	0.001	0.001
Opx	0.01	0.001	0.01	0.1	0.016	0.019	0.022	0.022	0.03	0.03	0.1	0.1
Cpx	0.2	0.14	0.15	0.17	0.2	0.25	0.3	0.3	0.28	0.29	0.3	0.3
Gt	0.1	0.13	0.2	0.1	0.3	0.6	0.9	1.4	2	3	4	6

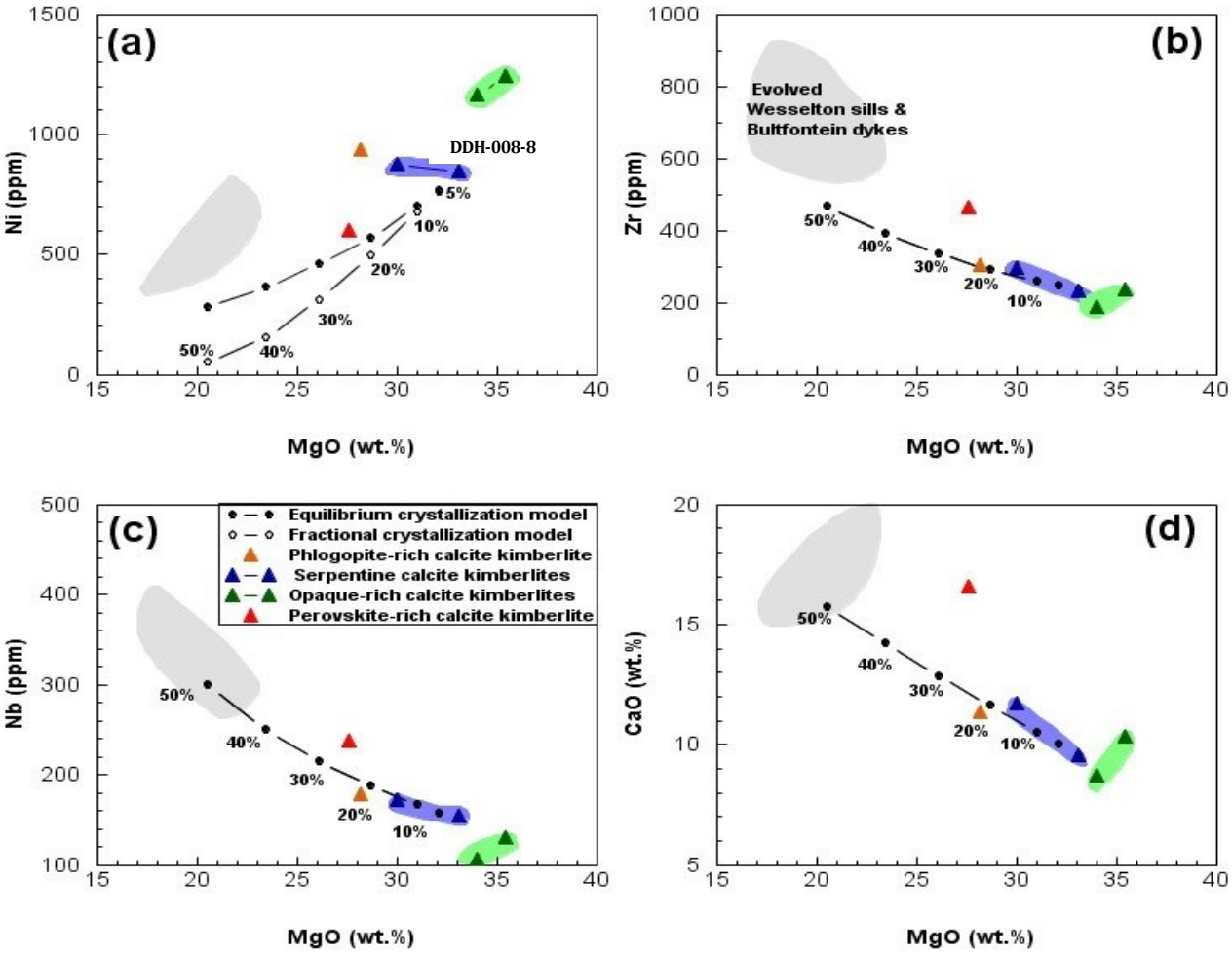

Figure 7.2: Olivine fractional crystallization models relating the aphanitic kimberlites using MgO as a differentiation index. (a) Ni vs MgO. (b - d) Selected incompatible elements vs MgO. Equilibrium crystallization curve (closed circles) and fractional crystallization curve (open circles) calculated using $K_D^{Fe-Mg} = 0.36$ (Hertzberg and O'Hara, 2002) and $D_{Ni} = 124/MgO + 0.9$ (Hart and Davies, 1978). (e) CaO vs MgO. Partition coefficients from Späth et al. (2001). The fields of evolved aphanitic kimberlites from the Wesselton sills and aphanitic kimberlites from the Bultfontein pipes is from le Roex et al. (2003).

Ni concentrations in the aphanitic perovskite – rich calcite kimberlite can be produced by ~20 - 30 % olivine crystallization (Fig. 7.2a). Figure 7.2a demonstrates that the observed variations are more consistent with equilibrium crystallization rather than fractional crystallization. Considering that that some olivines in the perovskite - rich calcite kimberlite are chemically zoned and yet its Ni depletion is inconsistent with fractional crystallization, this is an indication that perhaps a more elaborate fractionation mechanism being at work (e.g., the digestive fractional crystallization model; Pilbeam et al., 2013). Although not shown, results from olivine fractionation modelling indicate that the enriched REE abundances in the aphanitic perovskite-rich calcite kimberlite could be accounted for by ~50% olivine fractionation from the aphanitic serpentine calcite kimberlites. This is of cause inconsistent with enrichment of other incompatible elements (Zr, Nb) and CaO contents (Fig. 7.2b – d).

7.4. ROLE OF MANTLE ENTRAINMENT

Kimberlite magmas entrain disaggregated xenoliths from the upper mantle *en-route* to surface, a process widely considered to be responsible for their macrocrystic textures (Dawson, 1981, Mitchell, 1986). The assimilation of entrained mantle xenoliths in kimberlites is expected to enrich the host magma in MgO, SiO_2, FeO, Al_2O_3 and compatible elements (Ni, Cr) while decreasing incompatible elements (K and REE). To correct for the effects of mantle entrainment, the approach taken is similar to that of Berg (1998), and uses a combination of the lever rule as defined by Cox et al. (1979) to estimate the degree of mantle entrainment, and mass balance to correct for the effects mantle entrainment.

Degree of mantle entrainment

To determine the degree of mantle entrainment experienced by the macrocrystic kimberlite varieties in this study, their respective averages from their representative samples are taken to represent their hybrid magma (C_{hm}) compositions. These compostions for the D13 – phlogopite kimberlite, D14 – monticellite kimberlite and the macrocrystic calcite kimberlites all define a mixing trajectory on a plot of Sc-SiO_2 between proposed close-to-primary compositions (C_{pm}) for kimberlites from the Kimberley cluster (approximated from sample K119/2; le Roex, et al., 2003) and typical peridotite (C_1) from the upper mantle in the region (approximated from sample BD2426; Grégoire et al., 2002). Using the lever rule the average degree of mantle entrainment experienced by the D13 – phlogopite kimberlite, the D14 – monticellite kimberlite and the macrocrystic calcite kimberlites is determined to have been ~37%, ~27% and ~20%, respectively. This is consistent with their olivine modal abundances (Table 3.1).

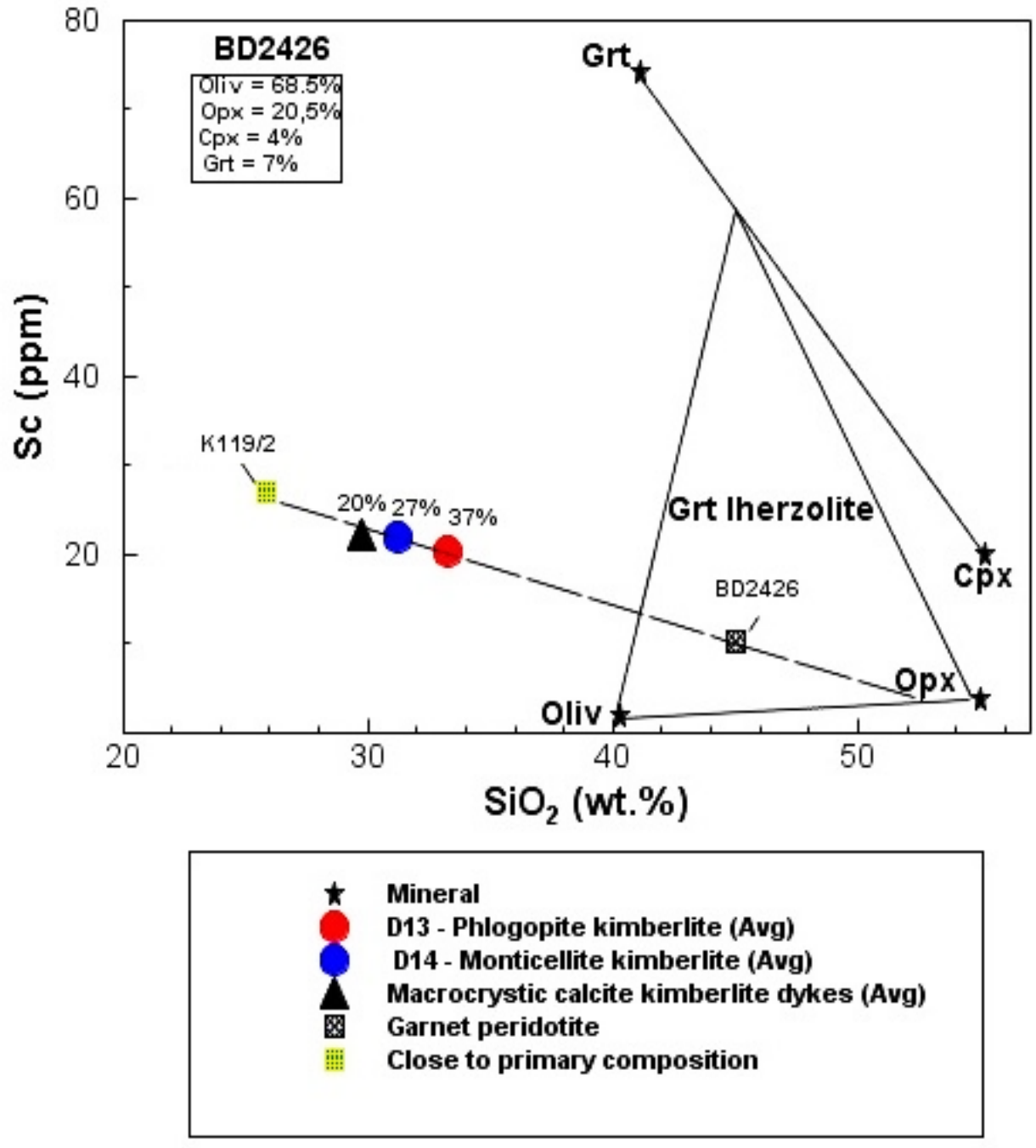

Figure 7.3: Sc vs SiO_2 illustrating the effects of mantle entrainment (and assimilation) macrocrystic kimberlite varieties from the eastern lobe of the Du Toitspan kimberlite pipe. Dashed line shows a mixing trajectory between close-to-primary composition [sample K119/2, le Roex et al. (2003)] and Peridotite [sample BD2426; Grégoire et al. (2002)]. Representative mineral compositions are from Grégoire et al. (2002). The degree of mantle entrainment estimated using the lever rule (Cox et al., 1979).

The effect of mantle entrainment

The main intrusive bodies (D13 – phlogopite kimberlite and the D14 – monticellite kimberlite) are primarily distinguished by distinct REE patterns and K_2O (and Al_2O_3) variations. In order to evaluate the petrogenetic significance of these variations to make it possible to relate ther absolute abundances those in the aphanitic calcite kimberlite dykes, REE and K abundances in the various macrocrystic kimberlite varieties are corrected the determined degree of mantle entrainment. Myers et al. (1987) showed that by simple rearrangement of traditional mass balance relations it is possible to account for the hybridization of two components in magmatic systems. The two-component mixing mass balance equation of Myers et al. (1987) is expressed as follows:

$$\mathbf{C_{pm} = \frac{C_{hm}}{X} + (1 - \frac{1}{X})C_1} \quad \textbf{(3)}$$

C_{pm} = primary magma
C_{hm} = hybrid magma
X = the proportion of parental magma
C_1 = component 1 (peridotite).

Using equation 3, hybrid REE and K magma compositions (C_{hm}) in the various macrocrystic kimberlite varieties are corrected using the inverse of their determined amounts of mantle entrainment (i.e., the proportion of parental magma). A typical smooth REE pattern representative of typical peridotite (C_1) is approximated using sample BD2421 (Grégoire et al., 2002) and applied in equation 3. The corrected REE and K are presented in Table 7.2 where they are compared with those in the respective aphanitic calcite kimberlite varieties in this study. The effects of mantle entrainment on REE abundances of the various macrocrystic kimberlite varieties is illustrated in Figures 7.4a to 7.4c. These are compared with REE abundances in the aphanitic (Figure 7.4d).

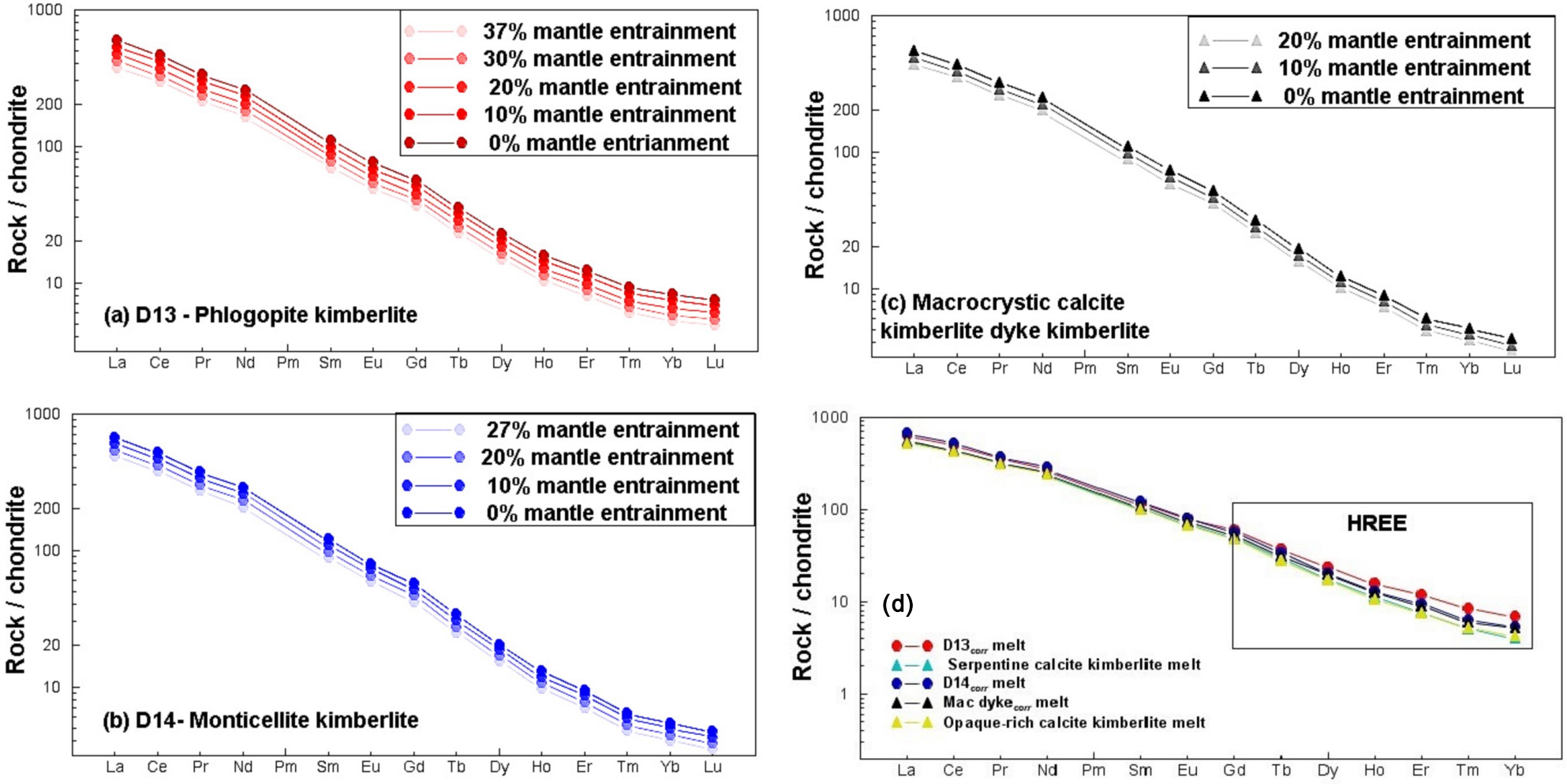

Figure 7.4: Mantle entrinement corrected REE patterns. (a – c) Chondrite normalised REE of macrocrystic parental magmas after correcting for mantle entrainment. (d) Calculated REE abundances in the macrocrystic kimberlite varieties compared with measured REE abundances in the aphanitic kimberlite varieties. Chondrite normalising values from Sun and McDonough (1989).

Table 7.2: Primitive mantle normalized average parental magma REE and K compositions in the different kimberlite intrusions from the eastern lobe of the Du Toitspan kimberlite pipe

	K-enriched intrusive phase		K-depleted intrusive phase						
	Avg. D13 - phlogopite kimberlite		Avg. D14 - monticellite kimberlite		Avg. Macrocrystic calcite kimberlites		Avg. opaque-rich calcite kimberlite	Avg. serpentine calcite kimberlite	Avg. phlogopite-rich calcite kimberlite
	Chm	Cpm	Chm	Cpm	Chm	Cpm			
†K	98.4	155	61.6	83.8	47.1	58.6	19.4	30.4	46.8
La	88.8	140	115	156	104	129	121	127	186
Ce	180	282	232	316	216	268	259	261	419
Pr	20.1	31.6	25.9	35.2	24.5	30.4	29.4	29.4	44.7
Nd	76.1	120	97	132	93	116	110	111	164
Sm	10.6	16.6	13.5	18.3	13.5	16.7	15.1	16	23.1
Eu	2.81	4.37	3.4	4.6	3.39	4.2	3.88	3.94	5.4
Gd	7.44	11.5	8.7	11.7	8.60	10.7	9.84	10.2	13.2
Tb	0.866	1.33	0.94	1.26	0.950	1.17	1.05	1.1	1.37
Dy	3.79	5.75	3.89	5.17	4.02	4.92	4.3	4.61	5.45
Ho	0.585	0.888	0.551	0.73	0.570	0.7	0.598	0.648	0.757
Er	1.32	2.02	1.17	1.55	1.20	1.46	1.23	1.36	1.48
Tm	0.152	0.234	0.123	0.163	0.125	0.153	0.132	0.138	0.155
Yb	0.9	1.39	0.683	0.911	0.709	0.869	0.717	0.752	0.814
Lu	0.123	0.19	0.09	0.119	0.088	0.108	0.100	0.093	0.108
Gd/Yb	8.27	8.27	12.7	12.8	12.1	12.3	13.7	13.6	16.2
La/Sm	8.38	8.43	8.52	8.52	7.70	7.72	8.01	7.94	8.07
La/Yb	98.7	101	168	171	147	148	169	169	229

† Normalized to primitive mantle values (Sun and McDnough,1989)

Chm – Hybrid magma composition

Cpm – Primary magma composition

7.5. D13 – PHLOGOPITE KIMBERLITE AND GROUP II KIMBERLITES (ORANGEITES)

The D13 – phlogopite kimberlite and the D14 – monticellite kimberlite show systematic variations in their REE_N patterns and K_2O (and Al_2O_3) contents. Because the lower Gd/Yb ratios and higher K_2O contents in the D13 – phlogopite kimberlite primary magma are unlike typical group I kimberlites (e.g., le Roex et al., 2003; Becker and le Roex, 2006), but are instead more characteristic of group II kimberlites (Becker and le Roex, 2006; Coe et al., 2008). Therefore, before considering the petrogenetic relationship that exists between the D13 – phlogopite kimberlite and other kimberlite intrusions in this study; the D13 – phlogopite kimberlite are first compared with group II kimberlites to gain better insight into their geochemical affinities K_2O and Gd/Yb.

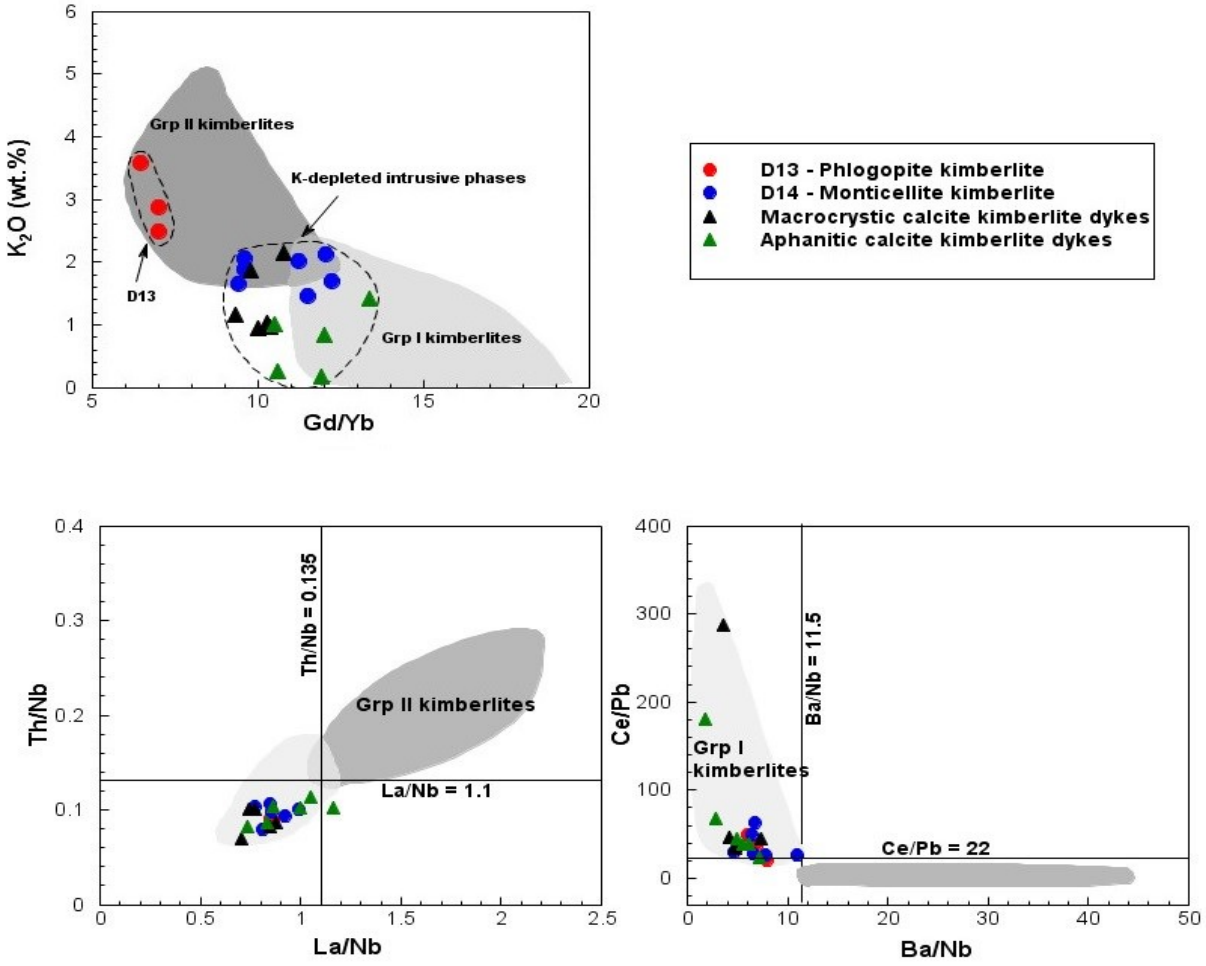

Figure 7.5: Bivariate plot showing K_2O vs Gd/Yb ratios and group I diagnostic incompatible element ratios in samples representative of kimberlite intrusions from the eastern lobe of the Du Toit pan kimberlite pipe. Fields of group I and II kimberlites is from le Roex et al. (2003). Field of group II kimberlites is from Becker and le Roex (2006).

Becker and le Roex (2006) showed that there are diagnostic incompatible element ratios (Th/Nb, La/Nb, Ce/Pb, Ba/Nb) that effectively discriminate between group I and II kimberlite source regions in southern African kimberlites. These diagnostic incompatible element ratios are used here to compare the D13 – phlogopite kimberlite and group II kimberlites from the region given their similarities in terms of K and Gd/Yb. Figure. 7.5 illustrates that the D13 – phlogopite kimberlite is characterized by diagnostic trace element ratios that are typical of southern African group I kimberlites (Th/Nb <0.135; La/Nb >1.1; Ce/Pb > 22; Ba/Nb >11.5) and that these are distinct from those typical of group II kimberlites. Therefore, despite their overlap in K – enrichment and Gd/Yb ratios, the D13 – phlogopite kimberlite and group II kimberlites are derived from distinct sources.

7.6. PARTIAL MELTING MODELS

Mathematical models that quantify the distribution of trace element concentrations in magmas during partial melting are well established (e.g., Gast, 1968; Shaw, 1970; Langmuir et al., 1977). In the evaluation of partial melting there are three models to consider (i.e., equilibrium, fractional, and dynamic melting). Differences in these melting models can be expressed mathematically in terms of the melt mass fraction in the residue [i.e., the mass porosity of the residue (ψ) vs the total degree of partial melting (F)] (Zou, 1998). During batch melting, the mass porosity is assumed to be equal to the degree of partial melting ($F = \psi$) until melt extraction is initiated and then $\psi = 0$ (Zou, 1998; Shaw, 2000). In this model the melt fraction remains in equilibrium with the residue throughout the partial melting process until a single 'batch' of melt escapes (Cox et al., 1979). During fractional melting the melt fraction escapes before re-equilibrating with the residue ($\psi = 0$) for the duration of melting. Because partial melting in nature is likely to be more dynamic and continuous rather than stagnant, to better constrain partial melting Langmuir et al. (1977) developed the continuous (dynamic) melting model. In the continuous (dynamic) melting model considered to be intermediate between equilibrium and fractional melting, $F = \psi$ only when $F \leq$ the critical mass porosity of the residue (Φ) and then $\psi = \Phi$, when $F \geq \Phi$ (Zou, 1998). To effectively model partial melting of kimberlite intrusions in this study, complex partial melting models (e.g., Langmuir et al., 1977; Hofmann and Feigensen, 1983) are not considered because they incorporate more parameters and therefore require more assumptions. This coupled with the inherent compositional modification already associated with kimberlites would increase uncertainty and decrease confidence in the models. Previous studies have developed simple batch (equilibrium) melting models that are in good agreement with observed geochemical variations in kimberlites (e.g., le Roex et al., 2003, Chalapathi et al., 2004; 2017, Harris et al., 2005; Becker and le Roex,

2006; Coe et al., 2008; Chalapathi and Dongre, 2009). In this section equilibrium melting models of Gast (1968) and Shaw (1970) are used to model the petrogenesis and characterize the source region(s) for kimberlite intrusions in this study. The mathematical expressions of the equilibrium (batch) melting is illustrated below

$$\frac{C_l}{C_o} = \frac{1}{F + D_0 - FP} \quad (4)$$

C_o = concentration of a trace element in the original mantle.

C_l = concentration of trace element in the melt

F = degree of partial melting

D = initial bulk distribution coefficient.

P = bulk reaction coefficient

7.6.1. Inverse modelling: REE source compositions

Semi-quantitative modelling is dependent on the following parameters; (1) the choice of source mineralogy (including its relative modal abundance), (2) the assumed degree of partial melting, (3) and the choice of primary magma compositions. In the following modelling it is always assumed that residual phases present in the source enter the melt according to their respective melting modes rather than their modal mineralogy, i.e. all partial melting is non –modal (D ≠P in eqn. 4). The equilibrium melting equation above is inverted to predict REE compositions in the source region for the kimberlite intrusions in this study. The selected parameters for the ensuing modelling are discussed below.

Source mineralogy (including its relative modal abundance)

Fractionated REE abundances in kimberlite intrusions in this study are indicative of partial melting in the presence of residual garnet (Table 7.2). Clinopyroxene is the most important repository of LREE in the mantle (Grégoire et al., 2003; Simon et al., 2007; le Roex and Class, 2016); while orthopyroxene and olivine are the most abundant minerals in mantle (Sun and McDonough, 1995). These minerals are consistent with an assumed garnet peridotite which is the dominant lithology below the Kimberley area (e.g., Gregoire et al., 2002; Simon et al., 2007) which is consistent with experimental studies (Wyllie, 1978; Eggler and Wendlandt, 1979; Canil and Scarfe, 1990; Dalton

and Presnall, 1998; Ulmer Sweeney, 2002; Gudfinnsson and Presnall, 2005; Brey et al., 2008). The assumed relative modal abundances are taken from average garnet peridotite from Grégoire et al. (2003) and Simon et al. (2007).

Assumed degree of partial melting

The degree of partial melting required to produce kimberlitic magmas (Mg/Ca >2; 25 wt. % >SiO_2) has been determined experimentally to be around F ~ 1% (Wyllie, 1978; Eggler and Wendlandt, 1979; Canil and Scarfe, 1990; Dalton and Presnall, 1998; Ulmer Sweeney, 2002; Gudfinnsson and Presnall, 2005; Brey et al., 2008). Some experimental studies have even suggested that there is primary magma continuum from carbonatitic (Mg/Ca ~1; 5 wt. % < SiO_2) to kimberlitic compositions with the transition occurring after ~0.6% degrees of partial melting (Dalton and Presnall, 1998; Brey et al., 2008). Therefore, ~0.6 % partial melting is assumed in the ensuing inverse modeling.

Choice of primary magma compositions

The choice of primary composition of any kimberlite intrusion is inconsequential because all intrusions are related in the subsequent section. Thus, the D14 – monticellite kimberlite are used in inverse modelling to determine source REE (Table 7.2). Partition coefficients used in the modelling are given in Table 7.1.The results of the modelling are given in Table 7.3 and calculated REE source compositions are illustrated in Figure 7.8. Calculated source region REE abundances are compared with calculated source compositions of le Roex et al. (2003) and the primitive mantle (Sun and McDonough, 1989). The results of the modelling are discussed below.

Table 7.3: Parameters used in non-modal (inverse) equilibrium melting to predict source region REE abundances for the various kimberlite intrusions. Melting proportions are from le Roex et al. (2003). Modal proportions from average GP and GPP from Grégoire et al. (2003) and Simon et al. (2007). Also shown are calculated source REE of kimberlite intrusions from the eastern lobe of the Du Toitspan kimberlite pipe compared with calculated source compositions from le Roex et al. (2003) and the primitive mantle from Sun and McDonough (1989).

Phase	Modal prop.	Melting prop.
Ol	0.66	0.05
Opx	0.25	0.05
Cpx	0.03	0.5
Grt	0.06	0.4

	Primitive mantle	Calculated mantle	
		F=0.6% (This study)	F=1% (le Roex et al. 2003)
K	250	152	260
La	0.69	1.45	1.86
Ce	1.78	3.25	5.14
Pr	0.28	0.45	0.67
Nd	1.35	2.07	2.77
Sm	0.44	0.33	0.47
Eu	0.17	0.11	0.14
Gd	0.60	0.39	0.42
Tb	0.11	0.07	0.06
Dy	0.74	0.37	0.32
Ho	0.16	0.07	0.05
Er	0.48	0.21	0.12
Tm	0.07	0.03	0.02
Yb	0.49	0.25	0.12
Lu	0.07	0.05	0.02
La/Sm_N		2.81	2.56
Gd/Yb_N		1.31	2.90
La/Yb_N		4.23	11.12

Assuming that the D14 – monticellite kimberlite formed from ~0.6% degrees of partial melting of a garnet peridotite, the results from the non-modal equilibrium (inverse) modelling indicate that the latter could have been derived from a source region that is enriched in LREE (La = 6.11 × chondrite; Yb = 1.47 × chondrite) (Table 7.3; Fig. 7.6). Relative to the primitive mantle, the calculated REE abundances are consistent with derivation from a source region having experienced prior melting (Yb = 0.49 × PM) and enrichment (La =2.03 × PM). The calculated source REE abundances are similar to those calculated by le Roex et al. (2003) for the Kimberley

kimberlites, and fall within the range of metasomatised peridotite xenoliths from the Kaapvaal craton in the region (Grégoire et al., 2003).

Until recently actual carbonated peridotites xenoliths in kimberlites remained elusive, however their existence in the Kaapvaal craton has recently been confirmed (Howarth et al., 2019). Importantly, in this study, the recovered carbonate peridotite xenoliths which were sampled by a Bultfontein kimberlite exhibit C-O-Sr-Nd-Pb isotope compositions that show a genetic link with the host kimberlite magma. Further, Re-Os isotopes of mantle xenoliths sampled from the western Kaapvaal craton provide direct evidence for the occurrence of a partial melting event in the Kimberley area during the Archean (~ 2.9 Ga) (Simon et al, 2007). Following le Roex et al. (2003), the source for kimberlite intrusion in this study are interpreted to have been derived from a source that is located within the sub-continental lithospheric mantle (SCLM) and is not unlike mantle xenoliths entrained by kimberlites in and around the area of Kimberley. Further evidence for the derivation of archetypal group I kimberlites from the SCLM comes from the first reported kimberlite quenched glass found to to have equilibrated within the lithospheric mantle (4.5 – 6 GPa; Howarth and Büttner, 2019) using the olivine Al-thermometer of De Hoog et al. (2010) subsequently modified by Bussweiler et al (2017).

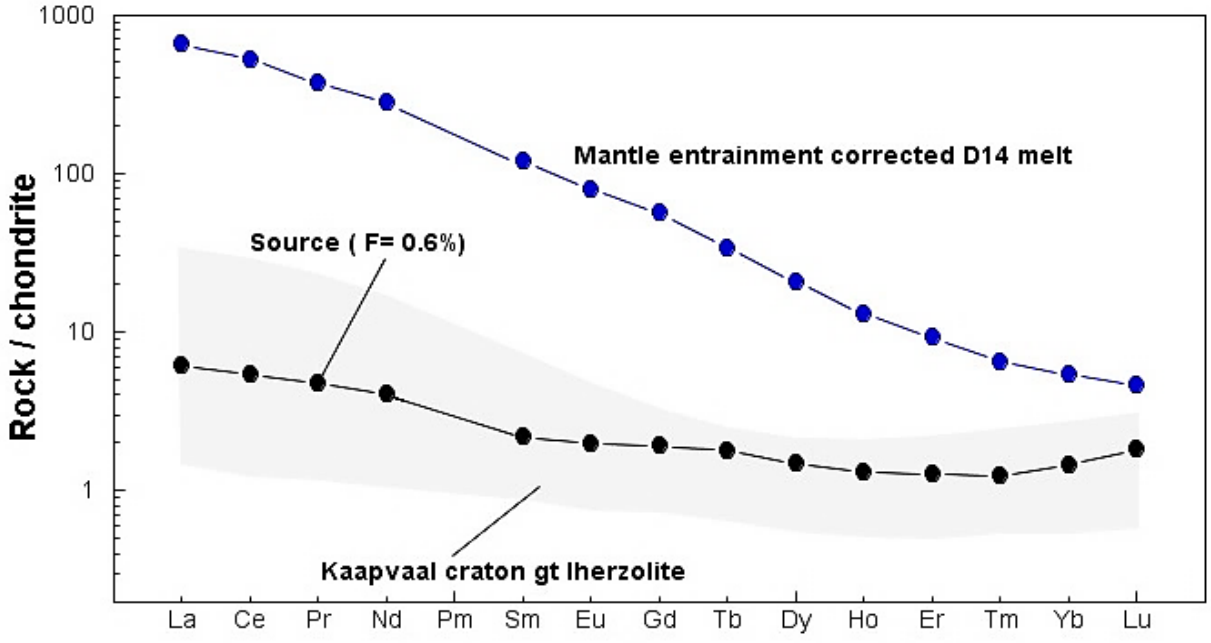

Figure 7.6: Chondrite – normalised diagrams REE patterns of calculated source from D14 – monticellite parental magma assuming 0.6% degrees of non-modal equilibrium melting. Modelling parameters given in Table 7.3. The field of Kaapvaal craton garnet lherzolites is from Grégoire et al. (2003).

7.6.2. Forward modelling: Residual clinopyroxene and garnet

In this section the conditions responsible for the petrogenesis of kimberlite intrusions in this study are evaluated. It was alluded to in the previous section that the D13 – phlogopite kimberlite has distinct REE_N patterns compared to the D14 – monticellite kimberlite and the calcite kimberlite dykes. The D13 – phlogopite kimberlite is the most distinct intrusion in this regard because it is characterized by lower Gd/Yb. The D14 – monticellite kimberlite and the calcite kimberlite dykes are in comparison are characterized by straighter HREE patterns (Gd/Yb = 12.3 – 16.2; La/Yb=171-229; Table 7.2). Fractioned REE abundances in primary magmas are an indication of melting in the presence of garnet, because the compatibility of REE in garnet increases systematically from La – Lu (see Table 7.1). Therefore, variable amounts of residual garnet in the source during partial melting will produce magmas with distinct HREE patterns. Because La/Sm ratios in the different kimberlite intrusions are sub-parallel it is unlikely that they were produced from significantly variable degrees of partial melting. The majority of clinopyroxene in depleted mantle xenoliths from the Kaapvaal craton has been argued to be of metasomatic origin (e.g., Grégoire et al., 2003; Simon et al., 2007). If indeed the amount of residual garnet is allowed to vary relative to clinopyroxene this could produce an array of equilibrium melts with fractionated HREE controlled by the relative proportion of garnet to clinopyroxene. To test this hypothesis forward constrained equilibrium melts ranging from 0.1 – 1.5% degrees of partial melting using the non-modal equilibrium equation of Shaw (1970), where all modelling parameters are kept constant (Table 7.3), but the relative proportion of garnet and clinopyroxene are made to vary. The results of this modelling are illustrated in Figures 7.7 and can be extended to include the full range of REE as shown in Figure 7.8 with parameters in Table 7.4.

Figure 7.8a shows that after F= 0.5-0.6% degrees of partial melting of a garnet peridotite containing source (66 vol.% olivine, 25 vol.% orthopyroxene, and 9 vol.% = garnet + clinopyroxene) with (cpx: grt = 67:33; Table 7.4), the lower Gd/Yb ratios in the D13 – phlogopite kimberlite can be accounted for. By simply increasing the proportion of garnet relative to clinopyroxene (cpx: grt = 33:67; Table 7.4) and keeping all other parameters constant, the relatively higher Gd/Yb ratios in the D14 monticellite kimberlite, macrocrystic calcite kimberlite and aphanitic phlogopite-rich calcite kimberlite parental magmas can be accounted for by slightly varying the degrees of partial melting of the same source in terms mineralogy. Assuming the derivation of the D14 monticellite kimberlite by ~0.6% degrees of partial melting, the results of the non-modal equilibrium melting indicate that the average macrocrystic calcite kimberlite and

the aphanitic phlogopite-rich calcite kimberlite could have been derived by F= 0.5% and F=0.4% degrees of partial melting, respectively.

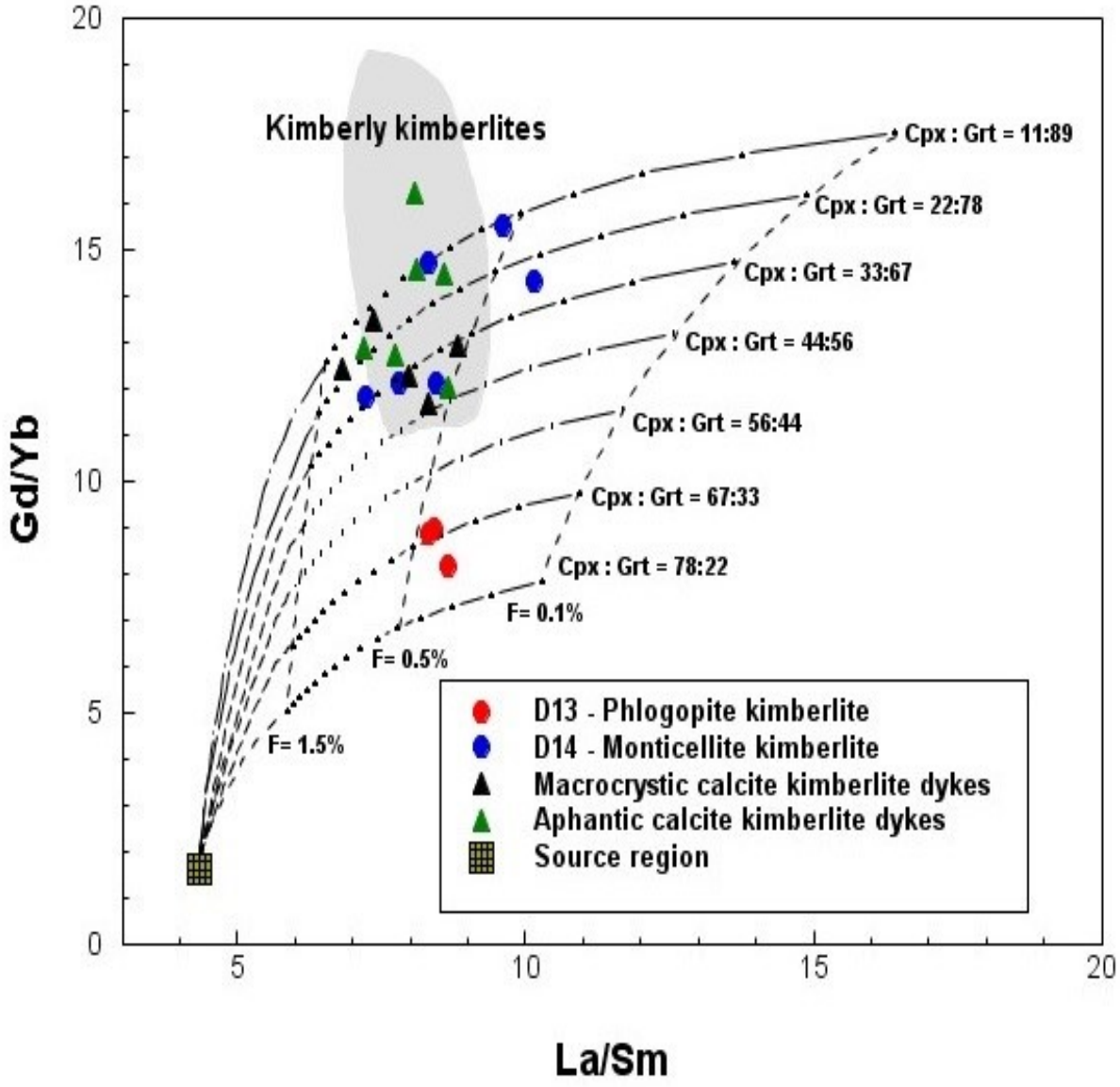

Figure 7.7: Bivariate plot of La/Sm vs Gd/Yb comparing calculated equilibrium melts and superimposed are compositions of the various kimberlite intrusions from the eastern lobe of the Du Toitspan kimberlite pipe. Different equilibrium melts represent distinct source mineralogy calculated from variable proportion cpx and grt (9 vol. %) degree of partial melting (F=0.1 -1.5). Field of group I kimberlites from le Roex et al. (2003). Source region composition given in Table 7.3.

On average the aphanitic opaque-rich calcite kimberlite and the aphanitic serpentine calcite kimberlite parental magmas with REE abundances that are almost indistinguishable despite their distinct Nb/Ta ratios. Their distinct Nb/Ta ratios are most likely controlled by the amount of entrained Mg-ilmenite *en-route* to surface and not their modal perovskite since their REE abundances are almost indistingushble. The results of the non-modal equilibrium partial melting modelling suggest that both aphanitic calcite kimberlite varieties are consistent with derivation from a more refractory source containing a higher proportion garnet relative to clinopyroxene (cpx :grt = 22:78) compared the D14 – monticellite kimberlite parental and associated macrocrystic and aphanitic calcite dykes. Interestingly, both the aphanitic opaque-rich calcite kimberlite dykes and the aphanitic serpentine calcite kimberlite dykes require relatively high degrees partial melts (F= 0.9%) compared to the major kimberlite intrusions

Table 7.4: A summary of parameters used in modelling presented in Figure. 7.8. Melting modes are the same as in Table 7.3. Opx = 25%, Ol = 66%.

Kimberlite intrusions	Peridotite Source				Degree of partial melting (F)
	Source Mineralogy	Mineral modes (vol. %)	Cpx: grt ratio = vol. 9%	Gd/Yb	
Avg. D13 phlogopite kimberlite (Cpm)	Cpx Grt	6 3	67:33	8.3	0.5%
Avg. D14 monticellite kimberlite (Cpm)	Cpx Grt	3 6	33:67	12.8	0.6%
Avg. Macrocrystic calcite dyke (Cpm)	Cpx Grt	3 6	33:67	12.3	0.6%
Aphanitic phlogopite -rich calcite kimberlite	Cpx Grt	3 6	33:67	16.2	0.4%
Avg. opaque-rich and serpentine calcite kimberlites	Cpx Grt	2 7	22.78	13.7	0.9%

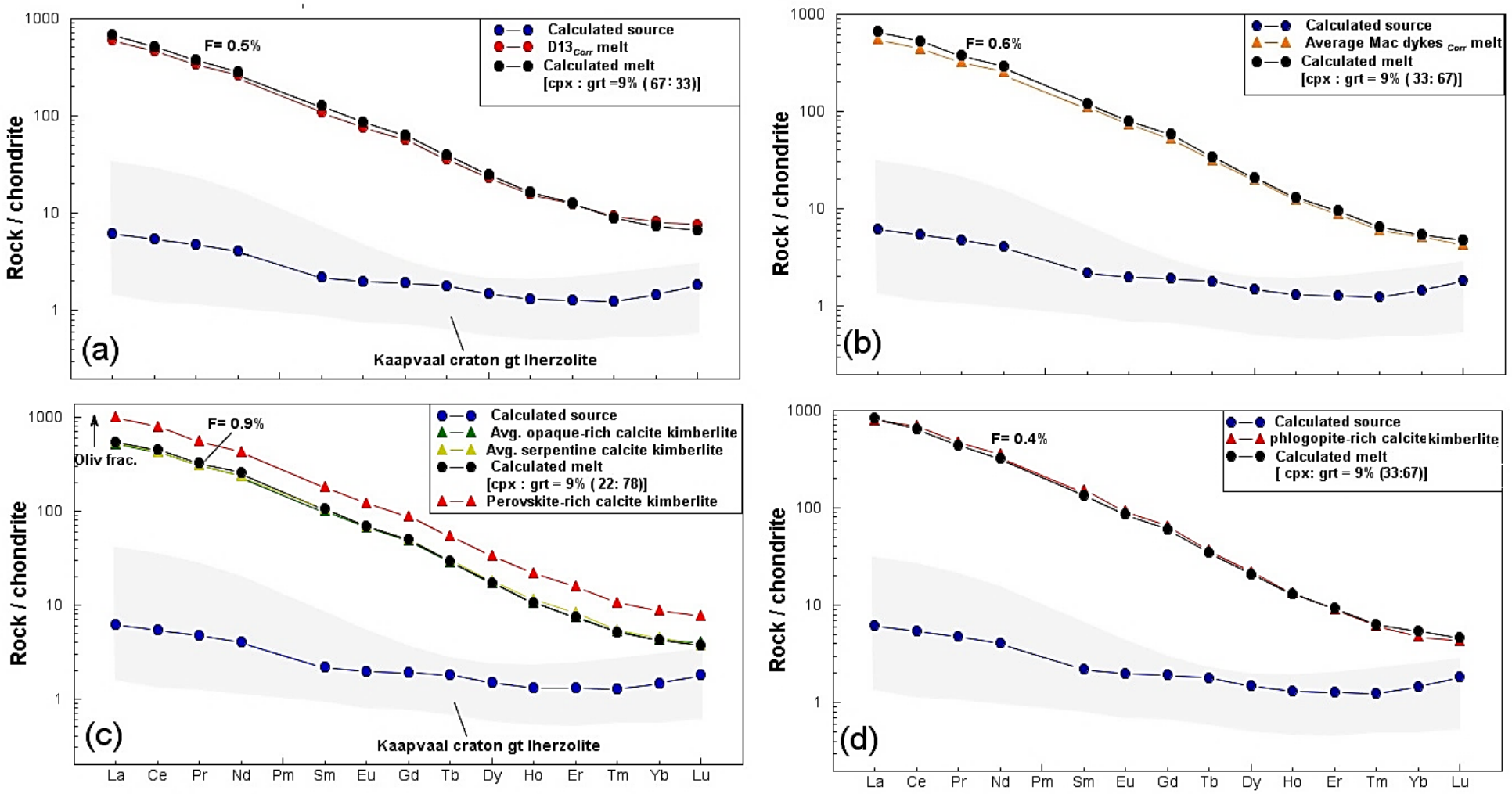

Figure 7.8: Chondrite – normalised diagrams of modelled REE patterns in calculated equilibrium melts compared with measured REE abundances of parental magma compositions for the various kimberlite intrusions from the eastern lobe of the Du Toitspan kimberlite pipe. Parameters of sources used in the forward constrained modelling are given in Table 7.3. Melting modes used are given in Table 7.2. The Kaapvaal craton field is from Grégoire et al. (2003). Chondrite normalising values from Sun and McDonough (1989).

7.7. Source region evolution

REE patterns in the different kimberlite intrusions from the eastern lobe of the Du Toitspan kimberlite pipe can be explained by variable degrees of partial melting of a single peridotite source composition in terms of REE provided that the proportion of residual garnet and clinopyroxene is allowed to vary from 7 vol.% garnet and 2 vol. % clinopyroxene to 3 vol. % garnet and 6 vol. % clinopyroxene (Table 7.4). This source mineralogy is not unlike typical metasomatised garnet from the lithospheric mantle beneath the Kimberley region (Gregoire et al., 2003; Simon et al., 2008). The variability in residual garnet relative to clinopyroxene in the source regions giving rise to kimberlite intrusions in this study is suggested to represent localised source heterogeneity. In the following section K variability in the D13 – phlogopite compared to the D14 – monticellite kimberlite and associated calcite kimberlite dykes in this study is evaluated.

7.7.1. Phlogopite equilibrium

Samples of the D13 – phlogopite kimberlite on primitive mantle normalised diagrams do not show K-anomalies that are characteristic of typical group I kimberlites (le Roex et al., 2003; Becker and le Roex, 2006), whereas the D14 – monticellite kimberlite and calcite kimberlite dykes are characterised by significant K-anomalies of variable magnitudes ($K/K^* = 0.04 - 0.55$). To evaluate whether K contents in the various kimberlite intrusions relate to source heterogeneity caused by crystallization of a K-bearing phase (in association with clinopyroxene) the approach taken is adopted from Späth et al. (2001). In this approach, K is treated as a stoichiometric component of the K-bearing phase present in the source rather than as a trace element that follows Henry's law (Späth et al., 2001). Thus, the amount of K- entering the melt will be controlled by the K_2O concentration of the specified K-bearing phase in the source.

The amount of K_2O entering the melt will remain fixed as long as the K-bearing phase in question remains a residual phase (Späth et al., 2001). Phlogopite and K-richterite are the main hosts of K_2O in the mantle and are both stable at P-T conditions that are compatible with kimberlite magmatism (e.g., Condamine et al., 2016; Konzett and Ulmer, 1999; Konzett and Fei, 2001). Erlank et al. (1987) identified the exsistence of a sequence of metasomatism that exists in xenoliths sampled by kimberlites from the Kimberley cluster rangeing from GP (Garnet

peridotite) – GPP (Garnet phlogopite peridotite) - PP (phlogopite peridotite) – PKP (phlogopite K-richterite peridotite). This sequence corresponds with a relative increase in the degree of metasomatism that exists along a continuum that spans from cryptic to modal metasomatism (Erlank et al., 1987). Van Achterbergh et al. (2001) recognised that the metasomatism continuum of Erlank et al. (1987) is much more systematically preserved in mantle xenoliths from the Zimbabwe craton found to be petrologically indistinguishable from mantle xenoliths found in the adjacent Kaapvaal craton, suggesting modification by a similar process (Stiefenhofer et al., 1997). Their study recognised that the transformation from cryptically metasomatised garnet peridotite (GP) to garnet ± phlogopite peridotite (GPP) is accompanied by the crystallization of metasomatic clinopyroxene and phlogopite which occurs at the expense of garnet [Grt → cpx + phl] at specimen scale.

If a similar scenario is considered for the source region giving rise to kimberlites in this study, then after adjusting for mantle entrainment, the D13 – phlogopite kimberlite primary magma containing K ~38 750 ppm (~ 4.67 wt. % K_2O; Table 7.2), is sufficiently enriched in K to have equilibrated against a source containing phlogopite, i.e. a phlogopite bearing peridotite (Fig. 7.9). Although the absence of K-anomalies in primitive mantle normalised diagrams for the D13 – phlogopite kimberlite suggests that phlogopite was exhausted shortly before or during melt segregation. Average phlogopite from the Kaapvaal craton peridotites contains ~10 wt. % K_2O (Giuliani et al., 2016). Therefore, assuming a smooth variation between Nb and Ta, the D13-phlogopite kimberlite source region which is interpolated to have K ~ 400 ppm, and could have thus equilibrated with a peridotite source containing accessory amounts of phlogopite (~0.2 vol.%) exhausted after ~0.3 – 0.4% degrees of partial melting before melt segregation after ~0.5 – 0.6% degrees of partial melting.

K-anomalies in the Kimberley kimberlites have been argued by le Roex et al (2003) to be inconsistent with partial melting in the presence of a K-bearing phase or with fractionation of a K-rich phase. Instead, these have been argued to be inherited from their source regions following their imprint in their source regions by a differentiated fluid already carrying a K-anomaly from earlier phlogopite crystallisation (le Roex et al., 2003; Becker and le Roex, 2006). Following le Roex et al. (2003) and Becker and le Roex (2006), K-anomalies in the D14 – monticellite kimberlite and associated calcite dykes are argued to have a similar origin with their lower K_2O arguing against equilibration with a source containing either phlogopite or K-richterite (Fig. 7.9).

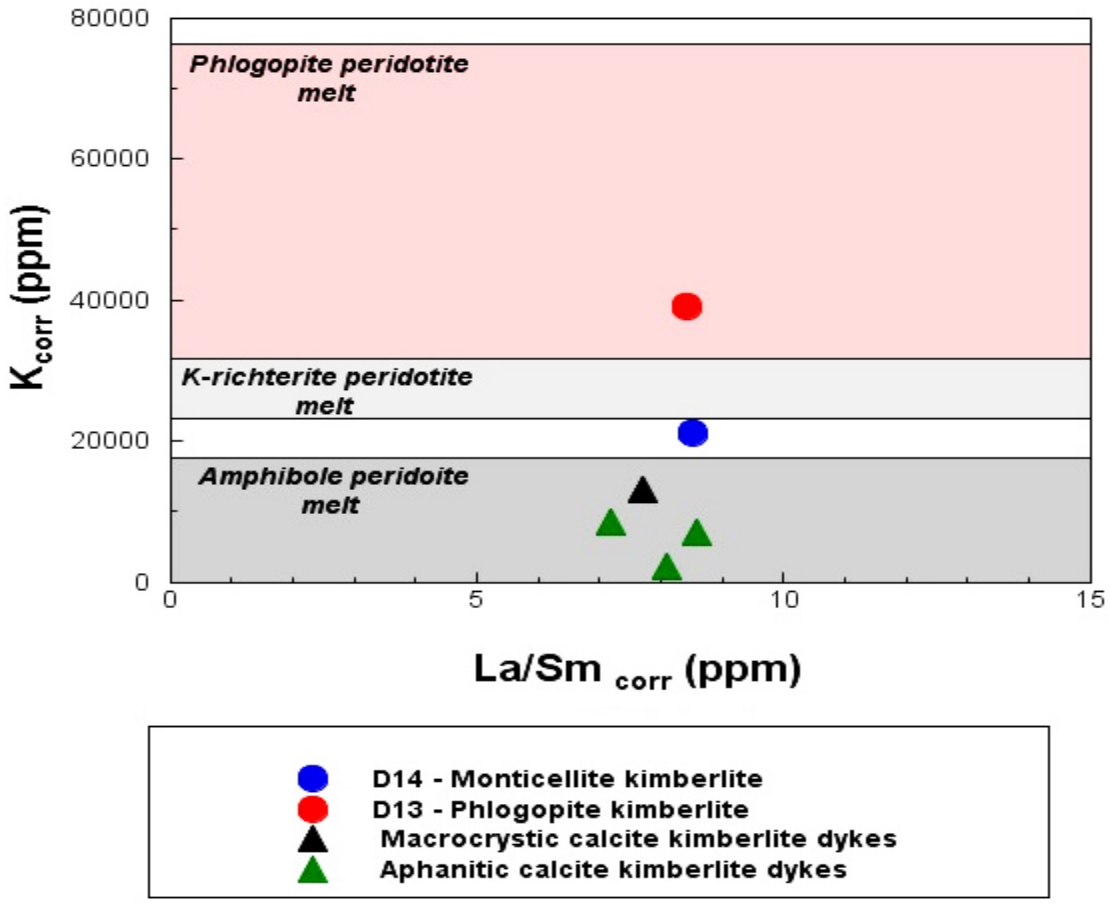

Figure 7.9: Bivariate plot showing K (ppm) vs La/Sm. Assuming that all K in the system is hosted in the respective K-bearing phases indicative of equilibration with a distinct source lithology based on variable K content (Adapted from Späth et al. 2001) (see text for further discussion).

7.7.2. Localised source heterogeneity and cause of magmatism

Semi quantitative partial melting models presented in the previous section are effective in demonstrating that the high K_2O (> 2 wt. %) and lower Gd/Yb ratios in the D13 – phlogopite kimberlite are consistent with low degree of partial melting (F=0.5 – 0.6%) of a phlogopite – bearing garnet peridotite (GPP) with a higher proportion of clinopyroxene relative to garnet. The lower K_2O (<2 wt. %) and higher Gd/Yb ratios in the D14 – monticellite kimberlite are consistent with similar degree of partial melting of a phlogopite – free garnet peridotite (GP), with a higher proportion of garnet relative clinopyroxene. The macrocrystic calcite kimberlite and the aphanitic phlogopite-rich calcite kimberlite dykes are related to the D14 – monticellite kimberlite by derivation from the same source, where subtle differences in their respective REE patterns can be explained by simply varying the degree of partial melting (F= 0.4 - 0.6%). On

average, REE abundances in the aphanitic opaque-rich calcite kimberlite and the aphanitic serpentine calcite kimberlite dykes are remarkably indistinguishable (Table 7.3), and show the strongest HREE depletion compared to other kimberlite intrusion in this study require derivation by higher degrees of partial melting (F= 0.9%) of a relatively more depleted refractory source that is perhaps closer to a garnet hartzburgite. At this relatively higher degree of partial melting it is likely that some melt fractions would have been emplaced along discrete structural discontinuities and thus could have experienced differentiation as consequence. The enrichment in incompatible elements and depletion in compatible elements in the perovskite-rich calcite kimberlite dyke is perhaps an of such differentiated magmas. Although this process is more likely to be more complex than simple equilibrium olivine fractionation. Further, given their derivation from a similar source, the D14 – monticellite kimberlites and associated calcite kimberlite dykes are likely to also be related by CO_2 degassing *en-route* to surface (Abersteiner et al., 2018).

The occurrence of CaO, K_2O and volatiles (CO_2 and H_2O) from oxidized zones near the base of cratons (Foley et al. 2019); as well as diagnostic trace element ratios (Ba/Nb, La/Nb, Th/Nb, Ce/Pb) in southern Africa group I kimberlites resembling those observed in Ocean Island Basalts (OIB) known to have a sublithospheric regions (Becker and le Roex, 2006; le Roex et al., 2003) in the geochemistry of kimberlite intrusions from this study is in good agreement with the proposed two – stage kimberlite petrogenetic models of le Roex et al. (2003) for kimberlites from the Kimberley cluster. In this model, kimberlites from the Kimberley cluster are argued to be derived from a melt depleted source that has been subsequently modified by the infiltrations of alkali-silicate melts (or fluids) inferred to be derived from an upwelling mantle plume in the region during the Mesozoic (Bell et al., 2005). If it is considered that a broadly homogenous source at regional scales was infiltrated by the same metasomatising agents, then the crystallization of metasomatic phlogopite and clinopyroxene (perhaps in bifurcating networks of PIC veins) could have been responsible for localised heterogeneity where source evolution can be expressed as in Figure 7.10; where the introduction of metasomstic phlogopite and clinopyroxene into depleted peridotite occured at the expense of garnet (and enstatite) (see Safonov et al., 2019 and references therein). Further evidence in support of this petrogenetic model comes from trace element and isotopic composition of clinopyroxene and phlogopite in PIC mantle xenoliths in the region which all show a genetic link with group I kimberlites from the Kimberley cluster (Gregoire et al., 2002, 2003; Fitzpayne et al., 2019). The upwelling Mesozoic mantle plume could have also provided the heat source required to raise the regional geotherm above the peridotite solidus resulting in the petrogenesis of the Du Toitspan kimberlite pipe (Fig. 7.10).

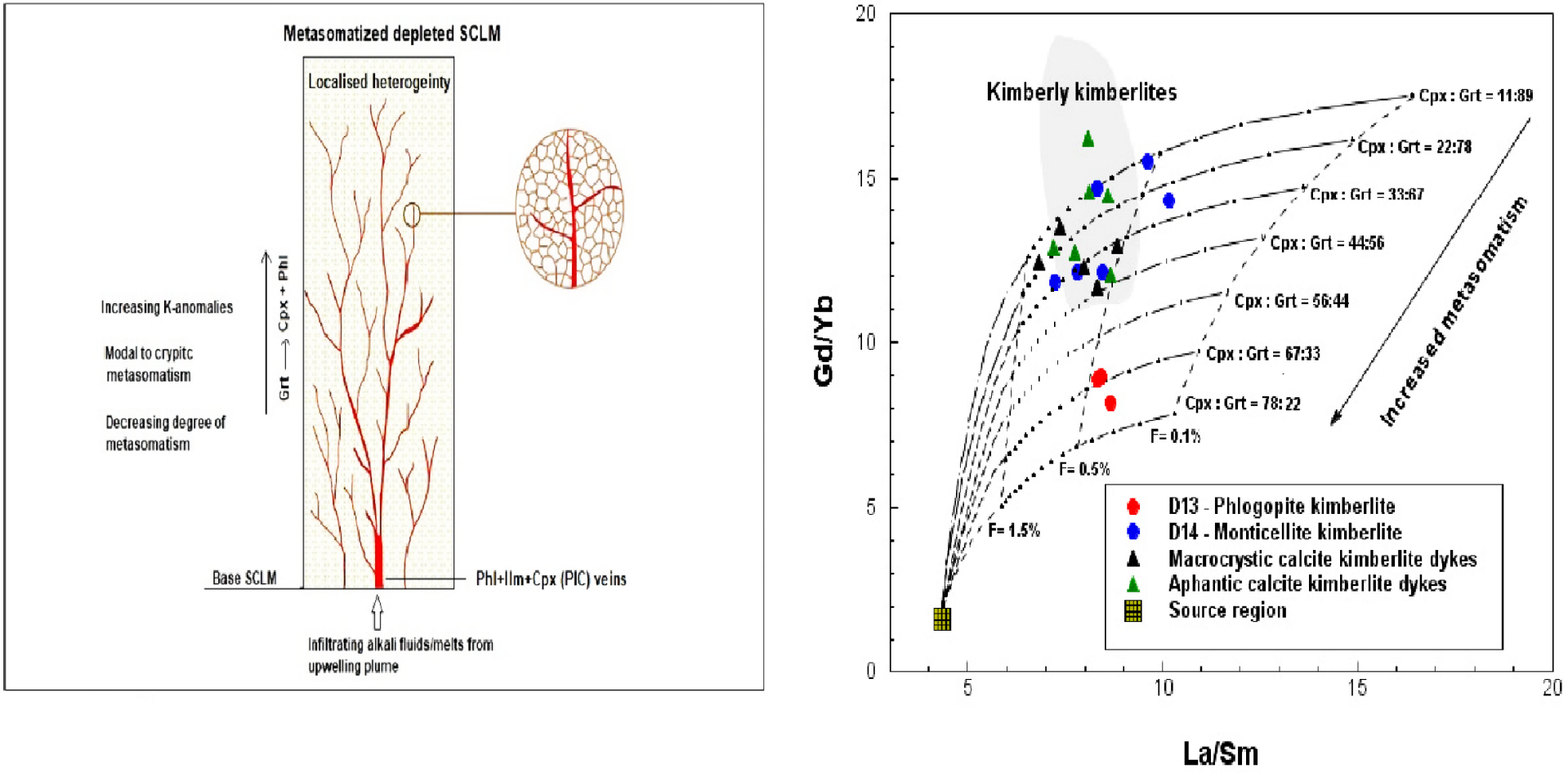

Figure 7.10: Petrogenesis of kimberlite intrusion and source heterogeneity. **(left)** a schematic illustrating alkali-silicate melts infiltrating a depleted refractory source crystallising phlogopite and clinopyroxene in (PIC?) veins with garnet consumption. Differentiated fluids imprint K-anomalies in more distal source regions from the PIC vein network (adapted from Eggins, 1992). **(right)** Gd/Yb vs La/Sm showing the petrogenesis of kimberlite intrusions in this study from a locally heterogeneous source. Parameters used in the modelling same as in Figure 7.7. Field of group I kimberlites is from le Roex et al. (2003). Arrow showing equilibrium melts produced from variably metasomstised source regions (inferred from Erlank et al., 1987)

CHAPTER 8: SUMMARY AND CONCLUSION

Kimberlite intrusions from the eastern lobe of the Du Toitspan kimberlite pipe have been analysed for their geochemistry with the aim of developing semi – quantitative models that place constraints on their petrogenesis and characterising their source region(s). This chapter provides a brief summary of salient aspects of previous chapters.

8.1. PETROGRAPHY

A total of twenty-seven samples collected from various kimberlite intrusions from the eastern lobe of the Du Toitspan kimberlite pipe were classified into; the D13 – phlogopite kimberlite, the D14 – monticellite kimberlite, D17 – serpentinized phlogopite kimberlite, and several internal as well as external calcite kimberlite dykes ranging in texture from macrocrystic to aphanitic. The aphanitic calcite kimberlite dykes were sub-divided further into; (2) opaque-rich calcite kimberlites, (2) serpentine calcite kimberlites, (1) phlogopite-rich calcite kimberlite and (1) perovskite-rich calcite kimberlite. Unlike other intrusions in this study the presence of magmaclasts and secondary microlitic diopside in the D17 – serpentinized phlogopite kimberlite suggests that it is not a hypabyssal kimberlite but rather solidified while transitioning from a hypabyssal towards a pyroclastic kimberlite in a near surface environment.

8.2. MINERAL CHEMISTRY

Electron probe microanalysis (EPMA) was used to measure major elements in olivines and phlogopites of selected samples representative of the different kimberlite intrusions. Although the D17 – serpentinized kimberlite was omitted from analysis due to alteration of these minerals. Olivine cores compositions in the macrocrystic kimberlite varieties are similar (Fo_{91-93}; NiO ~0.4 wt.%) but tend to be more variable in the aphanitic kimberlite varieties (Fo_{84-91}; NiO = 0.37 – 0.42 wt.%). Olivine rims compositions in the different kimberlite intrusions are similar with little variability (Fo_{87-89}; NiO = 0.24 – 0.39 wt.%). Phlogopite compositions show broad overlap, although a generous number of phlogopite microcrysts in the D13 – phlogopite kimberlite are slightly poorer in K_2O and richer F contents compared to most phlogopites in the D14 – monticellite kimberlite and the calcite kimberlite dykes.

8.3. MAJOR ELEMENT GEOCHEMISTRY

X-ray fluorescence (XRF) was used to measure major element compositions in samples representative of the different kimberlite intrusions. Major element unambiguously show the influence of crustal contamination in the D17 – serpentinized phlogopite kimberlite as evidenced by high contamination indices (1 – 1.5). High contamination indices in the D17 – serpentinized phlogopite kimberlite samples correlate positively with SiO_2, Al_2O_3, NaO_2; and negatively with MgO and K_2O. Negative SiO_2 – MgO correlation in the D17 – serpentinized phlogopite kimberlite provides further evidence of crustal contamination. Major elements in samples free from contamination generally show broad overlap except for richer K_2O (2.48 – 3.56 wt.%) and Al_2O_3 (3.34 – 5.07 wt.%) in the D13 – phlogopite kimberlite compared to poorer K_2O (< 2 wt.%) and Al_2O_3 (< 3 wt.%) in the D14 – monticellite kimberlite and the calcite kimberlite dykes. The influence of mantle entrainment on the major elements are most recognisable in the more macrocrystic samples. Although there are some subtle intra – intrusion geochemical variations among the aphanitic calcite kimberlite dykes, with richer CaO and TiO_2 and poorer MgO and SiO_2 in the perovskite – rich calcite kimberlite being suggestive of fractionation.

8.4. TRACE ELEMENT GEOCHEMISTRY

Inductively coupled plasma mass spectrometry (ICP-MS) and X-ray fluorescence (XRF) were used to measure trace element compositions in samples representative of the different kimberlite intrusions. Compatible element in the different kimberlite intrusions are variable (Ni = 598 – 1472 ppm; Cr = 1384 – 1918 ppm; Sc= 18.5 – 38.3 ppm; Co = 76.6 – 111 ppm) and show influence of mantle entrainment in the macrocrystic kimberlite varieties and fractionation in the perovskite – rich calcite kimberlite. LILE concentration show the influence of low temperature and post – emplacement alteration in the various kimberlite intrusions as evidenced by their incoherency and wide variability (Rb = 9.32 – 131 ppm ; Ba = 193 – 1888 ppm ; Sr = 585 – 1656 ppm). HFSE concentrations in the various kimberlite also show less variability (Nb = 103 – 160 ppm; Th = 9.20 – 14.7ppm ; Zr = 190 – 267 ppm) and are remarkably coherent and describe excellent positive correlations, with the strongest enrichment in the aphanitic perovskite – rich calcite kimberlite. REE_N patterns in the various kimberlite intrusions have sub-parallel and overall similar LREE (La/Sm_N = 4.3 – 6.5), with distinct HREE patterns. The D13 – phlogopite kimberlite is characterised by flattening HREE (La/Yb_N = 66.9 – 73.7 ; Gd/Yb_N = 6.5 – 7.0) and the D14 – monticellite kimberlite and calcite kimberlite dykes are by relatively straightening HREE (La/Yb_N = 94.1 – 164 ; Gd/Yb_N = 9.3 – 13.4). Superimposed on extended trace element primitive mantle normalised diagrams for the D14 – monticellite kimberlite and calcite kimberlite dyke are K, Sr, Ti, and Hf negative anomalies of

variable magnitudes (K/K* =0.04 – 0.46 ; Ti/Ti = 0.20 – 0.61 ; Hf/Hf* = 0.52 – 0.71 ; Sr/Sr* = 0.29 – 0.93). The D13 – phlogopite kimberlite samples also show Sr, Ti, and Hf negative anomalies but are distinguished by the absence of K-anomalies on primitive mantle normalised diagrams.

8.5. PETROGENESIS

Major and trace elements in the various kimberlite intrusions show the influence of either or some combination of compositional modification by low temperature alteration, fractionation, and mantle entrainment process. REE enrichment and Ni depletion in the perovskite-rich calcite kimberlite are consistent with 20 – 50% olivine fractionation of the parental aphanitic serpentine calcite kimberlite. Although other incompatible elements (e.g., Nb, Zr) in the aphanitic perovskite-rich calcite kimberlite show greater abundances than those predicted by equilibrium and fractional crystallization models. All other aphanitic calcite kimberlite could not be related by olivine fractionation and were considered to represent distinct primary magmas in their own rights given their refractory compositions. Given evidence that immobile elements in the various samples have remained resilient to low temperature alteration, their variations are considered to be of petrogenetic significance. Using a combination of the lever rule and two-component mixing mass balance equations, REE and K contents in the macrocrystic kimberlite varieties were corrected for the effects of mantle entrainment and assimilation. Partial melting models demonstrate that distinct $HREE_N$ patterns between the D13 – phlogopite kimberlite and D14 – monticellite kimberlite can be explained by variable degrees of partial melting of a single source composition provided that the proportion of residual garnet and clinopyroxene is allowed to vary slightly. The D14 – monticellite kimberlite are related to the macrocrystic calcite kimberlite and aphanitic phlogopite-rich calcite kimberlite dykes, where subtle differences in their REE abundances can be explained F=0.6% and F=0.4% degrees of partial melting of the same source. The K-enrichment in the D13 – phlogopite kimberlite can be explained by with a phlogopite – bearing garnet peridotite, although the absence of K-anomalies relative to the primitive mantle suggests that phlogopite was not a residual phase. The crystallization of clinopyroxene and phlogopite (and ilmenite?) via reactive prosperous with garnet consumption by alkali- silicate melts from an upwelling Mesozoic plume beneath the Kaapvaal craton is argued to have been responsible for the localised source heterogeneity, which subsequently provided the heat source required for the petrogenesis of the Du Toitspan kimberlite pipe.

REFERENCES

Abersteiner, A., Kamenetsky, V.S., Pearson, D.G., Kamenetsky, M., Goemann, K., Ehrig, K. and Rodemann, T., 2018. Monticellite in group-I kimberlites: Implications for evolution of parental melts and post-emplacement CO_2 degassing. *Chemical Geology*, *478*, pp.76-88.

Abersteiner, A., Kamenetsky, V.S., Goemann, K., Golovin, A.V., Sharygin, I.S., Giuliani, A., Rodemann, T., Spetsius, Z.V. and Kamenetsky, M., 2019. Djerfisherite in kimberlites and their xenoliths: implications for kimberlite melt evolution. *Contributions to Mineralogy and Petrology, 174*(1), p.8.

Afanasyev, A., Melnik, O., Porritt, L., Schumacher, J.C., Sparks, R.S.J., 2014. Hydrothermal alteration of kimberlite by convective flows of external water. *Contributions to Mineralogy and Petrology, 168* (1), pp.1–17.

Allsopp, H.L. and Barrett, D.R., 1975. Rb–Sr age determinations on South African kimberlite pipes. In *Physics and Chemistry of the Earth* (pp. 605-617). Pergamon.

Altermann, W. and Lenhardt, N., 2012. The volcano-sedimentary succession of the Archean Sodium Group, Ventersdorp Supergroup, South Africa: volcanology, sedimentology and geochemistry. *Precambrian Research*, *214*, pp.60-81.

Arndt, N.T., Guitreau, M., Boullier, A.M., Le Roex, A., Tommasi, A., Cordier, P. and Sobolev, A., 2010. Olivine, and the origin of kimberlite. *Journal of Petrology,* 51(3), pp.573-602.

Beard, A.D., Downes, H., Hegner, E., Sablukov, S.M., Vetrin, V.R. and Balogh, K., 1998. Mineralogy and geochemistry of Devonian ultramafic minor intrusions of the southern Kola Peninsula, Russia: implications for the petrogenesis of kimberlites and melilitites. *Contributions to Mineralogy and Petrology*, *130*(3-4), pp.288-303.

Becker, M. and Le Roex, A.P., 2006. Geochemistry of South African on-and off-craton, Group I and Group II kimberlites: petrogenesis and source region evolution. *Journal of Petrology*, *47*(4), pp.673-703.

Becker, M., le Roex, A.P. and Class, C., 2007. Geochemistry and petrogenesis of South African transitional kimberlites located on and off the Kaapvaal Craton. *South African Journal of Geology*, *110*(4), pp.631-646.

Bell, D.R., Gregoire, M., Grove, T.L., Chatterjee, N., Carlson, R.W. and Buseck, P.R., 2005. Silica and volatile-element metasomatism of Archean mantle: a xenolith-scale example from the Kaapvaal Craton. *Contributions to Mineralogy and Petrology, 150*(3), p.251.

Berg, G.W., 1998, April. Geochemical Relations which reflect the History of Kimberlites from the Type area of Kimberley, South Africa. In International Kimberlite Conference: Extended Abstracts (Vol. 7, pp. 76-78).

Birch, G.F., 1981. The Karbonat-Bombe: a precise, rapid and cheap instrument for determining calcium carbonate in sediments and rocks. *Trans. Geol. Soc. S. Afr*, *84*, pp.199-203.

Brey, G.P., Bulatov, V.K., Girnis, A.V., Lahaye, Y., 2008. Experimental melting of carbonated peridotite at 6–10 GPa. *Journal of Petrology 49* (4), pp.797–821.

Brooker, R.A., Sparks, R.S.J., Kavanagh, J.L., Field, M., 2011. The volatile content of hypabyssal kimberlite magmas: some constraints from experiments on natural rock compositions. *Bulletin of Volcanology , 73* (8), pp. 959–981.

Bussweiler, Y., 2019. Polymineralic Inclusions in Megacrysts as Proxies for Kimberlite Melt Evolution—A Review. *Minerals, 9(9)*, p.530.

Bussweiler, Y., Brey, G.P., Pearson, D.G., Stachel, T., Stern, R.A., Hardman, M.F., Kjarsgaard, B.A. and Jackson, S.E., 2017. The aluminum-in-olivine thermometer for mantle peridotites—Experimental versus empirical calibration and potential applications. *Lithos, 272*, pp.301-314.

Canil, D. and Scarfe, C.M., 1990. Phase relations in peridotite+ CO_2 systems to 12 GPa: implications for the origin of kimberlite and carbonate stability in the Earth's upper mantle. *Journal of Geophysical Research: Solid Earth, 95*(B10), pp.15805-15816.

Chalapathi Rao, N.V., 2005. A petrological and geochemical reappraisal of the Mesoproterozoic diamondiferous Majhgawan pipe of central India: evidence for transitional kimberlite–orangeite (group II kimberlite)–lamproite rock type. *Mineralogy and Petrology*, *84*(1-2), pp.69-106.

Chalapathi Rao, N.V., Gibson, S.A., Pyle, D.M. and Dickin, A.P., 2004. Petrogenesis of Proterozoic lamproites and kimberlites from the Cuddapah Basin and Dharwar craton, southern India. *Journal of Petrology*, *45*(5), pp.907-948.

Chalapathi Rao, N.V. and Dongre, A.N., 2009. Mineralogy and geochemistry of kimberlites Nk–2 and kk–6, Narayanpet kimberlite field, eastern Dharwar craton, southern India: evidence for a transitional kimberlite signature. *The Canadian Mineralogist, 47*(5), pp.1117-1135.

Clement, C.R., 1982. A comparative geological study of some major kimberlite pipes in the Northern Cape and Orange Free State. Unpublished Ph.D. thesis, University of Cape Town, Cape Town, 431 pp.

Clement, C. R., Skinner, E. M. W. and Scott Smith, B. H. (1984) Kimberlite Redefined, *The Journal of Geology*. University of Chicago Press, 92(2), pp. 223–228.

Clement, C.R., Skinner, E.M.W., 1985. A textural-genetic classification scheme of kimberlites. *Transactions of the Geological Society of South Africa* 88, pp. 403–409.

Clement, C.R., Reid, A.M., 1989. The origin of kimberlite pipes: an interpretation based on the synthesis of geological features displayed by southern African occurrences. In: Ross, J., Jacques, A.L., Ferguson, J., Green, D.H., O'Reilly, S.Y., Danchin, R.V., Janse, A.J.A. (Eds.), *Kimberlites and Related Rocks, Volume 1. Proceedings of the Fourth International Kimberlite Conference.* Geological Society of Australia Special Publication 14, Perth, Australia, pp. 632–646.

Coe, N., le Roex, A., Gurney, J., Pearson, D.G. and Nowell, G., 2008. Petrogenesis of the Swartruggens and Star Group II kimberlite dyke swarms, South Africa: constraints from whole rock geochemistry. *Contributions to Mineralogy and Petrology, 156*(5), pp.627-652.

Condamine, P., Médard, E. and Devidal, J.L., 2016. Experimental melting of phlogopite-peridotite in the garnet stability field. *Contributions to Mineralogy and Petrology, 171*(11), p.95.

Cordier, C., Sauzeat, L., Arndt, N.T., Boullier, A.M., Batanova, V. and Barou, F., 2015. Metasomatism of the lithospheric mantle immediately precedes kimberlite eruption: new evidence from olivine composition and microstructures. *Journal of Petrology*, *56*(9), pp.1775-1796.

Cox, K. G., Bell, J. D. and Pankhurst, R. (1979) *The interpretation of igneous rocks*. 1st edn. Springer-Science+Business Media, B.V.

Dalton, J.A., Presnall, D.C., 1998. The continuum of primary carbonatitic–kimberlitic melt compositions in equilibrium with lherzolite: data from the system CaO-MgO-Al2O3-SiO2-CO2 at 6 GPa. *Journal of Petrology, 39* (11–12), pp.1953–1964.

Dawson, J.B., 1971. Advances in kimberlite geology. *Earth Science Reviews 7*, pp. 187–214.

De Hoog, J.C., Gall, L. and Cornell, D.H., 2010. Trace-element geochemistry of mantle olivine and application to mantle petrogenesis and geothermobarometry. *Chemical Geology, 270*(1-4), pp.196-215.

Dongre, A. and Tappe, S., 2019. Kimberlite and carbonatite dykes within the Premier diatreme root (Cullinan Diamond Mine, South Africa): New insights to mineralogical-genetic classifications and magma CO2 degassing. *Lithos*, 338, pp.155-173.

Drennan, G.R., Robb, L.J., Meyer, F.M., Armstrong, R.A. and De Bruiyn, H., 1990. The nature of the Archaean basement in the hinterland of the Witwatersrand Basin: II. A crustal profile west of the Welkom Goldfield and comparisons with the Vredefort crustal profile. *South African Journal of Geology, 93*(1), pp.41-53.

Duncan, A.R. and Marsh, J.S. (2006) 'The Karoo Igneous Province', in Johnson, M.R., Anhaeusser, C.R.

and Thomas, R. J. (Eds.). (ed.) *The Geology of South Africa.* Geological Society of South Africa, pp. 501–520.

Eggins, S.M., 1992. Petrogenesis of Hawaiian tholeiites: 1, phase equilibria constraints. *Contributions to Mineralogy and Petrology, 110*(2-3), pp.387-397.

Eggler, D. H., and Wendlandt, R.F. 1979. Experimental studies on the relationships between kimberlite magma and partial melting of peridotite. In: Boyd F.R. and Meyer, H.O.A. (Eds.), *Kimberlites, Diatremes and Diamonds: Their Geology, Petrology, and Geochemistry*. American Geophysical Union, New York, pp. 331-378.

Erlank, A.J., Waters, F.G., Hawkesworth, C.J., Haggerty, S.E., Allsopp, H.L., Rickard, R.S., Menzies, M., 1987. 'Evidence for mantle metasomatism in peridotite nodules from the Kimberley pipes, South Africa.' In: Menzies, M., Hawkesworth, C.J. (Eds.), Mantle Metasomatism. Academic Press, London, pp. 221–309.

Field, M., Stiefenhofer, J., Robey, J. and Kurszlaukis, S., 2008. Kimberlite-hosted diamond deposits of southern Africa: a review. *Ore Geology Reviews, 34*(1-2), pp.33-75.

Field, M. and Smith, B.S., 1998, April. Textural and genetic classification schemes for kimberlites: a new perspective. In *International Kimberlite Conference: Extended Abstracts* (Vol. 7, No. 1, pp. 214-216).

Fitzpayne, A., Giuliani, A., Maas, R., Hergt, J., Janney, P. and Phillips, D., 2019. Progressive metasomatism of the mantle by kimberlite melts: Sr–Nd–Hf–Pb isotope compositions of MARID and PIC minerals. *Earth and Planetary Science Letters*, *509*, pp.15-26.

Foley, S.F., Yaxley, G.M. and Kjarsgaard, B.A., 2019. Kimberlites from source to surface: insights from experiments. *Elements: An International Magazine of Mineralogy, Geochemistry, and Petrology, 15*(6), pp.393-398.

Fraser, K.J. and Hawkesworth, C.J., 1992. The petrogenesis of group 2 ultrapotassic kimberlites from Finsch Mine, South Africa. *Lithos, 28*(3-6), pp.327-345.

Fraser, K.J., Hawkesworth, C.J., Erlank, A.J., Mitchell, R.H. and Scott-Smith, B.H., 1985. Sr, Nd and Pb isotope and minor element geochemistry of lamproites and kimberlites. *Earth and Planetary Science Letters, 76*(1-2), pp.57-70.

Fritiofsson, S, 2014. Kaapvaal Craton basement exposed in Diamond mines at Kimberley, South Africa -Greenstone belt schists and amphibolites.

Gast, P.W., 1968. Trace element fractionation and the origin of tholeiitic and alkaline magma types. *Geochimica et Cosmochimica Acta, 32*(10), pp.1057-1086.

Gaudet, M., Kopylova, M., Muntener, C., Zhuk, V. and Nathwani, C., 2018. Geology of the Renard 65 kimberlite pipe, Québec, Canada. *Mineralogy and Petrology, 112*(2), pp.433-445.

Giuliani, A., Phillips, D., Kamenetsky, V.S. and Goemann, K., 2016. Constraints on kimberlite ascent mechanisms revealed by phlogopite compositions in kimberlites and mantle xenoliths. *Lithos, 240*, pp.189-201.

Giuliani, A., 2018. Insights into kimberlite petrogenesis and mantle metasomatism from a review of the compositional zoning of olivine in kimberlites worldwide. *Lithos, 312*, pp.322-342.

Golovin, A.V., Sharygin, I.S., Kamenetsky, V.S., Korsakov, A.V. and Yaxley, G.M., 2018. Alkali-carbonate melts from the base of cratonic lithospheric mantle: links to kimberlites. *Chemical Geology, 483*, pp.261-274.

Greenough, J.D., 1988. Minor phases in the Earth's mantle: evidence from trace-and minor-element patterns in primitive alkaline magmas. *Chemical Geology, 69*(3-4), pp.177-192.

Grégoire, M., Bell, D.R. and Le Roex, A.P., 2003. Garnet lherzolites from the Kaapvaal Craton (South Africa): trace element evidence for a metasomatic history. *Journal of Petrology, 44*(4), pp.629-657.

Grégoire, M., Bell, D. and Le Roex, A., 2002. Trace element geochemistry of phlogopite-rich mafic mantle xenoliths: their classification and their relationship to phlogopite-bearing peridotites and kimberlites revisited. *Contributions to Mineralogy and Petrology, 142*(5), pp.603-625.

Gudfinnsson, G.H., Presnall, D.C., 2005. Continuous gradations among primary carbonatitic, kimberlitic, melilititic, basaltic, picritic, and komatiitic melts in equilibrium with garnet lherzolite at 3–8 GPa. Journal of Petrology 46 (8), 1645–1659.

Hanson, E.K., Moore, J.M., Bordy, E.M., Marsh, J.S., Howarth, G. and Robey, J.V.A., 2009. Cretaceous erosion in central South Africa: Evidence from upper-crustal xenoliths in kimberlite diatremes. *South African Journal of Geology, 112*(2), pp.125-140.

Hart, S.R. and Davis, K.E., 1978. Nickel partitioning between olivine and silicate melt. Earth and Planetary Science Letters, 40(2), pp.203-219.

Hawthorne, J.B., 1975. Model of a kimberlite pipe. *Physics and Chemistry of the Earth, 9*, pp.1-15.

Herzberg, C. and O'Hara, M.J., 2002. Plume-associated ultramafic magmas of Phanerozoic age. *Journal of Petrology, 43*(10), pp.1857-1883.

Hetman, C.M., Smith, B.S., Paul, J.L. and Winter, F., 2004. Geology of the Gahcho Kue kimberlite pipes, NWT, Canada: root to diatreme magmatic transition zones. *Lithos, 76*(1-4), pp.51-74.

Howarth, G.H., Taylor, L.A., 2016. Multi-Step kimberlite evolution tracked in zoned olivine from the Benfontein sill, South Africa. *Lithos 262*, pp. 384–397.

Howarth, G.H., Büttner, S.H. 2019. New constraints on archetypal South African kimberlite petrogenesis from quenched glass-rich melt inclusions in olivine megacrysts. *Gondwana Research, 68,* pp. 116-126.

Howarth, G.H., Moore, A.E., Harris, C., van der Meer, Q.H. and le Roux, P., 2019. Crustal versus mantle origin of carbonate xenoliths from Kimberley region kimberlites using CO -Sr-Nd-Pb isotopes and trace element abundances. Geochimica et Cosmochimica Acta.

Howarth, G.H. and Giuliani, A., 2020. Contrasting types of micaceous kimberlite-lamproite magmatism from the Man Craton (West Africa): New insights from petrography and mineral chemistry. *Lithos,* p.105483.

Hunter, D. R., 2006. The Geology of South Africa, in Johnson, M. ., Thomas, C., and Anhaeusser, R. J. (eds) The Geology of South Africa. 2nd edn. Council for Geosciences, pp. 1 –9.

Jochum, K.P., Weis, U., Schwager, B., Stoll, B., Wilson, S.A., Haug, G.H., Andreae, M.O. and Enzweiler, J., 2016. Reference values following ISO guidelines for frequently requested rock reference materials. *Geostandards and Geoanalytical Research, 40(3)*, pp.333-350.

Kamenetsky, V.S., Kamenetsky, M.B., Sobolev, A.V., Golovin, A.V., Demouchy, S., Faure, K., Sharygin, V.V., Kuzmin, D.V., 2008. Olivine in the Udachnaya-East kimberlite (Yakutia, Russia): types, compositions and origins. *Journal of Petrology, 49*(4), pp. 823–839.

Kamenetsky, V.S., Golovin, A.V., Maas, R., Giuliani, A., Kamenetsky, M.B., Weiss, Y., 2014. Towards a new model for kimberlite petrogenesis: Evidence from unaltered kimberlites and mantle minerals. *Earth-Science Reviews 139*, pp.145–167.

Kargin, A.V., Sazonova, L.V., Nosova, A.A., Lebedeva, N.M., Kostitsyn, Y.A., Kovalchuk, E.V., Tretyachenko, V.V. and Tikhomirova, Y.S., 2019. Phlogopite in mantle xenoliths and kimberlite from the Grib pipe, Arkhangelsk province, Russia: Evidence for multi-stage mantle metasomatism and origin of phlogopite in kimberlite. *Geoscience Frontiers, 10*(5), pp.1941-1959.

Kilinc, A., 1989. Partial melting of crustal rocks, *Engineering Geology, 27*(1–4), pp. 279–299.

Kjarsgaard, B. , 2007. Kimberlite pipe models: significance for exploration, In Milkereit, B. (ed.) *Proceedings of Exploration: Fifth Decennial International Conference on Mineral Exploration*. 7 edn. Ottawa, Canada, pp. 667–677.

Kjarsgaard, B.A., Pearson, D.G., Tappe, S., Nowell, G.M. and Dowall, D.P., 2009. Geochemistry of hypabyssal kimberlites from Lac de Gras, Canada: comparisons to a global database and

applications to the parent magma problem. *Lithos, 112*, pp.236-248.

Konzett, J. and Fei, Y., 2000. Transport and storage of potassium in the Earth's upper mantle and transition zone: an experimental study to 23 GPa in simplified and natural bulk compositions. *Journal of Petrology*, 41(4), pp.583-603.

Konzett, J. and Ulmer, P., 1999. The stability of hydrous potassic phases in lherzolitic mantle—an experimental study to 9.5 GPa in simplified and natural bulk compositions. *Journal of Petrology, 40*(4), pp.629-652.

Kopylova, M.G., Matveev, S. and Raudsepp, M., 2007. Searching for parental kimberlite melt. *Geochimica et Cosmochimica Acta, 71*(14), pp.3616-3629.

Langmuir, C.H., Bender, J.F., Bence, A.E., Hanson, G.N. and Taylor, S.R., 1977. Petrogenesis of basalts from the FAMOUS area: Mid-Atlantic Ridge. *Earth and Planetary Science Letters*, 36(1), pp.133-156.

Le Maitre, R.W., Streckeisen, A., Zanettin, B., Le Bas, M.J., Bonin, B. and Bateman, P. eds., 2005. *Igneous rocks: a classification and glossary of terms: recommendations of the International Union of Geological Sciences Subcommission on the Systematics of Igneous Rocks*. Cambridge University Press.

Le Roex, A.P., Bell, D.R. and Davis, P., 2003. Petrogenesis of group I kimberlites from Kimberley, South Africa: evidence from bulk-rock geochemistry. *Journal of Petrology, 44*(12), pp.2261-2286.

Le Roex, A. and Class, C., 2016. Metasomatic enrichment of Proterozoic mantle south of the Kaapvaal Craton, South Africa: origin of sinusoidal REE patterns in clinopyroxene and garnet. *Contributions to Mineralogy and Petrology, 171*(2), p.14.

Lewis, H.C., 1887. The matrix of diamond. *Geological Magazine 5*, pp. 129–131.

Luguet, A., Behrens, M., Pearson, D.G., König, S. and Herwartz, D., 2015. Significance of the whole rock Re–Os ages in cryptically and modally metasomatised cratonic peridotites: Constraints from HSE–Se–Te systematics. *Geochimica et Cosmochimica Acta, 164*, pp.441-463.

Mitchell, R.H., 1986. *Kimberlites: Mineralogy, Geochemistry, and Petrology*. Plenum Press, New York. 441 p.

Mitchell, R.H., 1991. Kimberlites and lamproites: Primary sources of diamond. *Geoscience Canada, 18*(1), pp. 1-16.

Mitchell, R.H., 1994. Suggestions for revisions to the terminology of kimberlites and lamprophyres from a genetic viewpoint. In *Proceedings in the. Fifth International Kimberlite Conference* (Vol. 1, pp. 15-26).

Mitchell, R.H., 1995. *Kimberlites, orangeites, and related rocks*. Plenum Press, New York. 410 p.

Muramatsu, Y., 1983. Geochemical investigations of kimberlites from the Kimberley area, South Africa. Geochemical Journal, 17(2), pp.71-86.

Muramatsu, Y. and Wedepohl, K.H., 1985. REE and selected trace elements in kimberlites from the Kimberley area (South Africa). *Chemical Geology, 51*(3-4), pp.289-301.

Myers, J.D., Angevine, C.L. and Frost, C.D., 1987. Mass balance calculations with end member compositional variability: applications to petrologic problems. *Earth and planetary science letters*, 81(2-3), pp.212-220.

Nielsen, T.F., Sand, K.K., 2008. The Majuagaa kimberlite dike, Maniitsoq region, West Greenland: constraints on an Mg-rich silicocarbonatitic melt composition from groundmass mineralogy and bulk compositions. *The Canadian Mineralogist, 46* (4), 1043–1061.

Nowicki, T., Porritt, L., Crawford, B. and Kjarsgaard, B., 2008. Geochemical trends in kimberlites of the Ekati property, Northwest Territories, Canada: insights on volcanic and resedimentation processes. *Journal of Volcanology and Geothermal Research, 174*(1-3), pp.117-127.

Ogilvie-Harris, R.C., Field, M., Sparks, R.S.J. and Walter, M.J., 2009. Perovskite from the Du Toitspan kimberlite, Kimberley, South Africa: implications for magmatic processes. *Mineralogical Magazine, 73*(6), pp.915-928.

Pandey, A., Rao, N.C., Chakrabarti, R., Pandit, D., Pankaj, P., Kumar, A. and Sahoo, S., 2017. Petrogenesis of a Mesoproterozoic shoshonitic lamprophyre dyke from the Wajrakarur kimberlite field, eastern Dharwar craton, southern India: Geochemical and Sr-Nd isotopic evidence for a modified sub-continental lithospheric mantle source. *Lithos, 292*, pp.218-233.

Patterson, M., Francis, D. and McCandless, T., 2009. Kimberlites: magmas or mixtures?. *Lithos, 112*, pp.191-200.

Pilbeam, L.H., Nielsen, T.F.D. and Waight, T.E., 2013. Digestion fractional crystallization (DFC): an important process in the genesis of kimberlites. Evidence from olivine in the Majuagaa kimberlite, southern West Greenland. *Journal of Petrology*, 54(7), pp.1399-1425.

Poujol, M., Anhaeusser, C.R. and Armstrong, R.A., 2002. Episodic granitoid emplacement in the Archaean Amalia–Kraaipan terrane, South Africa: confirmation from single zircon U–Pb geochronology. *Journal of African Earth Sciences, 35*(1), pp.147-161.

Price, S.E., Russell, J.K. and Kopylova, M.G., 2000. Primitive magma from the Jericho Pipe, NWT, Canada: constraints on primary kimberlite melt chemistry. *Journal of Petrology, 41*(6), pp.789-808.

Raczek I., Stoll B., Hofmann A.W. and Jochum K.P. (2001). High-precision trace element data for the USGS reference materials BCR-1, BCR-2, BHVO-1, BHVO-2, AGV-1, AGV-2, DTS-1, DTS-2, GSP-1 and GSP-2 by ID-TIMS and MIC-SSMS. Geostandards Newsletter: *The Journal of Geostandards and Geoanalysis, 25*, pp. 77-86.

Rollinson, H., 1993. Using Geochemical Data: evaluation, presentation, interpretation. *British Library Cataloguing-in-Publication Data*, pp.352.

Roy, P., Balaram, V., Kumar, A., Satyanarayanan, M. and Gnaneshwar Rao, T., 2007. New REE and trace element data on two kimberlitic reference materials by ICP-MS. *Geostandards and Geoanalytical Research, 31*(3), pp.261-273.

Russell, J.K., Porritt, L.A., Lavallée, Y. and Dingwell, D.B., 2012. Kimberlite ascent by assimilation-fuelled buoyancy. *Nature*, 481(7381), pp.352-356.

Safonov, O., Butvina, V. and Limanov, E., 2019. Phlogopite-Forming Reactions as Indicators of Metasomatism in the Lithospheric Mantle. *Minerals, 9*(11), p.685.

Scott-Smith, B.H., Nowicki, T.E., Russell, J.K., Webb, K.J., Mitchell, R.H., Hetman, C.M. and Robey, J.V.A., 2018. A Glossary of kimberlite and related rocks 3 parts. *Scott-Smith Petrology Inc., North Vancouver, Canada,* p. 259.

Stiefenhofer, J., Viljoen, K.S., Marsh, J.S., 1997. Petrology and geochemistry of peridotite xenoliths from the Letlhakane kimberlite, Botswana. *Contributions to Mineralogy and Petrology, 127*, pp.147–158.

Shatskiy, A., Litasov, K.D., Sharygin, I.S. and Ohtani, E., 2017. Composition of primary kimberlite melt in a garnet lherzolite mantle source: constraints from melting phase relations in anhydrous Udachnaya-East kimberlite with variable CO_2 content at 6.5 GPa. *Gondwana Research, 45*, pp.208-227.

Shaw, D.M., 2000. Continuous (dynamic) melting theory revisited. The Canadian Mineralogist, 38(5), pp.1041-1063.

Shaw, D.M., 1970. Trace element fractionation during anatexis. *Geochimica et Cosmochimica Acta, 34*(2), pp.237-243.

Shee, S.R., 1985. The petrogenesis of the Wesselton Mine kimberlites, Kimberley, South Africa. Unpublished Ph.D. thesis, University of Cape Town, Cape Town, 530 pp.

Simon, N.S., Carlson, R.W., Pearson, D.G. and Davies, G.R., 2007. The origin and evolution of the Kaapvaal cratonic lithospheric mantle. *Journal of Petrology, 48*(3), pp.589-625.

Skinner, E.M.W., Clement, C.R., 1979. Mineralogical classification of southern African kimberlites. *Second International Kimberlite Conference,* Santa Fe. American Geophysical Union, pp. 129–139

Skinner, E.M.W., 1989. Contrasting Group 1 and Group 2 kimberlite petrology: towards a genetic model for kimberlites. In: Ross, J., Jacques, A.L., Ferguson, J., Green, D.H., O'Reilly, S.Y., Danchin, R.V., Janse, A.J.A. (Eds.), Kimberlites and Related Rocks, Volume 1. *Proceedings of the Fourth International Kimberlite Conference*. Geological Society of Australia Special Publication 14, Perth, Australia, pp. 528–544.

Skinner, E.M.W., 2008. The emplacement of class 1 kimberlites. *Journal of Volcanology and Geothermal Research*, *174*(1-3), pp.40-48.

Skinner, E.M.W. and Marsh, J.S., 2004. Distinct kimberlite pipe classes with contrasting eruption processes. *Lithos, 76*(1-4), pp.183-200.

Skinner, E.M.W and Truswell, J.F. 2006. Kimberlites. In: Johnson, M.R., Anhaeusser, C.R. & Thomas, R.J. (Eds.) The geology of South Africa, pp. 381-393. Geological Society of South Africa, Marshalltown

Smith, B.S., Nowicki, T.E., Russell, J.K., Webb, K.J., Mitchell, R.H., Hetman, M.H., Skinner, E.M.W. and Robey, J.A., 2012. Kimberlite Terminology and Classification. In *Proceedings of 10th International Kimberlite Conference Volume 2* (p. 1).

Smith, B.S., Nowicki, T.E., Russell, J.K., Webb, K.J., Hetman, C.M., Harder, M. and Mitchell, R.H., 2008, October. Kimberlites: descriptive geological nomenclature and classification. In *International Kimberlite Conference: Extended Abstracts* (Vol. 9).

Smith, C.B., Gurney, J.J., Ebrahim, N., Skinner, E.M.W. and Clement, C.R., 1985. Geochemical character of southern African kimberlites: a new approach based on isotopic constraints. *Transactions of the Geological Society of South Africa, 88*(2), pp.267-280.

Smith., 1983. Pb, Sr and Nd isotopic evidence for sources of southern African Cretaceous kimberlites. *Nature, 304*(5921), p.51.

Soltys, A., Giuliani, A. and Phillips, D., 2018. A new approach to reconstructing the composition and evolution of kimberlite melts: a case study of the archetypal Bultfontein kimberlite (Kimberley, South Africa). *Lithos, 304*, pp.1-15.

Späth, A., Le Roex, A.P. and Opiyo-Akech, N., 2001. Plume–lithosphere interaction and the origin of continental rift-related alkaline volcanism—the Chyulu Hills volcanic province, southern Kenya. *Journal of Petrology, 42*(4), pp.765-787.

Sparks, R.S.J., Baker, L., Brown, R.J., Field, M., Schumacher, J., Stripp, G. and Walters, A., 2006. Dynamical constraints on kimberlite volcanism. *Journal of Volcanology and Geothermal Research, 155*(1-2), pp.18-48.

Sun, S.S. and McDonough, W.F., 1989. Chemical and isotopic systematics of oceanic basalts: implications for mantle composition and processes. *Geological Society, London, Special Publications, 42*(1), pp.313-345.

Stone, R.S. and Luth, R.W., 2016. Orthopyroxene survival in deep carbonatite melts: implications for kimberlites. *Contributions to Mineralogy and Petrology, 171*(7), p.63.

Stripp, G.R., Field, M., Schumacher, J.C., Sparks, R.S.J., Cressy, G., 2006. Post emplacement serpentinization and related hydrothermal metamorphism in kimberlite from Venetia, South Africa. *Journal of Metamorphic Geology ,24,* pp.515–534.

Tainton, K.M. and McKenzie, D.A.N., 1994. The generation of kimberlites, lamproites, and their source rocks. *Journal of Petrology, 35*(3), pp.787-817.

Taylor, W.R., T ins, L.A. and Haggerty, S.E., 1994. Comparative geochemistry of West African kimberlites: evidence for a micaceous kimberlite endmember of sublithospheric origin. *Geochimica et Cosmochimica acta, 58*(19), pp.4017-4037.

Ulmer, P. and Sweeney, R.J., 2002. Generation and differentiation of group II kimberlites: constraints from a high-pressure experimental study to 10 GPa. *Geochimica et Cosmochimica Acta, 66*(12), pp.2139-2153.

Van Achterbergh, E., Griffin, W. L. and Stiefenhofer, J. (2001). Metasomatism in mantle xenoliths from the Letlhakane kimberlites: estimation of element fluxes. *Contributions to Mineralogy and Petrology 141*, 397–414.

Wagner, P.A., 1914. The diamond fields of South Africa. *Transvaal Leader*, Johannesburg. 347 pp.

Wedepohl, K. H., and Y. Muramatsu. The chemical composition of kimberlites compared with the average composition of three basaltic magma types. *Kimberlites, Diatremes, and Diamonds: Their Geology, Petrology, and Geochemistry 15* (1982): 300-312.

Wilson, M., 1989. Igneous petrogenesis. Unwin Hyman. London, 466 p.

Woolley, A.R., Bergman, S.C., Edgar, A.D., Le Bas, M.J., Mitchell, R.H., Rock, N.M. and Scott Smith, B.H., 1996. Classification of lamprophyres, lamproites, kimberlites, and the kalsilitic, melilitic, and leucitic rocks. *The Canadian Mineralogist, 34*(2), pp.175-186.

Wyllie, P.J., 1978. Peridotite-CO_2-H_2O and the low-velocity zone. *Bulletin of Volcanology, 41*(4), pp.670-683.

Zou, H., 1998. Trace element fractionation during modal and nonmodal dynamic melting and open system melting: a mathematical treatment. *Geochimica et Cosmochimica Acta, 62*(11), pp.1937-1945.

APPENDICIES

APPENDIX A : GEOLOGICAL LOGS

DTP880/EX/DDH001				
From	**To**	**LOG**	**PHASE**	**Lithological description**
0.00	52.30			Wall rock – granite gneiss intercalated with subordinate amphibolitic gneiss crosscut by minor pegmatite veins.
52.30	77.20		D11	Grey macrocrystic massive volcaniclastic pyroclastic kimberlite. Contains rare peridotite xenoliths, and crustal xenoliths of dolerite and Archean basement lithologies. Magmaclasts are common. This unit hosts a 26cm aphanitic dyke at 61.30m, and. two macrocrystic hypabyssal kimberlite dykes at 69.35(19cm in length) and at 75.21 (30cm in length).
77.20	91.30		D13	Black macrocrystic hypabyssal kimberlite. Contains abundant Karoo shale xenoliths and lesser Ventersdorp Lava (Andesitic), with rare peridotite mantle xenoliths.
91.30	97.50		D14	Black macrocrystic hypabyssal kimberlite with fresh olivines and few.
97.50	104.83		D11	Grey macrocrystic volcaniclastic pyroclastic kimberlite (similar to unit above)
104.83	109.32		D14	Black macrocrystic hypabyssal kimberlite with fresh olivines and few.
109.32	120.00		D11	Grey macrocrystic volcaniclastic pyroclastic kimberlite (similar to unit above)
120.00	122.00		D13	Black macrocrystic hypabyssal kimberlite (similar to unit above)

DTP880/EX/DDH002				
From	To	LOG	PHASE	Lithological description
0.00	47.64			Amphibolitic Gneiss
47.64	107.19		D11	Grey macrocrystic massive volcaniclastic kimberlite with rare peridotite xenoliths and crustal xenoliths consisting mainly of dolerite and Archean basement lithologies. Magmaclasts are common.
107.19	107.43			Macrocrystic kimberlite dyke
107.43	151.32		D11	Similar D11 unit above
151.32	151.44			Macrocrystic kimberlite dyke
151.44	163.00		D11	Similar D11 unit above

DTP880/EX/DDH006				
From	To	LOG	PHASE	Lithological description
0.00	67.80			Wall rock - amphibolitic gneiss with quartz veins
67.80	80.70		D17	A Hkt (Hypabyssal kimberlite transitioning to pyroclastic kimberlite) rock. The Hkt has a brown relatively fine-grained matrix and overall looks finer grained than the D11.

				Pyroclastic kimberlite. Magmaclasts are distinctive and basement crustal xenolith and black shales.
80.70	91.10		D14	A very fresh, black, hard, macrocrystic hypabyssal kimberlite with a lower content of crustal xenoliths.
91.10	108,04			Wall rock - amphibolitic gneiss with quartz veins

DDH880/EX/DDH007				
From	To	LOG	PHASE	Lithological description
0	33.4			Wall rock - amphibolitic gneiss with quartz veins
33.4	35.91		D11	A dark brown pyroclastic kimberlite
35.91	36.61			Aphanitic hypabyssal kimberlite dyke
36.61	45.94		D11	Brown Pyroclastic kimberlite similar to that above. Olivines are up to 20mm in size and totally altered to a brown colour.
45.94	61.8		D14	Black, hard, very fresh, macrocrystic hypabyssal kimberlite with low abundance in crustal xenoliths up to 6cm in size.
61.8	77		D11	Brown to grey pyroclastic kimberlite with abundant crustal xenoliths ranging from 1-3cm in size. The pyroclastic kimberlite turns brownish-pinkish colour 71m to 77m.
77	87.54		D13	Hard, black, macrocrystic CK with common, very altered white basement crustal xenoliths up to 10cm in size.
87.54	102		D11	Brown to grey pyroclastic kimberlite.
102	102.72			Aphanitic hypabyssal kimberlite dyke
102.72	103.2		D11	similar to unit above
103.2	103.44			Aphanitic hypabyssal kimberlite dyke
103.44	103.72		D11	similar to unit above
103.72	104.3		D13	Similar to unit above

DDH880/EX/DDH011				
From	To	LOG	PHASE	Lithological description
0	51.2			Wall rock - amphibolitic gneiss with quartz veins
51.2	61.1	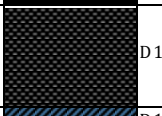	D11	Greyish brown pyroclastic kimberlite. Crustal xenoliths are common and up to 16cm in size (dolerite) and Archean basement crustal xenoliths . This unit is intruded by a 6cm wide fine-grained hypabyssal kimberlite dyke at 51,4m.
61.1	63.8		D14	Black, very fresh, macrocrystic hypabyssal kimberlite.
63.8	82.2		D13	Black, fresh, macrocrystic hypabyssal kimberlite fresh and with common Archean basement crustal xenoliths. So here we can see the contact between two different hypabyssal kimberlites - one very fresh and with few crustal xenoliths (D14) and the other fresh with common very altered white Archean basement crustal xenoliths.
82.2	121,8		D17	Brown HKt (hypabyssal kimberlite transitioning to a pyroclastic kimberlite) with magmaclasts and altered olivines up to 10mm in size. Crustal xenoliths are relatively unaltered and can be large. Between 97,8 and 100,2 there is a 2,4m sized Karoo Beaufort Group siltstone xenolith and between 118,6 and 120,5m a large basement schist xenolith. This unit is intruded by aphanitic hypabyssal dykes from (115 – 116.2m) and (116.7 - 117m.) The latter dyke hosts a 5cm unaltered harzburgite mantle xenolith

DDH880/EX/DDH012				
From	To	LOG	PHASE	Lithological description
0	31.8			Wall rock - amphibolitic gneiss with quartz veins
31.8	35.45		D11	A grey brown pyroclastic kimberlite with common unaltered crustal xenolith up to 20mm in size. Magmaclasts are common.

35.45	82.8		D14	Black, very fresh hypabyssal kimberlite (HK) similar to the low crustal xenolith HK described in boreholes cores.
82.8	86.8		D11	Normal grey brown PYROCLASTIC KIMBERLITE
86.8	87.8			Fine grained HK dyke, black (D11)
87.8	89.16		D11	Grey pyroclastic kimberlite
89.16	98.8			Wall rock schist with stringers of brown HK at 97,3 and 98,8m.
98.8	103.8			Wall rock amphibolitic gneiss
103.8	106.8	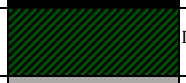	D13	Altered and brown kimberlite that is rich in crustal xenoliths (~40%) mainly of altered basement lithologies
106.8	140.80			Wall rock - schist intruded by an aphanitic kimberlite dyke and a macrocrystic dyke

DDH880/EX/DDH013				
From	To	LOG	PHASE	Lithological description
0	89.69			Amphibolitic Gneiss with quartz veins
89.69	97.65		D14	Macrocrystic hypabyssal kimberlite with fresh olvines low abundance in crustal xenoliths (<10%).
97.65	103.8		D17	A hypabyssal kimberlite transitioning into a pyroclastic kimberlite (Hkt). Olivines are altered to a brownish green colour. Crustal xenoliths are up to 5cm are abundant with common andesitic lava up 6cm. Magmaclasts are seen.

DDH880/EX/DDH014				
From	To	LOG	PHASE	Lithological description
0	38.85			Granite - Gneiss intercalated with sub-ordinate amphibolitic gneiss with regularly occurring pegmatite and quartz veins
38.85	97.76		D14	Macrocrystic hypabyssal kimberlite with fresh olvines low abundance in crustal xenoliths of mostly schist and granite up to 14cm and 12cm, respectively.
97.76	98.08			Aphanitic hypabyssal kimberlite dyke
98.08	99.96		D14	Black hypabyssal kimberlite (D14)
99.96	107.28		D11	Grey pyroclastic kimberlite.
107.28	110.47		D14	Macrocrystic hypabyssal kimberlite hosting an autolith between 109.51m - 109.83m
110.47	132.88		D11	Grey pyroclastic kimberlite.
132.88	161.00			Wall rock schist – This unit is intruded by two aphanitic kimberlite dykes from 142.75m -142.77m and 144.55m-146.00m

DDH880/EX/DDH015				
From	To	LOG	PHASE	Lithological description
0.00	34.00			Wall rock – Basement gneiss and amphibolite with later quartz veins.
34.00	34.75		D11	Brown pyroclastic kimberlite with MARID xenoliths up to 3cm is size. Olivines are altered (black) and are up to 10mm in size. magmaclasts are present.
34.75	35.36			Aphanitic hypabyssal kimberlite dyke
35.36	38.77		D11	Brown pyroclastic kimberlite with magmaclasts up to 3cm. crustal xenoliths include basement lithologies and black shale. Also present are mantle xenolith up to 4 cm peridotite
38.77	38.92			Aphanitic hypabyssal kimberlite dyke, aphanitic, mantle peridotite xenolith that is 8cm in size
38.92	48.18		D11	Brown pyroclastic kimberlite with magmaclasts and large black altered olivines up to 10mm. crustal xenoliths including andesitic lavas up to 14cm, basement lithologies up to 5cm,
48.18	48.95			Macrocrystic hypabyssal kimberlite

48.95	56.29		D11	Similar to unit above
56.29	57.23			Aphanitic hypabyssal kimberlite
57.23	61.77		D11	Brown pyroclastic kimberlite with crustal xenoliths of schist (up to 30cm), Andesitic lava (up to 35cm
61.77	65.96		D13	Macrocrystic hypabyssal kimberlite with crustal xenoliths up to 15cm . and smaller ~2cm basement lithologies crustal xenoliths are common
65.96	75.08		D11	Similar to unit above
75.08	83.42		D13	Similar to unit above
83.42	86.10		D11	Similar to unit above
86.10	87.30		D13	Similar to unit above
87.30	89.35		D11	Similar to unit above
89.35	90.29		D13	Similar to unit above
90.29	91.80		D11	Similar to unit above
91.80	116.70		D14	Moderately macrocrystic hypabyssal kimberlite, with low abundances of crustal xenolith, largest crustal is 2cm.
116.70	117.45		D11	Grey brown pyroclastic kimberlite
117.45	147.40	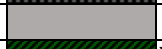		Wall rock- with kimberlite stringers
147.40	147.92	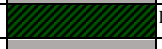	D13	Macrocrystic hypabyssal kimberlite with coarse olivines.
147.92	163.00	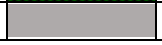		Wall rock - schist with some quartz veins.

DDH880/EX/DDH016				
From	To	LOG	PHASE	Lithological Description
0.00	40.55			Wall rock – Basement gneiss and amphibolite with later quartz vein.
40.55	51.15		D11	Brown pyroclastic becomes darker and starts looking like a hypabyssal kimberlite from ~46m onwards but still has magmaclasts.
51.15	62.05		D14	Macrocrystic hypabyssal kimberlite with crustal xenoliths of mostly Ventersdorp lava up to 3cm in size.
62.05	76.82		D17	Greenish brown pyroclastic kimberlite (from 62 - 68m kimberlite is transitional from pyroclastic to hypabyssal kimberlite).
76.82	77.05			Macrocrystic hypabyssal kimberlite dyke
77.05	86.34		D11	Grey – brown pyroclastic kimberlite with abundant basement and shale crustal xenoliths up to 4cm in size. Olivines are black altered and up to 10mm in size. Magmaclasts present and present but rare.
86.34	86.90			Hypabyssal macrocrystic dyke (similar to unit above)
86.90	93.41		D11	Grey – brown pyroclastic kimberlite.
93.41	101.05			Wall rock – Schist with some quartz veins.

APPENDIX B: PETROGRAPHY OF INDIVIDUAL SAMPLES

B.1. D13 – phlogopite kimberlite

	Kimberlite		Macrocrysts (modal%)		Phenocrysts (modal%)		Groundmass (modal%)
Sample	DDH-001-3		Olivine (23%) – anhedral serpentinized along margins and fractures		Olivine (15%) - subhedral, partially to completely serpentinized		Phlogopite (20%)- Interlocking laths
Phase	D13		Phlogopite (5%) – anhedral		Phlogopite (3%) - subhedral and lath- shaped		Monticellite (8%) – granular, occasionally serpentinized
Mineralogical classification	Phlogopite kimberlite		Ilmenite (2%) – anhedral				Opaque oxides (7%) - euhedral to subhedral
Textural classification	Uniformly textured macrocrystic						Perovskite (7%) - euhedral to subhedral
							Serpentine (5%) - Interstitial
							Calcite (5%)- Interstitial
Sample	DDH-007-3		Olivine (27%) - anhedral, serpentinized along margins and fractures, deformation textures		Olivine (17%) - subhedral to euhedral, partially to completely serpentinized		Phlogopite (15%)- Interstitial laths
Phase	D13		Phlogopite (3%) - anhedral		Phlogopite (3%) - subhedral and lath-shaped; serpentinized		Monticellite (10%) – granular, occasionally serpentinized
Mineralogical classification	Monticellite phlogopite kimberlite		Ilmenite (3%) - anhedral				Opaque oxides (7%) - euhedral to subhedral
Textural classification	Uniformly textured macrocrystic						Perovskite (5%) - euhedral to subhedral
							Serpentine (5%) - Interstitial
							Calcite (5%)- Interstitial
Sample	DDH-008-3		Olivine (25%)-anhedral, serpentinized along margins and fractures, deformation textures		Olivine (15%) - subhedral to euhedral, partially to completely serpentinized		Phlogopite (20%)- Interstitial laths
Phase	D13		Phlogopite (6%) - anhedral		Phlogopite (3%) - subhedral and lath- shaped; serpentinized		Monticellite (10%) – granular, occasionally serpentinized
Mineralogical classification	Phlogopite kimberlite		Ilmenite (3%) - anhedral		Ilmenite (2%) - anhedral		Opaque oxides (6%) - euhedral to subhedral
Textural classification	Uniformly textured macrocrystic						Perovskite (5%) - euhedral to subhedral
							Serpentine (5%) - Interstitial

							Calcite (5%)- Interstitial

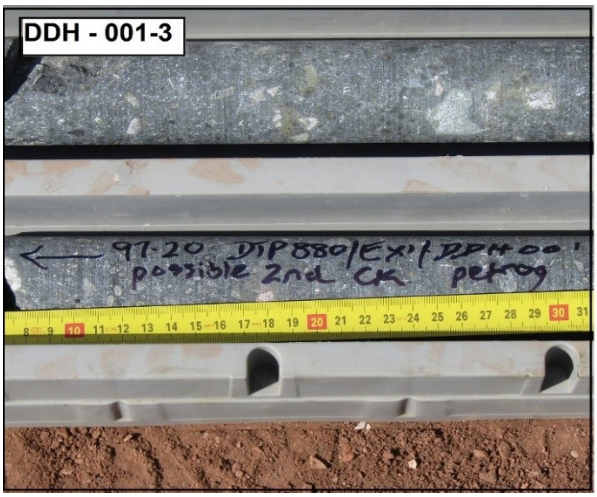

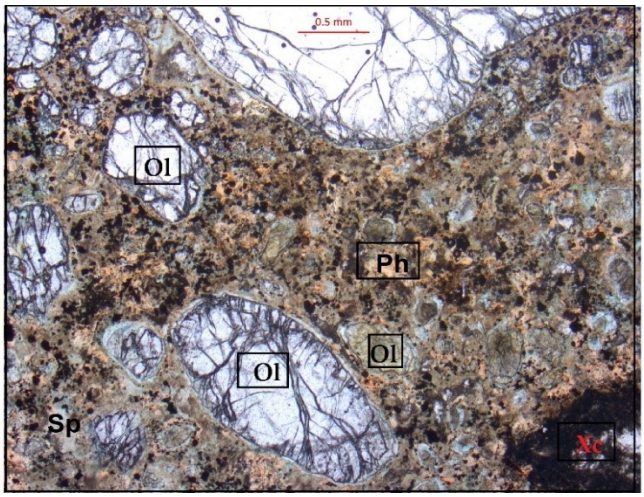

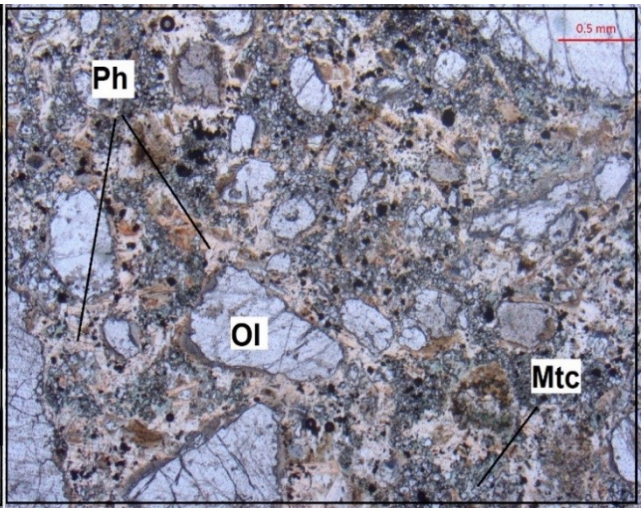

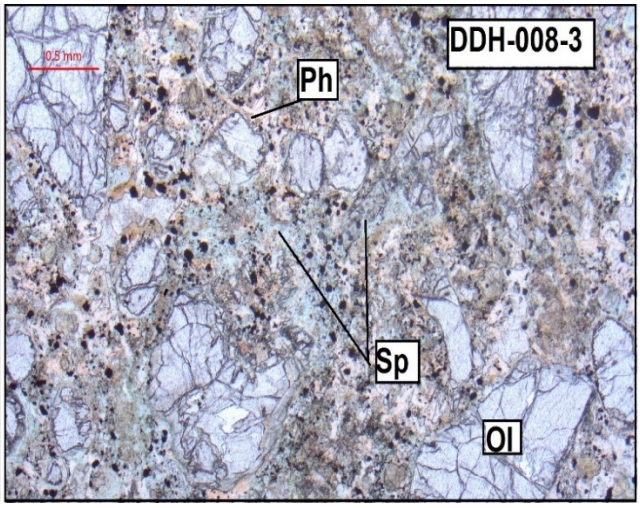

B.2 D14 – monticellite kimberlite

	Kimberlite		Macrocrysts		Phenocrysts		Groundmass
Sample	DDH-006-3		Olivine (10%)-anhedral, serpentinized along margins and fractures, deformation features		Olivine (25%) - subhedral to euhedral, , partially to completely serpentinized		Monticellite (20%)- granular, ultrafine (< 0.125 mm)
Phase	D14		Phlogopite (3%) – anhedral, partially to completely resorbed.		Phlogopite (7%) - subhedral and lath-shaped; completely or partially resorbed		Calcite (15%) - Interstitial and tabular discrete grains
Mineralogical classification	Monticellite kimberlite						Opaque oxides (10%) - euhedral to subhedral
Textural classification	Uniformly textured, sparsely macrocrystic						Perovskite (5%) - Euhedral to subhedral
							Phlogopite (5%) – typically resorbed
Sample	DDH-007-1		Olivine (20%)-anhedral, serpentinized along margins and fractures, deformation textures		Olivine (20%) - subhedral to euhedral, partially to completely serpentinized		Monticellite (20%)- granular, ultrafine (< 0.125 mm)
Phase	D14		Phlogopite (3%) – anhedral, partially to completely resorbed.		Phlogopite (2%) - subhedral and lath-shaped; completely or partially resorbed		Calcite (12%) - Interstitial and tabular discrete grains
Mineralogical classification	Monticellite kimberlite						Opaque oxides (8%) - euhedral to subhedral
Textural classification	Uniformly textured macrocrystic						Perovskite (7%) - Euhedral to subhedral
							Phlogopite (5%) - Interstitial
							Apatite (3%) - acicular
Sample	DDH-0011-2		Olivine (20%)-anhedral, serpentinized along margins and fractures, deformation textures		Olivine (20%) - subhedral to euhedral, partially to completely serpentinized		Monticellite (20%)- granular ultrafine (< 0.125 mm)
Phase	D14		Phlogopite (3%) – anhedral, partially to completely resorbed		Phlogopite (3%) - subhedral and lath-shaped; completely or partially resorbed		Calcite (12%) - Interstitial and tabular discrete grains
Mineralogical classification	Monticellite kimberlite						Opaque oxides (10%) - euhedral to subhedral
Textural classification	Uniformly textured macrocrystic						Perovskite (5%) - Euhedral to subhedral
							Phlogopite (5%) - typically resorbed
Sample	DDH-014-4		Olivine (35%)-anhedral, serpentinized along margins and fractures, deformation textures		Olivine (12%) - subhedral to euhedral, partially to completely serpentinized		Monticellite (15%)- granular, ultrafine (< 0.125 mm)

Phase	D14		Phlogopite (5%) – anhedral, partially to completely resorbed		Phlogopite (3%) - subhedral and lath-shaped; completely or partially resorbed		Calcite (10%) - Interstitial and tabular discrete grains
Mineralogical classification	Monticellite kimberlite						Opaque oxides (7%) - euhedral to subhedral
Textural classification	Uniformly textured macrocrystic						Perovskite (5%) - Euhedral to subhedral
							Serpentine (5%)- interstitial
							Apatite (3%) - acicular
Sample	DDH-015-5		Olivine (12%)-anhedral, serpentinized along margins and fractures, deformation textures		Olivine (15%) - subhedral to euhedral, partially to completely serpentinized		Monticellite (25%)- granular, ultrafine (< 0.125 mm)
Phase	D14		Phlogopite (5%) – anhedral, partially to completely resorbed		Phlogopite (3%) - subhedral and lath-shaped; completely or partially resorbed		Calcite (15%) - Interstitial and tabular discrete grains
Mineralogical classification	Monticellite kimberlite						Opaque oxides (10%) - euhedral to subhedral
Textural classification	Uniformly textured macrocrystic						Perovskite (10%) - Euhedral to subhedral
							Serpentine (5%)- interstitial
Sample	DDH-016-3		Olivine (16%)-anhedral, serpentinized along margins and fractures, deformation textures		Olivine (20%) - subhedral to euhedral, partially to completely serpentinized		Monticellite (20%)- granular ultrafine (< 0.125 mm)
Phase	D14		Phlogopite (5%) – anhedral, partially to completely resorbed		Phlogopite (3%) - subhedral and lath-shaped; completely or partially resorbed		Calcite (13%) - Interstitial and tabular discrete grains
Mineralogical classification	Monticellite kimberlite						Opaque oxides (8%) - euhedral to subhedral
Textural classification	Uniformly textured macrocrystic						Perovskite (7%) - euhedral to subhedral
							Serpentine (5%)- interstitial
							Apatite (3%) - acicular
Sample	DDH-016-4		Olivine (25%)-anhedral, serpentinized along margins and fractures, deformation textures		Olivine (15%) - subhedral to euhedral, partially to completely serpentinized		Monticellite (15%)- granular ultrafine (< 0.125 mm)
Phase	D14		Phlogopite (10%) – anhedral, partially to completely resorbed		Phlogopite (5%) - subhedral and lath-shaped; completely or partially resorbed		Calcite (10%) - Interstitial and tabular discrete grains
Mineralogical classification	Monticellite kimberlite						Opaque oxides (8%) - euhedral to subhedral
Textural classification	Uniformly textured macrocrystic						Perovskite (8%) - euhedral to subhedral

							Phlogopite (4%) - typically resorbed

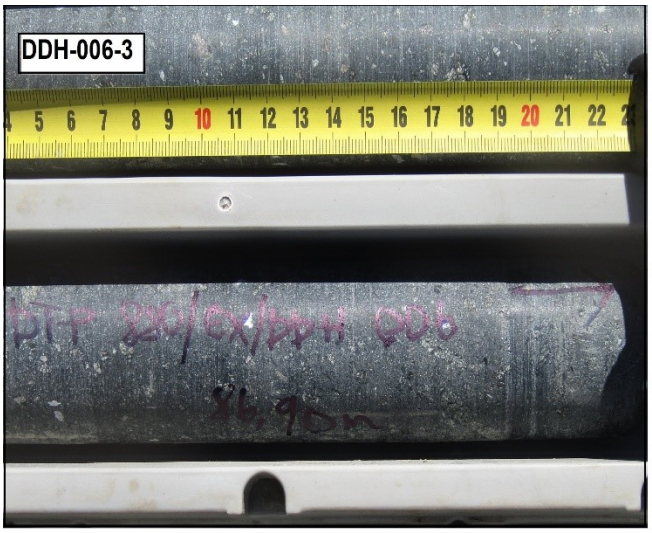

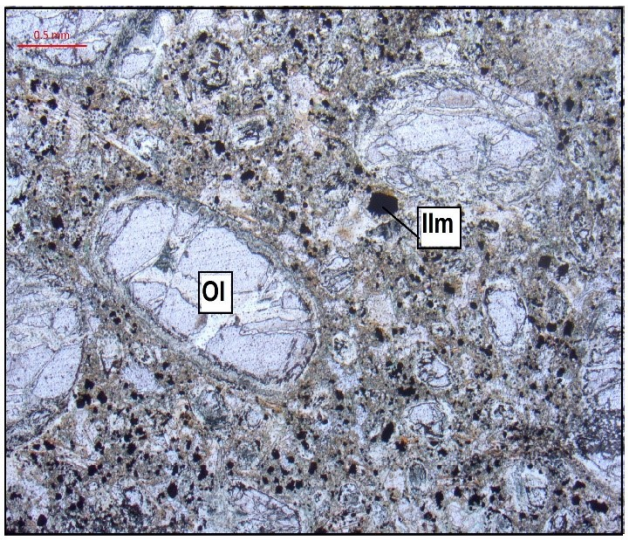

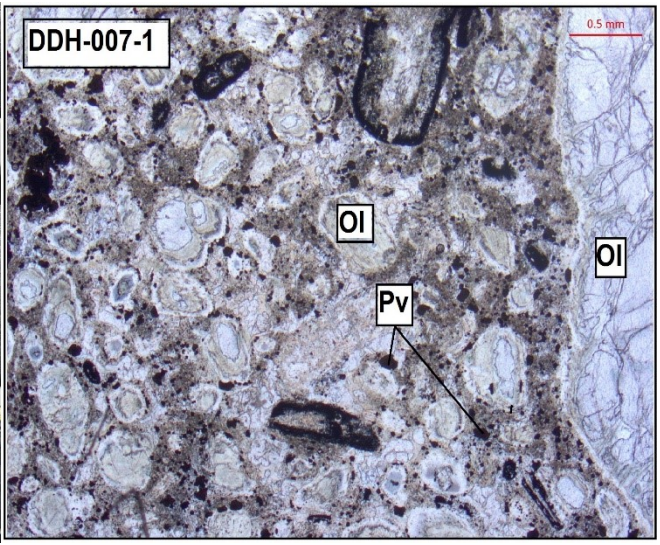


DDH-011-2

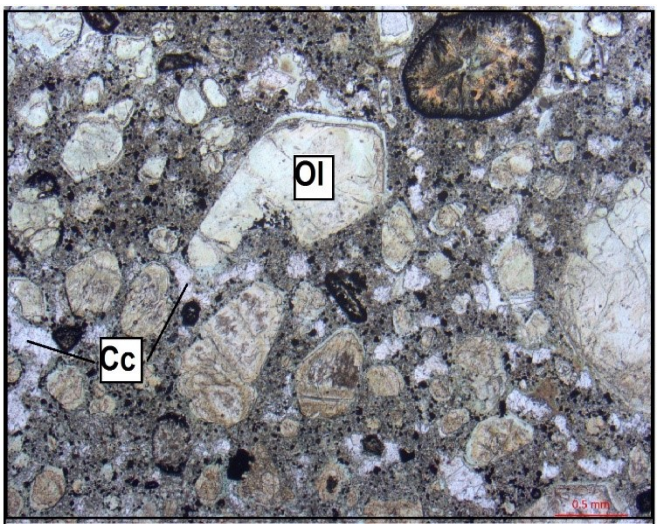
Ol
Cc
0.5 mm


DDH-014-4
DEPTH
10700

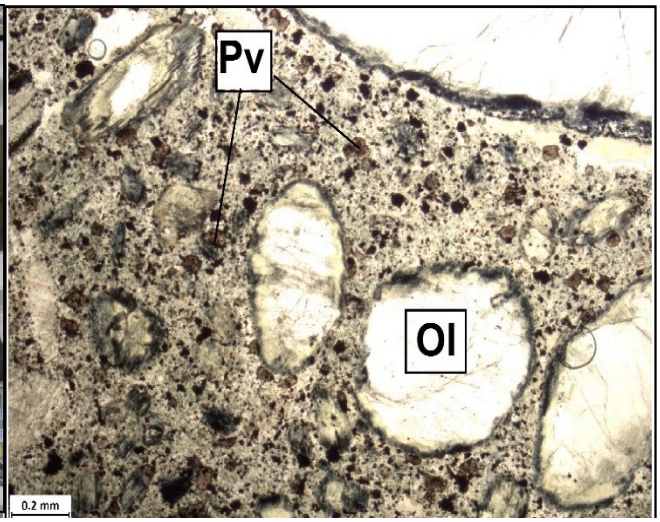
Pv
Ol
0.2 mm


DDH-015-5

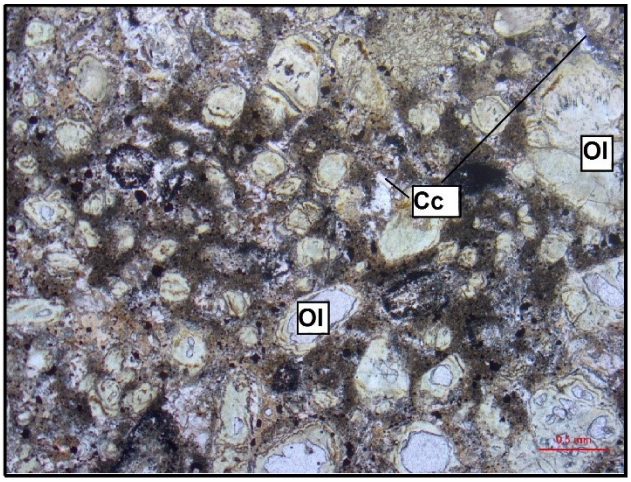
Ol
Cc
Ol

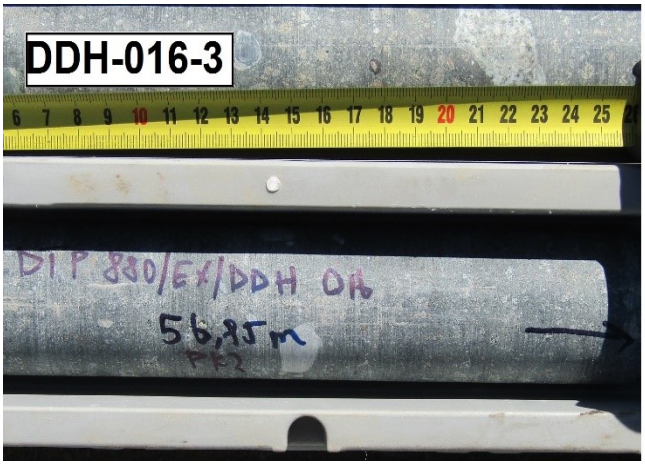
DDH-016-3

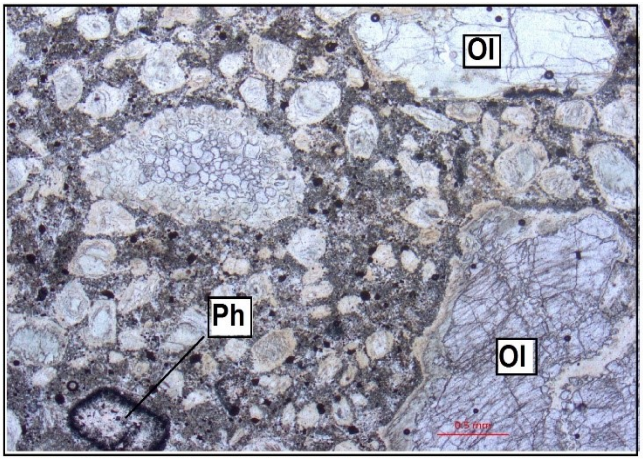
Ol
Ph
Ol

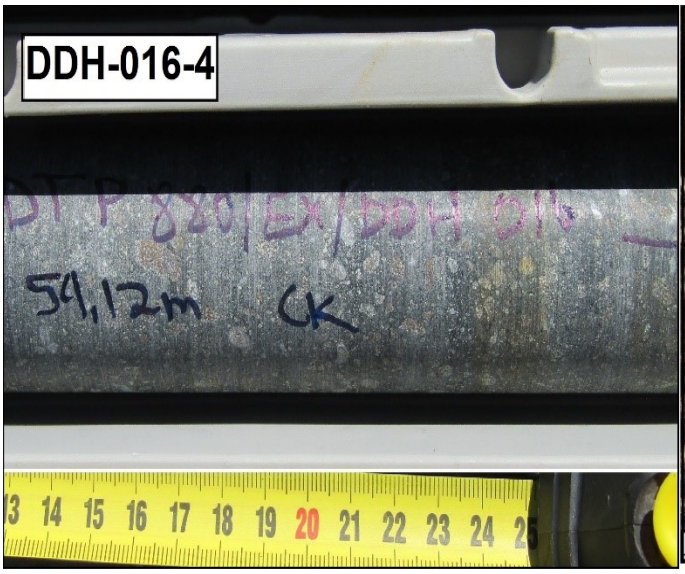
DDH-016-4

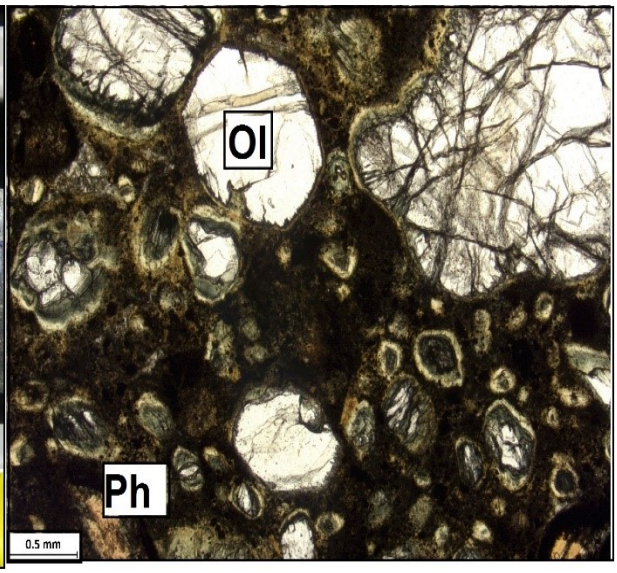
Ol
Ph
0.5 mm

B.3. D17 – serpentinized phlogopite kimberlite

	Kimberlite		Macrocrysts (modal%)		Phenocrysts (modal%)		Groundmass (modal%)
Sample	DDH-006-1		Olivine (28%)-anhedral, serpentinized, deformation features		Olivine (14%) - subhedral to euhedral, completely serpentinized		Phlogopite (10%)- subhedral to lath – shaped, serpentinized
Phase	D17		Phlogopite (10%) - subhedral, compositionally zoned,		Phlogopite (8%) - subhedral and lath- shaped; serpentinized		Serpentine (8%) - Interstitial
Mineralogical classification	Serpentinized phlogopite kimberlite		Amphibole (< 7%) – crustal xenocrysts, euhedral				Calcite (7%) - Interstitial to tabular
Textural classification	Uniform, macrocrystic						Opaque - oxides(3%) - euhedral to subhedral
							Perovskite (3%) - euhedral to subhedral
							Microlitic diopside (2%)
Sample	DDH-006-2		Olivine (30%)-anhedral, serpentinized, deformation features		Olivine (15%) - subhedral to euhedral, completely serpentinized		Phlogopite (15%)- subhedral to lath – shaped, serpentinized
Phase	D17		Phlogopite (5%) - subhedral, compositionally zoned,		Phlogopite (5%) - subhedral and lath- shaped; serpentinized		Serpentine (8%) - interstitial
Mineralogical classification	Serpentinized phlogopite kimberlite		Amphibole (< 7%) – crustal xenocrysts, euhedral				Calcite (7%) - interstitial to tabular
Textural classification	Uniform,						Opaque - oxides(3%) - euhedral to subhedral
	macrocrystic						Perovskite (3%) - euhedral to subhedral
							Microlitic diopside (2%)
Sample	DDH-0011-4		Olivine (25%)-anhedral, serpentinized along margins and fractures, deformation textures		Olivine (15%) - subhedral to euhedral, completely serpentinized		Phlogopite (18%)- Brown, interlocking laths, serpentinized
Phase	D17		Phlogopite (6%) - anhedral		Phlogopite (4%) - subhedral and lath- shaped; serpentinized		Serpentine (12%) - Interstitial
Mineralogical classification	Serpentinized phlogopite kimberlite						Calcite (10%) - Interstitial to tabular
	Segregationary,						Opaque - oxides (5%) - euhedral to subhedral
	macrocrystic						Perovskite (3%) - euhedral to subhedral
							Microlitic diopside (2%)
Sample	DDH-013-4		Olivine (24%)-anhedral, serpentinized along margins and fractures, deformation textures		Olivine (15%) - subhedral to euhedral, completely serpentinized		Phlogopite (25%)- Brown, interlocking laths, serpentinized

Phase	D17		Phlogopite (6%) - anhedral serpentinized		Phlogopite (8%) - subhedral and lath- shaped; serpentinized		Serpentine (8%) - Interstitial
Mineralogical classification	Serpentinized phlogopite kimberlite						Calcite (7%) - Interstitial to tabular
Textural classification	Segregationary,						Opaque - oxides (3%) - euhedral to subhedral
	macrocrystic						Perovskite (2%) - euhedral to subhedral
							Microlitic diopside (2%)
Sample	DDH-016-5		Olivine (23%)-anhedral, serpentinized along margins and fractures, deformation textures		Olivine (15%) - subhedral to euhedral, partially to completely serpentinized		Phlogopite (20%)- Brown, subhedral to euhedral, serpentinized
Phase	D17		Phlogopite (7%) – anhedral, serpentinized		Phlogopite (8%) - subhedral and lath- shaped; serpentinized		Serpentine (10%) – Interstitial
Mineralogical classification	Serpentinized phlogopite kimberlite						Calcite (10%) – Interstitial to tabular
Textural classification	Segregationary,						Opaque - oxides (3%) - euhedral to subhedral
	macrocrystic						Perovskite (2%) - euhedral to subhedral
							Microlitic diopside (<2%)

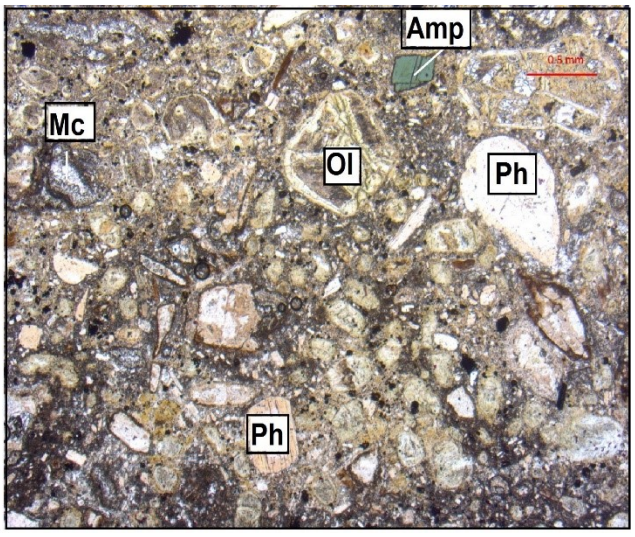

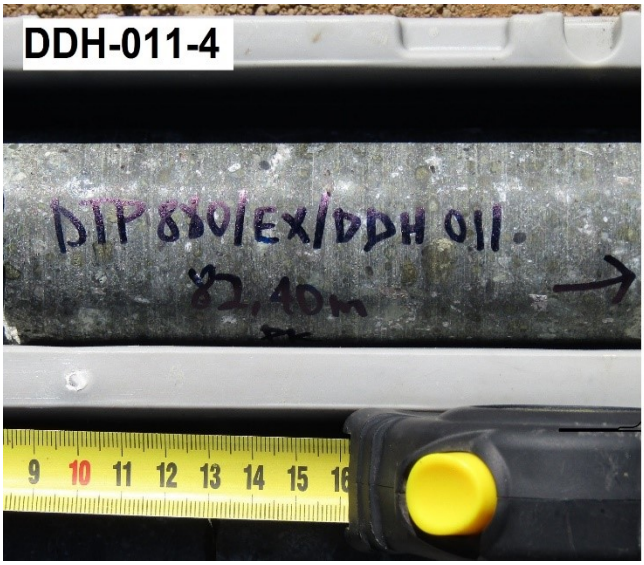
DDH-011-4

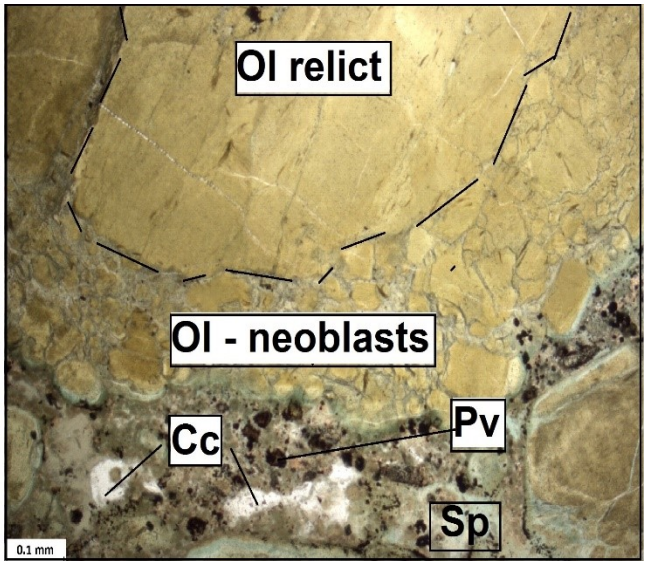
Ol relict
Ol - neoblasts
Cc
Pv
Sp
0.1 mm


DDH-006-2

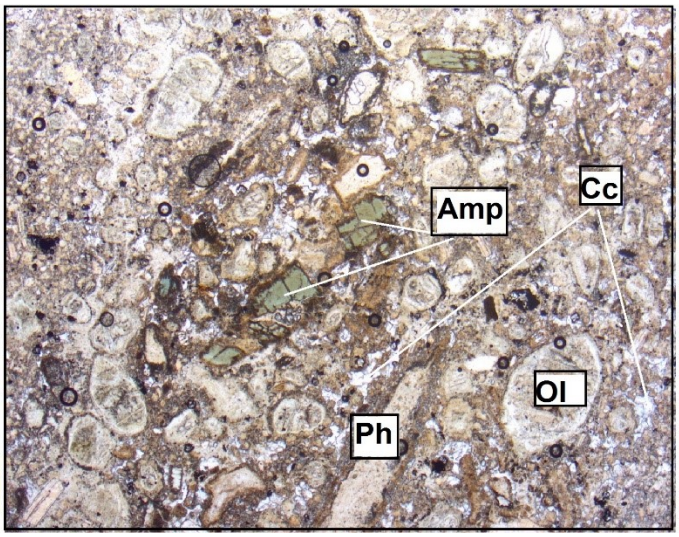
Amp
Cc
Ol
Ph

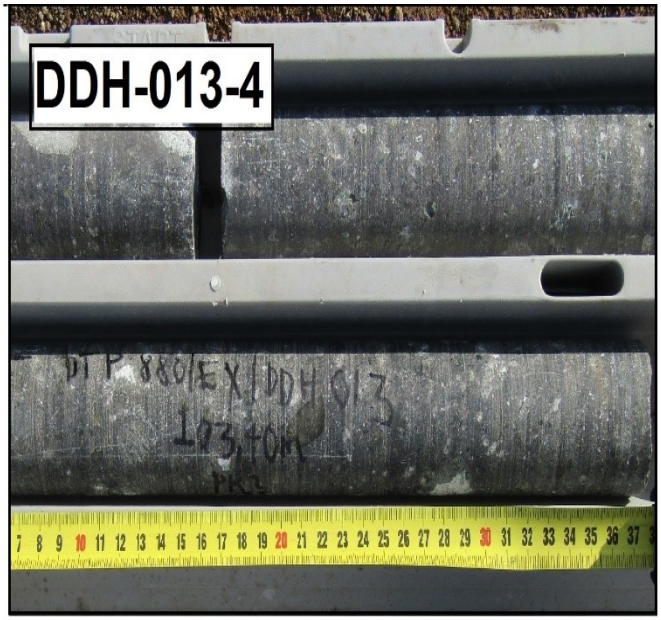
DDH-013-4

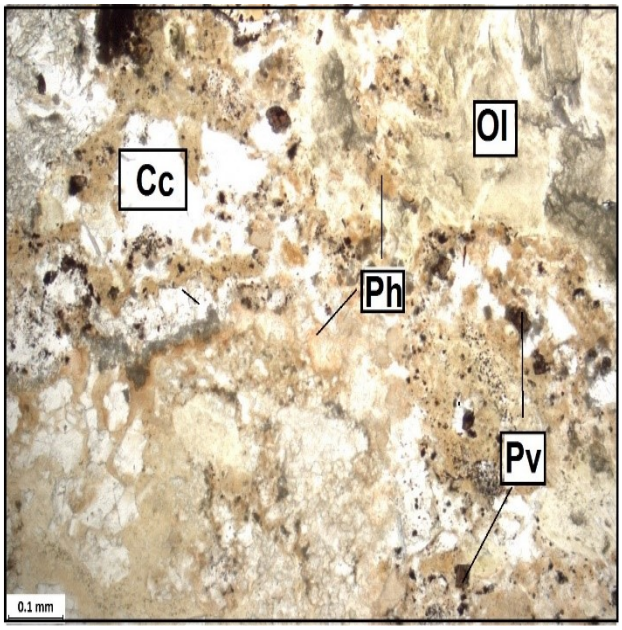
Ol
Cc
Ph
Pv
0.1 mm

B.4. Macrocrystic calcite kimberlite

	Kimberlite		Macrocrysts (modal%)		Phenocrysts (modal%)		Groundmass (modal%)
Sample	DDH-002-4		*Olivine* (39%)-anhedral, serpentinized along margins and fractures, deformation features		*Olivine* (15%) - subhedral to euhedral, partially to completely serpentinized		*Calcite* (15%)- laths in a sheaf texture
Phase	Internal dyke		*Phlogopite* (5%) - anhedral		*Phlogopite* (5%) - subhedral and poikilitic		*Opaque oxides* (10%) - euhedral to subhedral
Mineralogical classification	Calcite kimberlite		*Garnet* (<1%) – anhedral, kelyphitized				*Perovskite* (8%) - euhedral to subhedral
Textural classification	Uniform, very macrocrystic						*Monticellite* (5%) – granular, carbonatized
							Phlogopite (3%) – *laths*
							Serpentine (2%)- Interstitial and tabular
							Apatite (2%) - acicular
Sample	DDH-011-7		*Olivine* (10%)-anhedral, serpentinized along margins and fractures, deformation textures		*Olivine* (17%) - subhedral to euhedral, partially to completely serpentinized		*Calcite* (20%)- laths in a sheaf texture
Phase	Internal dyke		*Phlogopite* (8%) - anhedral		*Phlogopite* (8%) - subhedral and poikilitic		*Opaque oxides* (10%) - euhedral to subhedral
Mineralogical classification	Calcite kimberlite		*Garnet* (<2%) - anhedral, kelyphitized				*Perovskite* (8%) - euhedral to subhedral
Textural classification	Uniform, sparsely macrocrystic						*Monticellite* (7%) – granular, carbonatized
							Serpentine (5%)- Interstitial
							Phlogopite (3%) – *laths*
							Apatite (2%) - acicular
Sample	DDH-0013-2		*Olivine* (15%)-anhedral, serpentinized along margins and fractures, deformation textures		*Olivine* (15%) - subhedral to euhedral, partially to completely serpentinized		*Calcite* (15%)- laths in a sheaf texture
Phase	Internal dyke		*Phlogopite* (8%) - anhedral		*Phlogopite* (10%) - subhedral and lath-shaped; completely or partially resorbed		*Opaque oxides* (10%) - euhedral to subhedral
Mineralogical classification	Calcite kimberlite		*Garnet* (<2%) - anhedral, kelyphitized				*Perovskite* (8%) - euhedral to subhedral
Textural classification	Uniform, sparsely macrocrystic						*Monticellite* (7%) – granular, carbonatized
							serpentine (5%) - Interstitial
							Phlogopite (3%) – laths
							Apatite (2%) - acicular
Sample	DDH-012-4		*Olivine* (28%)-anhedral, serpentinized along margins and fractures, deformation textures		*Olivine* (12%) - subhedral to euhedral, partially to completely serpentinized		Calcite (15%)- laths in a sheaf texture
Phase	External dyke				*Phlogopite* (5%) - subhedral and lath-		*Opaque oxides* (10%) - euhedral to subhedral

					shaped; completely or partially resorbed		
Mineralogical classification	Calcite kimberlite						*Perovskite* (10%) - euhedral to subhedral
Textural classification	Segregationary, Macrocrystic						*serpentine* (8%) - Interstitial
							Monticellite (5%) – granular, carbonatized
							Phlogopite (5%) – laths
							Apatite (2%) - acicular
Sample	DDH-014-2		*Olivine* (30%)-anhedral, serpentinized along margins and fractures, deformation textures		*Olivine* (15%) - subhedral to euhedral, partially to completely serpentinized		Calcite (20%)- laths in a sheaf texture
Phase	Internal dyke				*Phlogopite* (5%) - subhedral and lath-shaped; serpentinized		*Opaque oxides* (10%) - euhedral to subhedral
Mineralogical classification	Calcite kimberlite						*Perovskite* (10%) - euhedral to subhedral
Textural classification	Uniform, Macrocrystic						*serpentine* (3%) - Interstitial
							Monticellite (3%) – granular, carbonatized
							Phlogopite (2%) – laths
							Apatite (2%) - acicular
Sample	DDH-015-6		Olivine (26%)-anhedral, serpentinized along margins and fractures, deformation textures		Olivine (20%) - subhedral to euhedral, partially to completely serpentinized		*Calcite* (15%)- Interstitial, tabular, segregationary
Phase	External dyke		Phlogopite (3%) - anhedral		Phlogopite (5%) - subhedral and lath-shaped; serpentinized		*Opaque oxides* (10%) - euhedral to subhedral
Mineralogical classification	Calcite kimberlite		Garnet (1%) - anhedral, kelyphitized				*Perovskite* (10%) - euhedral to subhedral
Textural classification	Slightly segregationary, Macrocrystic						*Serpentine* (8%) - Interstitial
							Monticellite (5%) – granular-g, carbonatized
							Phlogopite (5%) – subhedral
							Apatite (2%) - acicular


DDH-011-7
D11

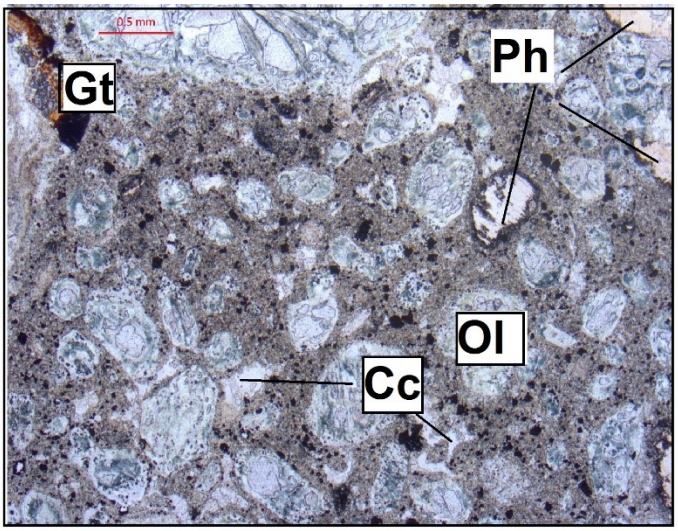
0.5 mm
Gt
Ph
Ol
Cc


DDH-002-4
D11

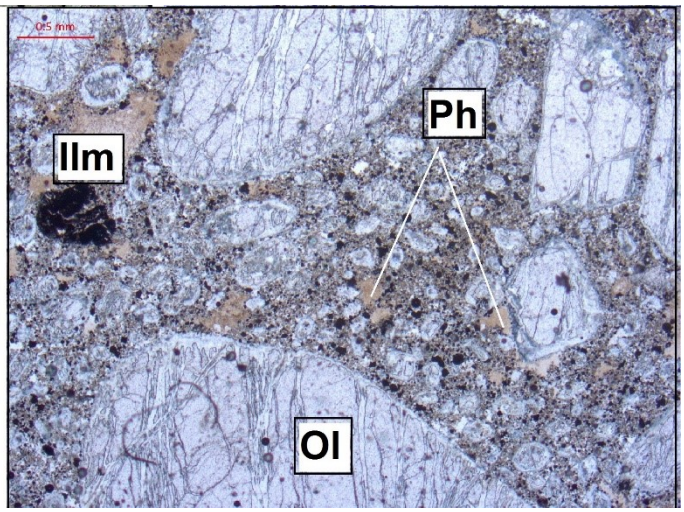
0.5 mm
Ilm
Ph
Ol

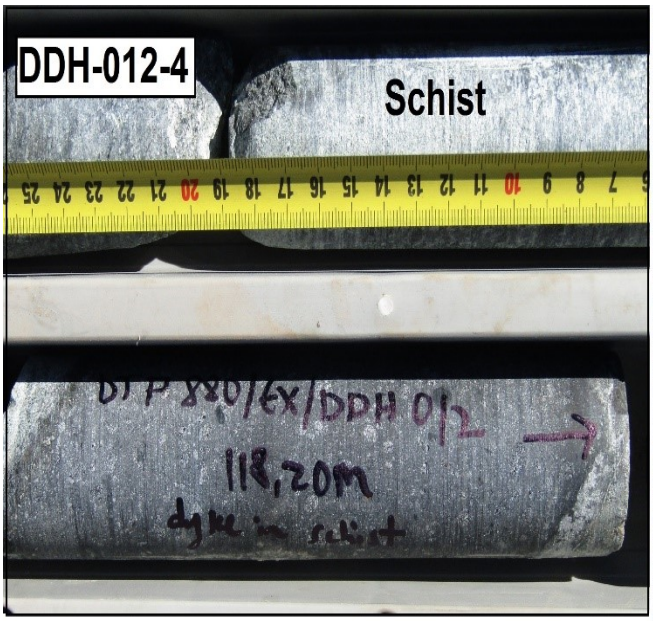
DDH-012-4
Schist

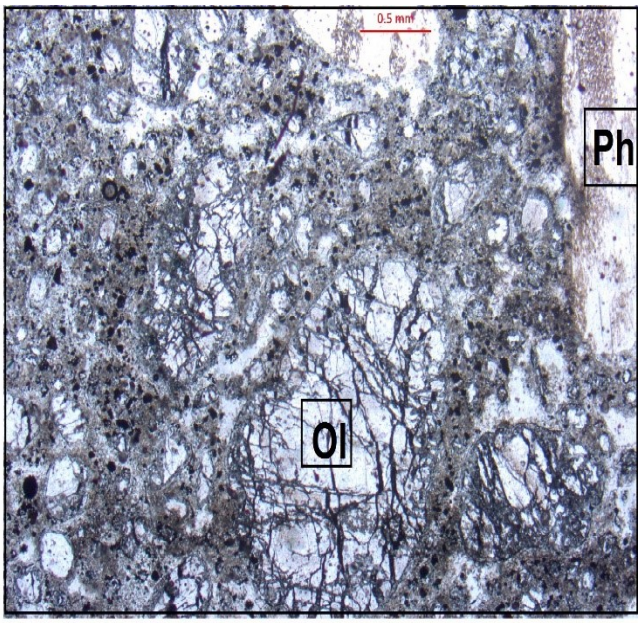
0.5 mm
Ph
Ol


DDH-013-2
98,00m
D17

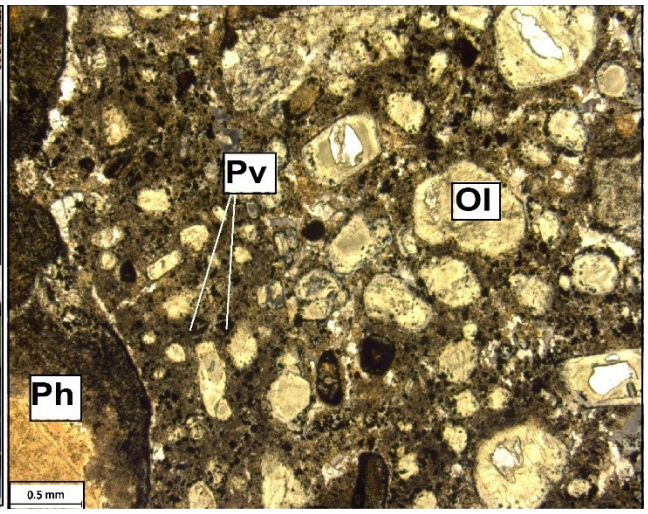
Pv
Ol
Ph
0.5 mm


DDH-015-6
Schist

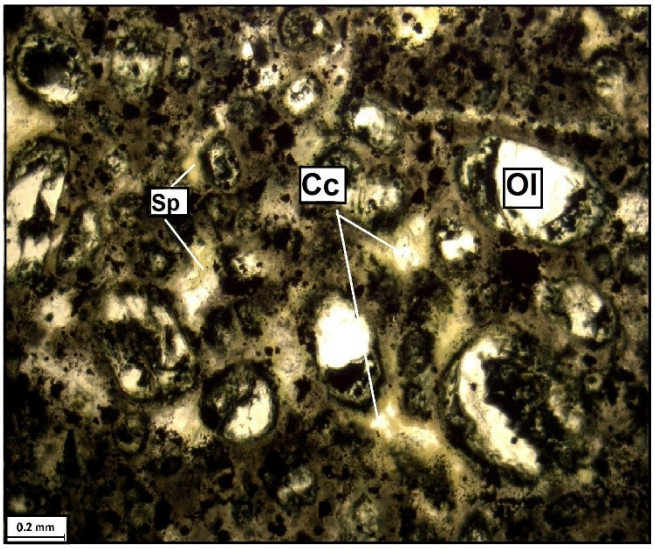
Sp
Cc
Ol
0.2 mm

B.5. Aphanitic calcite kimberlite

	Kimberlite		Macrocrysts (modal%)		Phenocrysts (modal%)		Groundmass (modal%)
Sample	DDH-001-2		*Olivine* (1%) - anhedral, partially serpentinized		*Olivine* (30%) - subhedral to euhedral, partially serpentinized		*Calcite* (30%)- interstitial and tabular
Phase	Internal dyke				*Phlogopite* (8%) - subhedral and poikilitic		*Serpentine* (12%) - Interstitial
Mineralogical classification	Opaque-rich calcite kimberlite						*Opaque oxides* (10%) - euhedral to subhedral
Textural classification	Uniform, Aphanitic						*Perovskite* (5%) - euhedral to subhedral
							Phlogopite (3%) – Interlocking laths
							Apatite (2%)- acicular
Sample	DDH-008-4				*Olivine* (22%) - subhedral to euhedral		*Calcite* (30%)- interstitial and tabular
Phase	Internal dyke				*Phlogopite* (3%) – resorbed laths		*Perovskite* (20%) - euhedral to subhedral (0.125 – 0.25 mm)
Mineralogical classification	Perovskite -rich calcite kimberlite						*Opaque oxides* (13%) - euhedral to subhedral
Textural classification	Uniform, Aphanitic						*Serpentine* (7%) - Interstitial
							Apatite (5%)- acicular
Sample	DDH-008-8				*Olivine* (30%) - subhedral to euhedral, partially serpentinized		*Calcite* (25%)- interstitial and tabular, poorly developed segregations
Phase	External dyke				*Phlogopite* (3%) – resorbed laths		*Serpentine* (20%) – Interstitial, poorly developed segregations
Mineralogical classification	Serpentine calcite kimberlite						*Opaque oxides* (10%) - euhedral to subhedral
Textural classification	Segregationary, Aphanitic						*Perovskite* (5%) - Euhedral to subhedral
							Phlogopite (5%) – Interlocking laths
							Apatite (2%)- acicular
Sample	DDH-012-3				*Olivine* (30%) - subhedral to euhedral, partially serpentinized		*Calcite* (25%)- interstitial and tabular
Phase	Internal dyke				*Phlogopite* (10%) - resorbed laths		*Serpentine* (12%) - Interstitial
Mineralogical classification	Opaque-rich calcite kimberlite						*Opaque oxides* (10%) - euhedral to subhedral

Textural classification	Uniform, Aphanitic						*Perovskite* (8%) - euhedral to subhedral
							Phlogopite (3%) – Interlocking laths
							Apatite (2%)- acicular

Sample	DDH-013-3		*Olivine* (1%) - anhedral, partially serpentinized		*Olivine* (25%) - subhedral to euhedral, partially serpentinized		*Calcite* (25%)- interstitial and tabular
Phase	Internal dyke		*Phlogopite* (2%) - anhedral, partially serpentinized		*Phlogopite* (15%) - subhedral and poikilitic, partially resorbed		*Phlogopite* (13%) - Interlocking laths
Mineralogical classification	Phlogopite – rich calcite kimberlite						*Opaque oxides* (8%) - euhedral to subhedral
Textural classification	Uniform, Aphanitic						*Perovskite* (7%) - euhedral to subhedral
							Serpentine (5%) - Interstitial
							Apatite (2%)- acicular

Sample	DDH-014-6				*Olivine* (30%) - subhedral to euhedral, partially serpentinized		*Calcite* (25%)- Interstitial, segregationary and tabular
Phase	External dyke				*Phlogopite* (3%) – Resorbed laths		*Serpentine* (15%) – Interstitial, segregationary
Mineralogical classification	Serpentine calcite kimberlite						*Opaque oxides* (13%) - euhedral to subhedral
Textural classification	Segregationary, Aphanitic						*Perovskite* (7%) - euhedral to subhedral
							Phlogopite (5%) – Interlocking laths
							Apatite (2%)- Acicular


DDH-008-4
D11

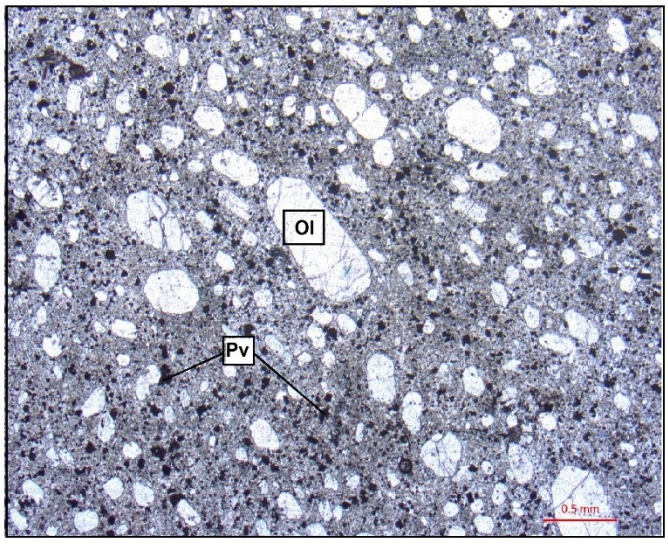
Ol
Pv
0.5 mm


DDH-008-8
Schist

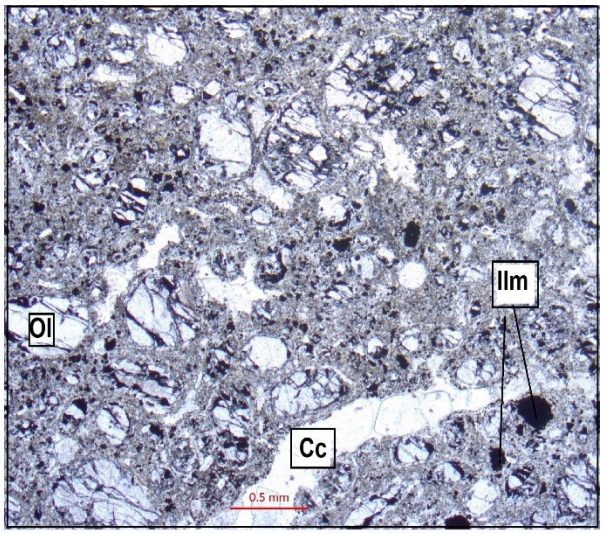
Ilm
Ol
Cc
0.5 mm


DDH-012-3
D11

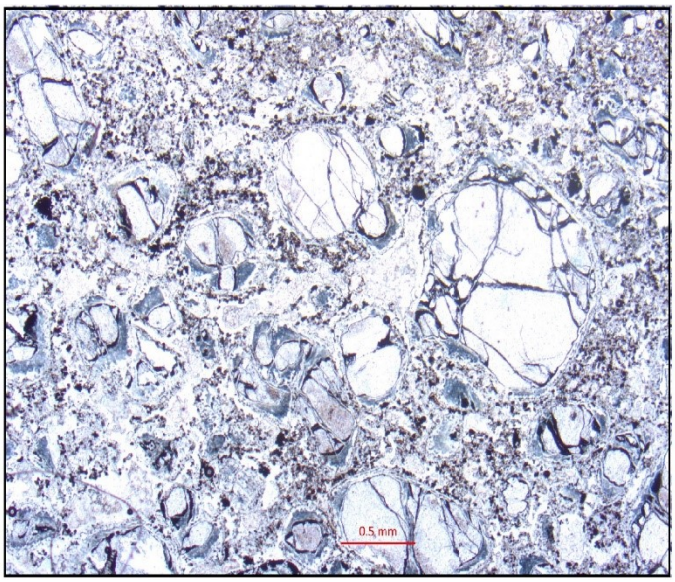
0.5 mm

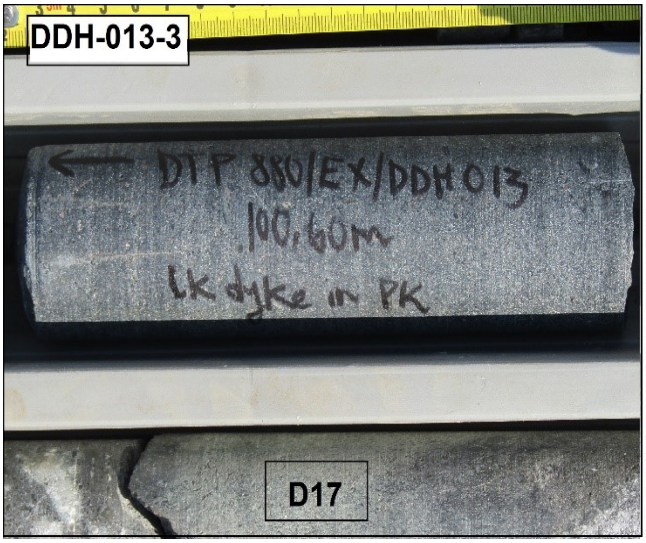
DDH-013-3
DTP 880/EX/DDH 013
100.60m
Lk dyke in PK
D17

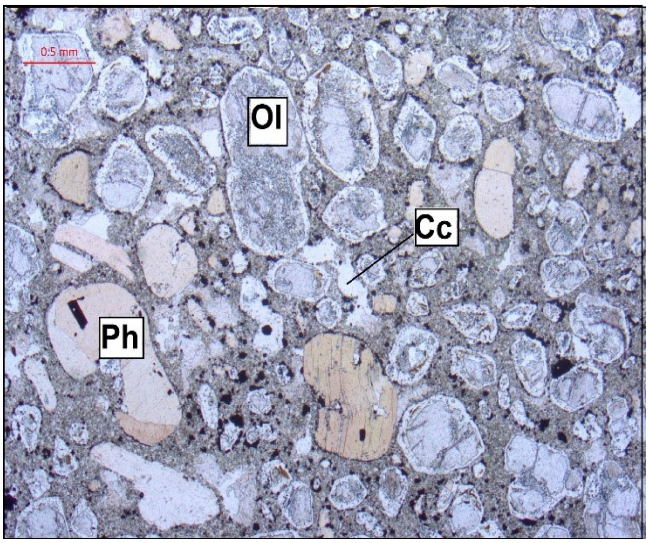
0.5 mm
Ol
Cc
Ph


DDH-014-6
145.0m
DTP 880/EX1/DDH014
Dyke in Schist wallrock
Schist

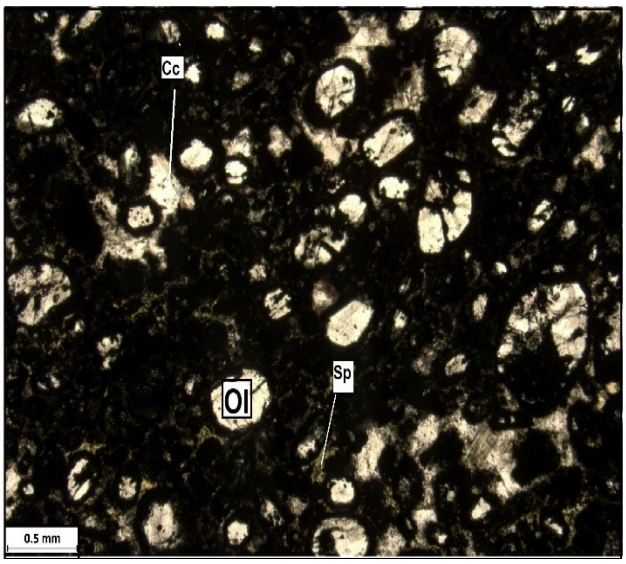
Cc
Sp
Ol
0.5 mm

APPENDIX C : SAMPLE PREPARATION AND ANALYSIS

C.1. Electron micro analyse probe (EPMA)

Mineral analysis were carried out on 30μm polished sections. To minimize electric charge build up polished sections were carbon coated. The carbon coated polished sections were analysed in the department of Geological sciences at the University of Cape Town (UCT) using a JOEL JXA – 8100 electron probe microanalyzer (EPMA). The EPMA was operated at an accelerating voltage of 15 Kv for all minerals with a 20nA beam current. Analysis of all elements in both phlogopite and olivine had a counting time of 10 seconds, except for Ni in olivine which was set to a peak counting time of 30 seconds.

C.2 X-ray fluorescence (XRF)

All bulk-rock sample preparation and analysis of selected samples was conducted in the department of Geological sciences at UCT. The freshest samples available were selected and passed through a jaw crusher. Crushed rock fragments were then individually selected using binocular microscope (×50 magnification) to remove all visible xenogenic fragments (crustal, mantle xenoliths, and megacrysts, calcite veins) and any weathered fragments. Approximately 30-40g of clean sample was collected and then powdered for 1-2 minutes using a carbon steel Sieb swing mill. Approximately 2g of sample was weighed using porcelain crucibles and carefully recorded. The crucibles were left to dry overnight in an oven at 110°C and re-weighed on the following day. H_2O content in the various samples were determined using the mass difference from both recordings. The samples were then left overnight to roast at 850°C and re-weighed to determine the percentage of loss on ignition (LOI).

Analysis were run on a Philips X'Unique wavelength dispersive spectrometer in the department of Geological sciences at UCT using a low dilution fusion technique. Major elements were analysed using a Mo/Sc x-ray tube, first transitional metals (Co, Cr, Ni, and V) using a Au tube and HFSE (Nb and Zr) using a Rh tube. The analysed XRF concentrations and recommended values for international rock standards (BHVO-1, SARM 48; Govindaraju, 1994) show no significant difference (Tables B.2).

C.2.1 Fusion disks preparation

Fusion discs were prepared for trace elements analysis. In order to prepare fusion discs, 0.7g of roasted sample was weighed out with 6g of lithium tetraborate-lithium metaborate sigma X-ray flux. The fusion discs were then prepared in claisse fluxy ™ Pt-Au crucibles and stored in a desiccator prior to analysis.

C.2.2 Briquettes preparation

Powder briquettes were prepared for major element analysis. In order to prepare powder briquettes, 6g of sample were injected with the binding agent poly vinyl alcohol. The briquettes were made under a 10-ton press, with boric acid rings. Powder briquettes were then placed in a vacuum chamber for 20 – 25 minutes to allow them to stabilize before being stored in a desiccator prior to XRF analysis.

C.3 Inductively coupled plasma - mass spectrometry (ICP-MS)

An ELAN 6000 Inductively Coupled Plasma Mass Spectrometer (ICP-MS) housed in the department of Geological sciences at UCT was used to determine trace element concentrations in all samples using the following approach. Approximately ~50mg of each sample were weighed into glass Teflon beakers. The samples were dissolved in a 4ml solution of hydrofluoric acid (HF) and nitric acid (HNO_3) at a proportion of 4 (HF): 1 (HNO3). The Teflon beakers containing the samples in HF-- HNO_3 solution were sealed and placed on a hotplate for ~3 days to allow for the complete digestion. After cooling, 2ml of concentrated HNO_3 was added and then dried for four hours. The previous step was repeated once. This was followed by the addition of a 4ml stock solution containing 10 ppb Re, Rh, ln and Bi as internal standards and 5% HNO_3 was added to the dried samples. The samples were then placed in an ultrasonic bath for ~1 hour. A drop of HF was added to ensure that Ta remained in solution during the analysis. Solutions containing the various samples were then diluted by another 10 times to ensure the detection of high absolute concentrations in some incompatible elements. Total procedural blanks (TPB) were run during each analysis. Average TPB trace element concentrations are given in Table C.1. The international standards BHVO-2 and SARM 39 were also run during each

(Table C.2.). The analytical precision gave a precision which is generally better than 1.3% relative standard deviation for all analysed trace elements.

Table C.1: Trace element concentrations (in ppm) of total procedural blanks (TPB) run for analysed samples representative of the different kimberlite intrusions.

	TPB		Average
Li	0.012	0.01	0.011
Sc	0.002	0.006	0.004
V	0.026	0.012	0.019
Cr	0.204	0.105	0.1545
Co	0.002	0.003	0.0025
Ni	0.433	0.141	0.287
Cu	0.001	0.006	0.0035
Zn	0.277	0.406	0.3415
Ga	0.003	0.003	0.003
Rb	0.002	0.002	0.002
Sr	0.003	0.015	0.009
Y	0.002	0.002	0.002
Zr	0.033	0.017	0.025
Nb	0.022	0.014	0.018
Ba	0.001	0.016	0.0085
La	0.001	0.003	0.002
Ce	0.001	0.004	0.0025
Pr	0.001	0.002	0.0015
Nd	0.001	0.002	0.0015
Sm	0.001	0.001	0.001
Eu	0.001	0.001	0.001
Tb	0.001	0.001	0.001

Gd	0.001	0.001	0.001
Dy	0.001	0.001	0.001
Ho	0.001	0.001	0.001
Er	0.001	0.001	0.001
Tm	0.001	0.001	0.001
Yb	0.001	0.001	0.001
Lu	0.001	0.001	0.001
Hf	0.002	0.002	0.002
Ta	0.006	0.003	0.0045
Pb	0.001	0.008	0.0045
Th	0.002	0.002	0.002
U	0.003	0.002	0.0025

Table C.2. : Average trace element concentrations (in ppm) of the international standards BHV0-2 and SARM 39 analysed at UCT compared with recommended values of Roy et al. (2007) for SARM 39 international standard and recommended values of Raczek et al. (2001) and Jochum et al. (2016) for the BHVO-2 international standard. Jochum et al. (2016) in parenthesis. Relative standard deviation (RSD).

	UCT				Recommended values	
	BHVO-2	RSD %	SARM 39	RSD %	BHVO-2	SARM 39
Sc	31.11	1.272	13.46	0.668	(31.83)	13.7
V	306.5	0.334	115.5	0.586	(318.2)	115.5
Cr	272.0	0.606	1272	0.360	(287.2)	1274.2
Co	38.75	1.036	63.63	0.809	(44.89)	69.0
Ni	116.4	1.177	937.5	0.867	(119.8)	936.8
Zn	119.3	0.334	71.39	0.547	103.9	69.5
Ga	23.85	1.214	56.12	1.316	21.37	19.1
Rb	9.265	0.185	50.03	0.338	9.08	50.8
Sr	396.3	1.115	1485	0.189	396	1451.4
Y	23.44	0.825	15.58	0.489	(25.91)	16.4

Zr	156.8	0.439	228.8	0.233	(171.2)	243.2
Nb	17.07	1.560	99.47	0.246	(18.10)	109.2
Ba	129.0	0.587	1499	0.395	131	1683.3
La	14.50	1.066	91.99	0.691	15.2	89.2
Ce	36.78	0.910	193.9	0.922	37.5	182.9
Pr	5.261	1.089	22.03	0.671	5.29	21.5
Nd	24.53	0.618	83.45	0.686	24.5	82.2
Sm	6.149	0.662	11.39	0.718	6.07	12.2
Eu	1.934	0.753	3.012	0.562	2.07	3.14
Tb	0.877	1.240	0.884	0.153	0.936	0.99
Gd	5.923	1.786	7.834	0.643	6.24	8.58
Dy	5.098	0.537	3.909	0.752	5.31	4.23
Ho	0.934	0.848	0.583	0.527	0.972	0.62
Er	2.432	0.952	1.294	0.400	2.54	1.52
Tm	0.311	1.290	0.153	0.564	0.341	0.18
Yb	1.915	1.127	0.911	0.345	2.00	0.98
Lu	0.276	0.654	0.127	1.098	0.274	0.13
Hf	4.196	0.921	5.065	0.817	(4.470)	5.02
Ta	1.096	0.307	6.801	0.402	(1.154)	7.3
Pb	1.476	0.697	19.02	0.212	(1.653)	9.98
Th	1.220	0.313	8.740	0.742	(1.224)	9.75
U	0.401	0.783	2.141	0.362	(0.412)	2.52

The following compatible elements (Cr, Sc, and Co) all reported higher values when analysed using the XRF analytical technique compared to using the ICP-MS analytical technique. Figure C.1 shows that the analytical technique XRF gave lower values compared to those determined using ICP-MS (Fig. C.1b-d). Although Ni concentration measured using both techniques does not show similar variation, but rather shows good correlation (R^2 = 0.91) (Fig. C.1a). The observed variations are attributed to either poor dissolution of refractory minerals like chromite, ilmenite were perhaps longer residence times in HF - HNO_3 solution were required to complete acid digestion. For this reason for elements Sc, Co, and Cr, only data determined from

XRF analysis was used; whereas for Ni, only data from ICP-MS was used in the relevant chapters. A similar problem was not encountered for the incompatible elements which all generally show good correlation (Fig. C.2)

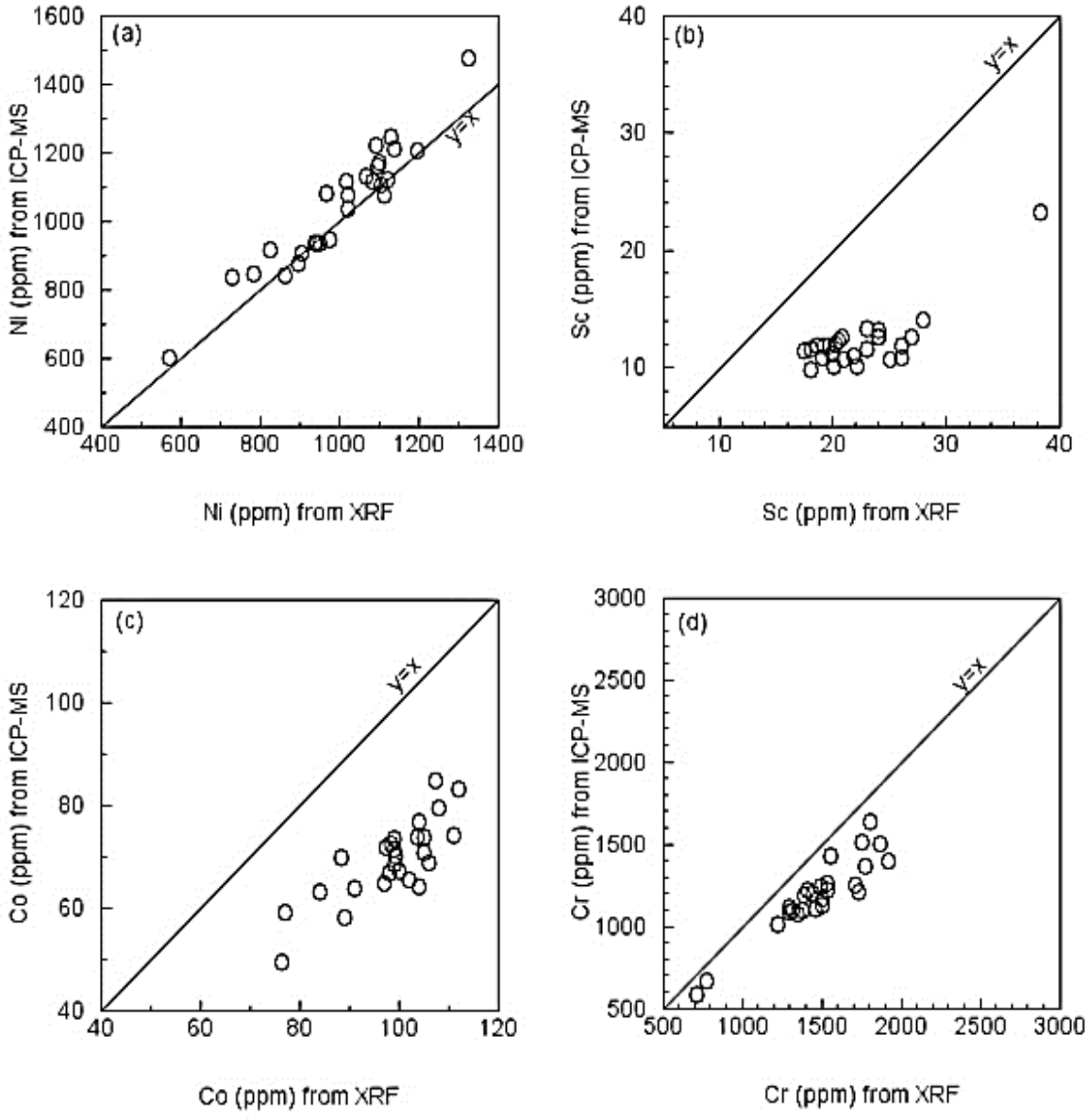

Figure C.1: A comparison of compatible elements measured using XRF and ICP-MS in samples from this study.

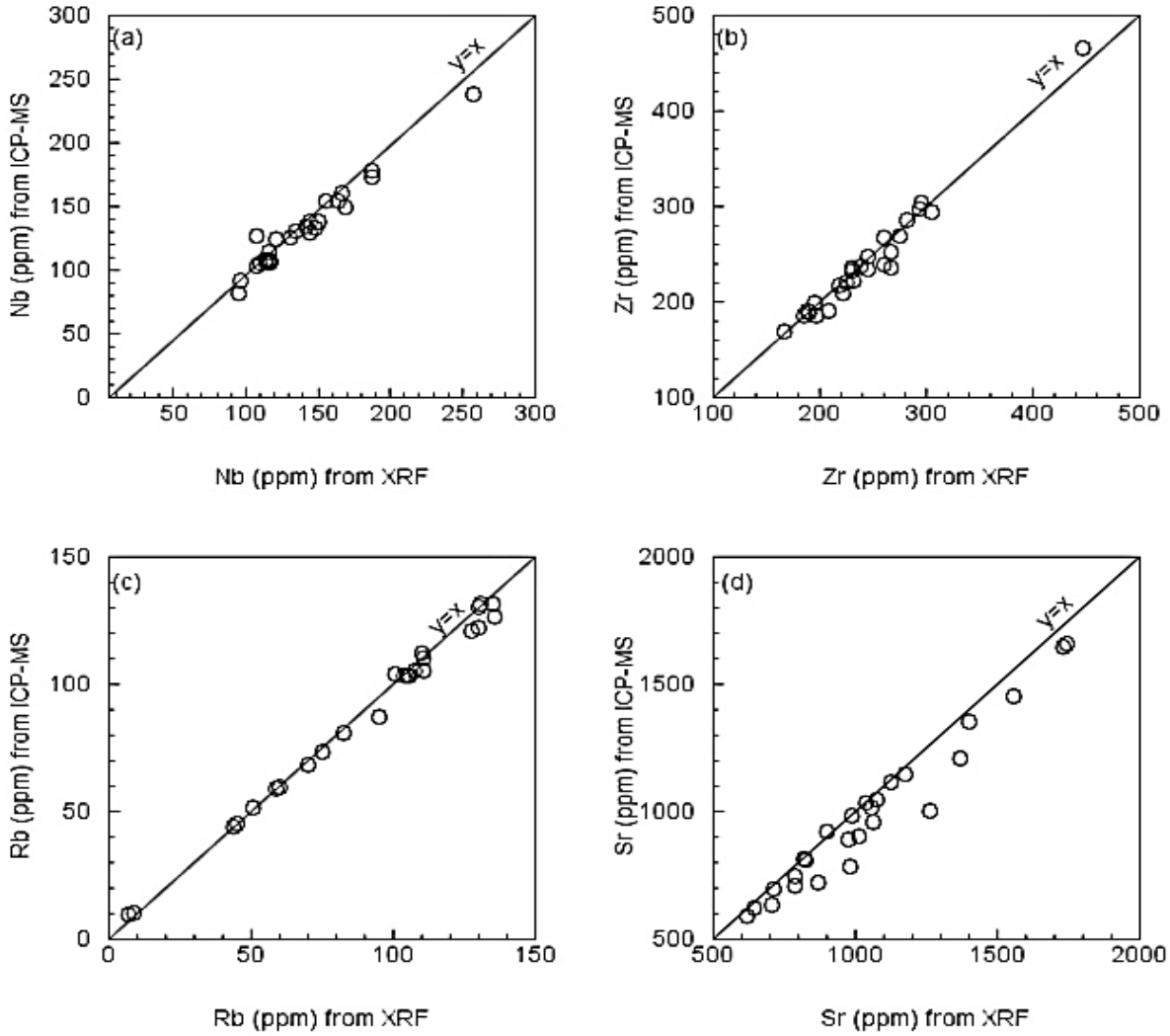

Figure C.2. : A comparison of incompatible elements analysed using XRF and ICP-MS in samples from this study.

C.4 Karbonat Bombe

CO_2 measurements were conducted using the karbonat-bombe method of Birch (1981). About 2- 4g of powdered kimberlite samples was inserted into a plexiglass cylinder and immersed in a 5ml HCl solution. The lid was screwed on tightly and shook to ensure that all sample reacted with the acid. A pressure reading was taken on the manometer after stabilisation of the pressure gauge which took between 2- 3 minutes. The CO_2 concentration was then calculated by stoichiometry from the proportion of $CaCO_3$ in the kimberlite after calibrating against a pure 1g $CaCO_3$ sample. The determined CO_2 was used to calculate H_2O concentrations in analysed samples using the determined loss on ignition (%).The Kabonat bombe apparatus was thoroughly washed after each analysis and re-calibrated with pure $CaCO_3$ after analysis of every five samples to ensure that the readings remained consistent. The estimated precision of this technique 2%. Although during the analysis difficulties were encountered with gas leakage and therefore this potentially may have reduced the precision of the technique.